

ISSN Print: 2518-4245

ISSN Online: 2518-4253

Vol. 59(4), December 2022

PROCEEDINGS

OF THE PAKISTAN ACADEMY OF SCIENCES:

A. Physical and Computational Sciences



PAKISTAN ACADEMY OF SCIENCES
ISLAMABAD, PAKISTAN

Proceedings of the Pakistan Academy of Sciences: Part A

Physical and Computational Sciences

President: Khalid Mahmood Khan
Secretary General: Tasawar Hayat
Treasurer: Amin Badshah

Proceedings of the Pakistan Academy of Sciences A. Physical and Computational Sciences is the official flagship, the peer-reviewed quarterly journal of the Pakistan Academy of Sciences. This open-access journal publishes original research articles and reviews on current advances in the field of Computer Science (all), Materials Science (all), Physics and Astronomy (all), Engineering Sciences (all), Chemistry, Statistics, Mathematics, Geography, Geology in English. Authors are not required to be Fellows or Members of the Pakistan Academy of Sciences or citizens of Pakistan. The journal is covered by Print and Online ISSN, indexed in Scopus, and distributed to scientific organizations, institutes and universities throughout the country, by subscription and on an exchange basis.

Editor:

Riffat Mahmood Qureshi, Pakistan Academy of Sciences, Islamabad, Pakistan; editor@paspk.org

Managing Editor:

Ali Ahsan, Pakistan Academy of Sciences, Islamabad, Pakistan; editor@paspk.org

Discipline Editors:

Chemical Sciences: Guo-Xin Jin, Inorganic Chemistry Institute, Fudan University, Shanghai, China

Chemical Sciences: Haq Nawaz Bhatti, Department of Chemistry University of Agriculture, Faisalabad, Pakistan

Geology: Peng Cui, Key Laboratory for Mountain Hazards and Earth Surface Process, CAS, Institute of Mountain Hazards & Environment, CAS Chengdu, Sichuan, People's Republic of China

Computer Sciences: Sharifullah Khan, Faculty of Electrical, Computer, IT & Design(FECID), Pak-Austria Fachhochschule: Institute of Applied Sciences and Technology (PAF-IAST), Mange, Haripur, Pakistan

Engineering Sciences: Akhlesh Lakhtakia, Evan Pugh University Professor and The Charles G. Binder (Endowed), Engineering Science and Mechanics, Pennsylvania State University, University Park, USA

Mathematical Sciences: Ismat Beg, Department of Mathematics and Statistical Sciences, Lahore School of Economics, Lahore, Pakistan

Mathematical Sciences: Jinde Cao, Department of Mathematics, Southeast University Nanjing, P. R. China

Physical Sciences: Asghari Maqsood, Department of Physics, E-9, PAF Complex Air University, Islamabad

Physical Sciences: Niemela J. Joseph, The Abdus Salam International Center for Theoretical Physics (ICTP-UNESCO), Trieste- Italy

Editorial Advisory Board:

Saeid Abbasbandy, Department of Mathematics, Imam Khomeini International University Ghazvin, 34149-16818, Iran

Muazzam Ali Khan Khattak, Department of Computer Science, Quaid-i-Azam University, Islamabad, Pakistan

Muhammad Sharif, Department of Mathematics, University of the Punjab, Lahore, Pakistan

Faiz Ullah Shah, Department of Civil, Environmental and Natural Resources Engineering, Lulea University of Technology, Luleå, Sweden

Kashif Nisar, Faculty of Computing and Informatics University Malaysia Sabah Jalan UMS, Kota Kinabalu Sabah, Malaysia

Guoqian Chen, Laboratory of Systems Ecology and Sustainability Science, College of Engineering, Peking University, Beijing, China

Bhagwan Das, Department of Electronic Engineering, Quaid-e-Awam University of Engineering, Science and Technology Nawabshah, Sindh, Pakistan

Muhammad Sadiq Ali Khan, Department of Computer Science, University of Karachi, Pakistan

Annual Subscription: **Pakistan:** Institutions, Rupees 4000/-; Individuals, Rupees 2000/- (Delivery Charges: Rupees 150/-)

Other Countries: US\$ 200.00 (includes air-lifted overseas delivery)

© *Pakistan Academy of Sciences*. Reproduction of paper abstracts is permitted provided the source is acknowledged. Permission to reproduce any other material may be obtained in writing from the Editor.

The data and opinions published in the *Proceedings* are of the author(s) only. The *Pakistan Academy of Sciences* and the *Editors* accept no responsibility whatsoever in this regard.

HEC Recognized, Category Y; Scopus Indexed

Published by **Pakistan Academy of Sciences**, 3 Constitution Avenue, G-5/2, Islamabad, Pakistan

Email: editor@paspk.org; **Tel:** 92-51-920 7140 & 921 5478; **Websites:** www.paspk.org/proceedings/; www.ppaspk.org

Printed at **Graphics Point.**, Office 3-A, Wasal Plaza, Fazal-e-Haq Road Blue Area Islamabad.

Ph: 051-2806257, **E-mail:** graphicspoint16@gmail.com



PROCEEDINGS OF THE PAKISTAN ACADEMY OF SCIENCES: PART A Physical and Computational Sciences

CONTENTS

Volume 59, No. 4, December 2022

Page

Research Articles

- Gun Detection in CCTV Images using HAAR-Like Features 1
—*Sami Ur Rahman, Fakhre Alam, and Wajid Ali*
- Design and Implementation of Low-Cost Data Acquisition System for Small and Medium Enterprises (SMEs) of Pakistan 13
—*Muhammad Imran Majid, Ejaz Malik, Tahniyat Aslam, Osama Mahfooz, and Fatima Maqbool*
- Modeling and Intelligent Controller Design for Reactor Regulating System of Advanced CANDU Reactor (ACR-700) in LabVIEW 25
—*Arshad Habib Malik, Feroza Arshad, and Aftab Ahmad Memon*
- Analysis of Stochastic Patterns of Daily Minimum Extreme Temperature of Karachi in Global Climate Change Perspective 37
—*Muhammad Atif Idrees, Syed Ahmed Hassan, and Muhammad Arif Hussain*
- Tidal Range Energy Resource Estimation of Khor Kalamat using Geostatistical Modeling 45
—*Ambreen Insaf, Mirza Salman Baig, Saba Javaid, Umair Abbas, and Zaheer Uddin*
- Evaluation of Air Permeability of Knitted Fabrics at Various Washing Intervals 55
—*Mehreen Ijaz, Namood-e-Sahar, and Zohra Tariq*
- Mathematical Analysis of Conducting and Dielectric Sphere in Fractional Space 61
—*M. Imran Shahzad, M. Akbar, Saeed Ahmed, Sania Shaheen, and M. Ahmad Raza*
- Investigation of Groundwater Quality for Drinking Usage in Kifri District (Iraq) by using NPI and WQI Indices 67
—*Abdulmutalib Raafat Sarhat, Muhammad Mohsin, and Aram Hassan Mohammed*

Instructions for Authors

Submission of Manuscripts: Manuscripts may be submitted as an e-mail attachment at editor@paspk.org or submit online at <http://ppaspk.org/index.php/PPASA/about/submissions>. Authors must consult the *Instructions for Authors* at the end of this issue or at the Website: www.paspk.org/proceedings/ or www.ppaspk.org.



Gun Detection in CCTV Images using HAAR-Like Features

Sami Ur Rahman, Fakhre Alam*, and Wajid Ali

Department of Computer Science, University of Malakand, Pakistan

Abstract: Automated video-based surveillance is an important area of research to assist the security personnel to detect the incident of any abnormal events in the surroundings. The objective of this paper is to develop a framework for automatic gun detection using closed-circuit television (CCTV) images. The methodology presented in this paper involves the development of a framework for automatic gun detection using closed-circuit television (CCTV) images, with the aim of enhancing the surveillance of crime and improving human security. The proposed approach consists of a dataset of CCTV images containing instances of guns, as well as non-gun images for comparison. These images would be used to train the proposed algorithm to recognize and identify guns in future CCTV images. The proposed framework is designed for an indoor environment and uses Haar-like features for gun detection. The proposed system involves the installation of CCTV cameras in a suitable corner of an indoor environment for surveillance. The CCTV cameras capture the scene and the frames of the scene are compared with a predefined dataset for automatic gun detection. The proposed approach draws a bounding box and raises an alarm if it detects a gun in a frame extracted from a captured scene. This provides a visual indication of the presence of a gun, making it easier for relevant authorities to quickly identify and respond to the threat. The proposed system shows promising results in real-time applications and about 90% accuracy has been achieved.

Keywords: Gun Detection, CCTV, Security, Video-based Surveillance, Haar-like Features, Support Vector Machine.

1. INTRODUCTION

Over the last two decades, the situation of the whole world becomes very difficult in terms of security due to terrorist attacks on public and private organizations such as universities, colleges and schools. Several methods have been taken to reduce security threats such as security alarm implementations, detection of grievous objects, and deployment of security guards and metal detectors. But these methods cannot work well because of the complex nature of anti-security threats and can be counteracted or deceived very easily. Now technology is used to deal with robbery and terrorist attacks with advanced computer vision systems. Closed-circuit television (CCTV) based security systems consist of cameras installed at different locations. With the help of these cameras, the locations of physical objects are detected and monitored. CCTV-based system record the scenes based on various visual information which greatly help in the investigation.

Although CCTV-based security systems play an important role in crime control and investigation, however, the system needs continuous monitoring from the human operator which sometimes becomes very difficult. Due to the advancement in technology, security threats are now automatically detected and alarms are generated accordingly. CCTV footages are automatically monitored for this purpose by applying various computer algorithms. These algorithms detect various types of human security threats [1]. The commonly detected threats are the detection of weapons, gunshots and suspected humans like thieves and terrorists [2]. These methods automatically generate an alarm when the above parameters are detected.

Automatic gun detection is indeed an important area of research and development that has the potential to contribute significantly to crime prevention efforts [3]. Automatic gun detection refers to the use of technology, such as computer vision algorithms and machine learning techniques,

to identify the presence of firearms in images or video footage [4]. This technology can be used in various settings, such as airports, schools, and public spaces, to detect the presence of firearms and alert security personnel or law enforcement officers.

The use of automatic gun detection technology can help prevent violent crimes and save lives [5]. For example, if a firearm is detected in a school or public place, security personnel can respond quickly to remove the threat and prevent a potential mass shooting. Similarly, if a firearm is detected at an airport or border crossing, law enforcement officers can take appropriate action to prevent smuggling or other illegal activities.

Gun detection in CCTV images using Haar-like features is a computer vision technology that can automatically detect the presence of guns in indoor environments from CCTV camera footage [6]. Haar-like features are image features that describe the local intensity patterns of an image and are commonly used in object detection applications [7].

In the literature, several approaches are available for gun detection. For example, Kumar *et al.* [4] have proposed a method for gun detection using Harris Interest Point Detector (HIPD). In this method, color-based segmentation is used to remove unrelated objects from the image by applying a k-mean clustering algorithm in their system. In the segmented image, HIPD and Fast Retina Key point (FREAK) help in locating the gun in the scene. Signal detection frameworks with psychophysical experiments are used for weapons detection by Darker *et al.* [8]. The goal of their work is to increase the effectiveness of the system by detecting firearms that are carried into public places. In the work of Xue *et al.* [9] various image fusion methods are used for concealed weapons detection. Another method proposed by Darker *et al.* [10] for weapons detection. Their method is the combination of two approaches: The first approach is the use of psychological techniques, and the visual cues used by CCTV operators for the detection of potential gun crime in real-time CCTV footage are made clear. The latest Digital Image Processing (DIP) algorithms and these extracted cues are combined in the second approach for object detection, motion tracking and machine learning. Image processing and sensors-based

technologies are used for the automatic detection and recognition of concealed weapons in the method developed by Prof *et al.* [11]. The fuzzy K-NN approach is used in the work of Roomi *et al.* [12]. In this approach, an image is converted into binary form by selecting the threshold as a mean of the two peaks of the bimodal histogram. To collect the object of interest the region of every object is ordered and the mean value is calculated which is set to a threshold value. The shape feature algorithm is implemented after object boundary extraction. Some sensors technologies are listed in the work proposed by Khajone *et al.* [13] which are used for Concealed Weapons Detection applications such as imaging sensors, recent advancement in Millimeter Wave (MMW) sensor technology that led to video rate (30 frames per second) and Passive Millimeter Wave (MMW). The detailed information of every object that is being monitored cannot provide by MMW alone.

Therefore, camera sensor fusion methodologies by means of MMW and IR or MMW and EO cameras are required to enhance the practical values of passive MMW in order to get information from various sensors that led to an effective Concealed Weapons Detection System. Concealed threats can be detected in high-security areas by using active mm-wave [14]. Metal and non-metal threats like handguns, knives, explosives or any concealed anomalous object can be detected by using this technology. It is not possible to monitor a huge amount of cameras with a human operator, therefore, implementing an image-understanding system instead of the human operator and alerting them if potentially dangerous situations occur is the best solution [15]. Another work was done by Dever *et al.* [16] for armed robbery detection. To classify the point of the arms and identify the classic hold-up position of armed robbery they examine the skeleton of the medial lines of the silhouette. Their proposed method contains four steps: Silhouette extraction, Skeleton segmentation, Segment identification and arm analysis. Another work was proposed by Andrzej *et al.* [17] for the visual detection of knives in a security application. The base of their work is on the Active Appearance Model (AAM) which is a statistical framework of shape and pixel intensities (texture) through the object. The arrangement of shape and texture is term as 'appearance' and the use of an algorithm that fits the shape texture

model in a new image is term as ‘active’. Regions of interest are manually labelled in the training phase which is supposed to be the milestone for defining their shape. Richard *et al.* [18] attempt three different approaches for concealed weapon detection. In the first approach, edge detection is used with pattern matching to specify the presence of concealed weapons. Daubechie wavelet is used in the second approach and Scale Invariant Feature Transform (SIFT) is used in the third approach. Lowe *et al.* [19] developed a system in which distinctive invariant features are extracted from images. These features are used for dependable matching among various views of an object or scene. Low-level image and video processing techniques are presented in the work of Foresti *et al.* [20] which are required to implement a modern visual-based surveillance system. Another work by Veena *et al.* [21] proposed a system for gun-type classification by implementing edge detection and SUSAN (Smallest Uni value Segment Assimilating Nucleus) low-level image processing. Michal *et al.* [22] proposed and benchmark an algorithm which is able to detect an individual that carries concealed weapons and alert the CCTV operator. Dee *et al.* [23] present an overview of behavior analysis and event detection systems within computer vision for surveillance. Spirito *et al.* [24] developed a system for the automatic detection of risky actions for underground surveillance using automatic video sequence processing techniques. In another work presented by Lee *et al.* [25] they found a video clip which is mostly different in terms of similarity measures from another type of video. The similarity matrix is calculated by using difference or chamfer difference as the similarity measure of features in different clips without searching the key-frames and finally, N-cut clustering is applied for abnormal event detection in video. In the work of Hung *et al.* [26] analyzed robbery events for suspicious object detection. First, background subtraction is used to detect foreground objects, and then every moveable object is tracked and obtains its route. Then suspicious object transferring condition between two persons is analyzed by using a robbery event analysis system. Ismail *et al.* [27] proposed a method for real-time monitoring of individuals and their activities. Their system works on monocular grey-scale video imagery and is applicable in outdoor environments. They employ a combination of shape analysis and tracking to locate people and

their parts to create a model of people’s appearance so that they can be tracked through interactions such as occlusion.

There are some limitations in the existing work; some approaches used special types of sensors which are too expensive while others have complex methodologies and complex feature types. Some of the approaches are not real-time and have a lengthy process of feature calculations. In the proposed work we have used a HAAR-like feature for gun detection which is a simple, accurate and fast calculation process.

This paper presents an automatic system for gun detection in a real-time scene using computer vision techniques. The proposed gun detection system uses CCTV images to read frames, process them, and identify the presence of a gun. The system’s speed and efficiency make it a suitable solution for indoor environments where the need for quick action may be critical to preventing security threats. By detecting guns in real-time, the system can alert security personnel to the presence of a potential threat and help to decrease the response time in the event of an incident.

2. PROPOSED ALGORITHM

A schematic diagram of the proposed methodology for gun detection in a real-time indoor environment is shown in Figure 1. In the proposed algorithm, first, the algorithm calculates the HAAR-like features of the current frame. Then these features are compared with reference features of the existing data set. If the features are matched with reference features, then a gun is detected in the frame otherwise the frame is ignored and the next frame is read out.

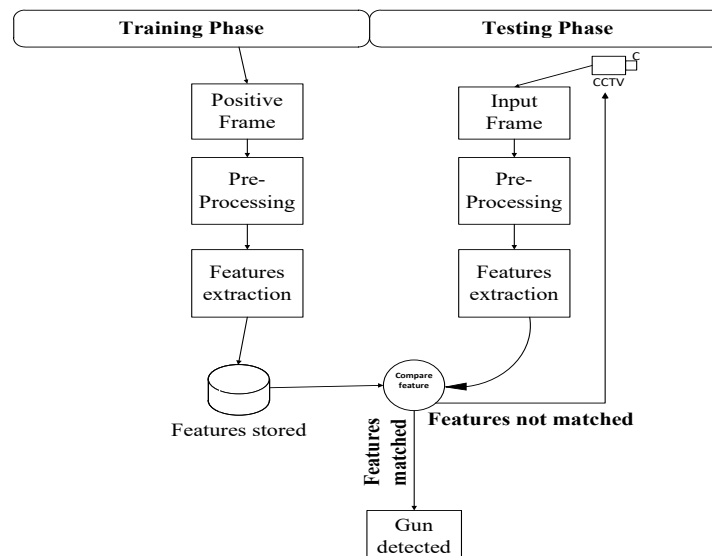
The proposed methodology for automatic gun detection in a real environment consists of two phases i.e., the training phase and the testing phase.

2.1 Training Phase

In this phase, the system is trained for gun detection and consists of the following steps: First positive frames are selected from the dataset which contains the gun. Then the frames are pre-processed and the region of interest (Gun) is selected from the frames. After selecting the region of interest, HAAR Like

Table 1. Summary of the state-of-the-art approaches

Reference	Work based on	True positive rate	True negative rate	False positive rate	Accuracy	Comments
[2]	HIP Detector	83.07%	-	8.33%	84.26%	Uses color based segmentation
[14]	3D radar imaging technique					Complex configuration of T/R pairs of antennas
[17]	AAM				92.5%	Corner detection
[12]	Use fuzzy K-NN Approach					Implementation of shape context descriptor and Zernike moments
[25]	Clustering based on N-CUT					Implementation of N-cut algorithm for clustering
[29]	HOG Features	81.14%	96%	4%	88.57%	Complex methodology of features calculation
[8]	Sensors Technology					Complex conversion process of analogue output of a CCTV camera to a digital signal and transformation of digital signal to computer via fire wire
[21]	Edge detection					Implementation of Canny Edge detector and SUSAN corner detection
Proposed work	HAAR Like Features	91%	87%	12.50%	95%	Simple method for feature calculations

**Fig.1.** Schematic diagram of the proposed methodology for gun detection in real time indoor environment

features are calculated from the region of interest and are stored in a database for comparison of input frames.

2.2 Testing Phase

In this phase detection of the gun is done from input frames in the following steps: First, the input frame is read from the CCTV camera and then the input frame is preprocessed and HAAR Like features are extracted from the input frames which are explained in the next section. Then these features are compared with the existing features. If the features match then the gun will be detected from the frame otherwise the frame will be discarded and the next frame will be read from the CCTV stream.

2.3 Haar-Like Features

The proposed system uses a HAAR-like feature for gun detection which can be obtained by the product of an image and some HAAR-like templates.

More precisely, let I denote an image and P denote a pattern respectively with the same size $N \times N$. The feature value f can be calculated for HAAR-like features which have k rectangles as.

$$f = \sum_{j=1}^k w(j) \cdot u(j) \quad (1)$$

The mean intensity of the pixel in image I surrounded by j^{th} rectangle is supposed to $u(j)$. The rectangle mean is referring to u and the weight assigned to the j^{th} rectangle is represented by $w(j)$ in the above equation.

Usually, to satisfy the following equation, the weight given to the rectangles of HAAR-like features is set to default numbers.

$$\sum_{j=1}^k w(j) = 0 \quad (2)$$

For example, in Figure 2(a) default weights 1 and -1 are assigned to the rectangles of HAAR-like features. In Figure 2(c) default weights 1, -2, and 1 are assigned to the rectangles of HAAR-like features.

HAAR-like features provide a very attractive

trade-off between speed of evaluation and accuracy which is the main cause of the popularity of HAAR-like features.

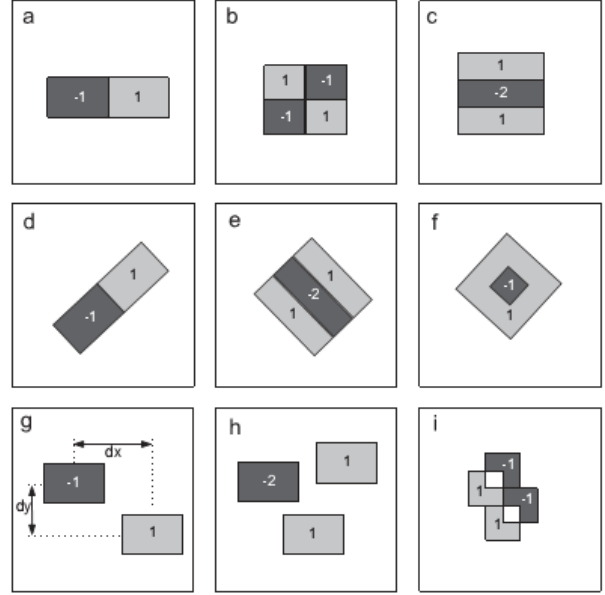


Fig. 2. HAAR-like features are presented with the default weights given to its rectangles. Fig (a) and (b) presented HAAR-like features introduced by Papageogiou et al. [28], Fig (c) presented a HAAR-like feature with three rectangles proposed by Viola and Jones [29]. Fig (d-f) presented Leinhardt's rotated feature. Fig (g) and (h) presented Li et al. [30] disjoint HAAR-like features and Fig (i) presented Voila and Jones [31] diagonal feature proposed to get diagonal arrangements of the object's visualization.

2.3.1 Integral Image

Integral image representation helps in the fast computation of HAAR-like features. It is the use of summed area table. Crow in 1984 introduced this concept which is used mostly in computer graphics.

The integral image can be defined as:

$$jj(m, n) = \sum_{m' \leq m, n' \leq n} j(m', n') \quad (3)$$

Where $jj(m, n)$ is the integral image and $j(m', n')$ is the intensity of the original image. The integral image can be calculated in only one pass using the following recurrences.

$$s(m, n) = s(m, n - 1) + j(m, n) \quad (4)$$

$$jj(m, n) = jj(m - 1, n) + s(m, n) \quad (5)$$

Where $s(m,n)$ is the collective sum of row with the following cases:

$s(m,-1)=0$ And $jj(-1,n)=0$ with the integral image, constant time is required to calculate each feature. Four memory references are required to calculate the sum of any rectangle.

The integral image calculation is shown in Figure 3.

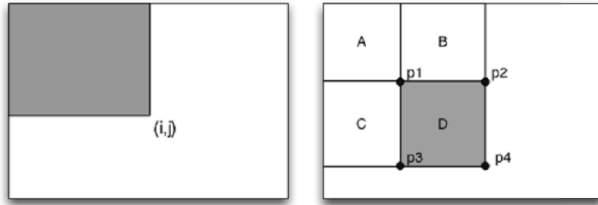


Fig. 3. Rectangle feature calculation and integral image. $k(i,j)$ = Sum of image intensities in shaded area

$$D = k(p4) + k(p1) - k(p2) - k(p3)$$

Moreover, rectangles which share corners are used by HAAR-like feature, the total amount of memory references required to calculate a feature can further be decreased.

For example, two, three and four rectangle features need only six, eight and nine memory references respectively.

2.4 Pseudo Code of the Proposed Algorithm

- Step.1 CF=read frame
 Step.2 Calculate HAAR-like feature of the current frame
 Step.3 Compare these features with pre-defined features
 If (current frame features = predefined features)
 Step.4 A Gun exists and detected
 B CF=read next frame
 C Go to step.2
 Else
 Step.5 A Ignore this frame
 B CF=read next frame
 Step.6 Go to step 2

In step. 1& step. 2 the algorithm read one frame from CCTV footage and assign this frame to the variable CF (Current Frame). The system then extracts HAAR like features from this frame. In step.3 comparison of the extracted features were

initiated with predefined features on which the system was trained. In step.4, if the current frame features are matched with predefined features, then the gun is detected in the current frame and the algorithm read the next frame in step.4 (b) from the CCTV footage and that process is repeated continuously. If this condition is not matched then the algorithms ignore/discard that frame and read the next frame for the next operation.

The initial point of the proposed system was to select the best feature type. Therefore, we select HAAR like features for our proposed system because these features are mostly used for object detection, fast evaluation speed and simple method of calculations. In the proposed system, we have used our own created data set due to unavailability of standard datasets on Internet. For the dataset, we have recorded two video clips. Then we have extracted positive and negative frames from recorded videos with some background images.

Positive frames are those frames in which the gun is present and negative frames are those frames which do not contain guns. Using this dataset, we trained the HAAR cascade classifier to detect the gun in the video. A lot of miss detections occurred using the HAAR cascade classifier due to its weak classification. Therefore, we have used Support Vector Machine (SVM) for further classification of the detected region selected by the HAAR cascade classifier. We have trained the SVM classifier by extracting the HAAR-like features from the gun and background images and then classifying the selected region of the HAAR cascade on the trained SVM classifier. This classifier performs a strong classification to ensure that the detected region is a gun.

3. RESULTS

To evaluate the performance of the proposed method, it was tested in different sessions with various conditions. For Example, different angles of the gun and occlusion (if the object of interest is hidden by another object) etc. were used. There are multiple images with various scaling and angles in the dataset and these images are used to test the trained classifier.

The classifier detects the gun, the detector draws

a bounding box around the gun if it exists in the scene. We conduct two recordings for the precise estimation of algorithm performance. The gun was not visible for the whole duration of the recording however the subject was holding a gun in hand in the first recording. The gun was occluded by certain objects or it was not in the coverage of the camera for a period of time. The subject did not hold any gun in hand but was empty-handed or take some casual items in hand in the second recording. To validate the performance of the cascade classifier we use evaluation metrics. This is discussed in the next section.

3.1 Evaluation Metrics

True positive (TP)

Gun exists in the frame and is detected.

$$1. Tp = Gd \div (Gn + Gd)$$

Gd=Frames in which gun exist and is detected

Gn=Frames in which gun exist but not detected

False positive (FP)

Gun is not existed in the frame and is detected

$$2. Fp = \sim Gd \div (\sim Gd + \sim Gn)$$

$\sim Gd$ =Frames in which gun is not exist and is detected

$\sim Gn$ =Frames in which gun is not exist and not detected.

True negative (TN)

Gun does not exist in the frame and nothing is detected.

$$3. Tn = \sim Gn \div (\sim Gn + \sim Gd)$$

$\sim Gn$ = Frames in which the gun is not existed and is not detected

$\sim Gd$ = Frames in which the gun is not existed and is detected

False negative (FN)

Gun exist in the frame but it is not detected

$$4. Fn = Gn \div (Gn + Gd)$$

Gd=Frames in which gun exist and is detected

Gn=Frames in which gun exist but not detected

Precision (P)

In relation to all instances, the rate of correctly detected gun instances is measured by precision.

$$5. P = Tp \div (Tp + Fp)$$

Accuracy (Acc)

In relation to all instances, the overall rate of the correctly detected gun is measured by the accuracy.

$$6. Acc = (Tp + Tn) \div (Tp + Fp + Tn + Fn)$$

Figure 4 shows some sample images from a data set in which some are positive frames and some are negative frames.

The experimental results of the cascade classifier are shown in Figure 5. As shown in the Figure, the bounding box around the gun ensures the detection of the gun in all test images. Similarly,

Figure 6(a) show an example input image of individuals carrying firearm from the dataset that is being analyzed. Figure 6 (b) shows the output of the proposed gun detection algorithm applied to the input image. The output image includes a bounding box around the detected gun in the input image. This is achieved using the proposed method, where the algorithm searches for specific features or patterns that are characteristic of guns and then locates and highlights these areas in the input image.

The purpose of presenting this information is to demonstrate the effectiveness of the proposed algorithm in accurately detecting guns in CCTV images, which can aid law enforcement agencies in preventing and solving crimes involving firearms.

In Table 2 we present the experimental results. In the initial stage of experiments, the system creates too many false alarms in the whole sequence of frames which makes the system unusable in a real scenario. To solve this problem, we increase the number of frames and did strong classification to reduce these false alarms. As a result, we noted a significant improvement in the accuracy and achieved an excellent result for the proposed system. Although the system misses some detection of the gun but does not generate too many false alarms for negative frames.

Table 3 shows a summary of the dataset used for training or testing the algorithm. It includes the total number of frames collected for the dataset. The number of frames containing guns (positive frames) and the number of frames without guns (negative frames). The number of images used for positive and negative frames.

Table 2. Experimental results of the proposed method

Evaluation metrics	Values
True Positive (TP)	91%
False Positive (FP)	12.5%
True Negative (TN)	87%
False Negative (FN)	8%
Precision (P)	98%
Accuracy (ACC)	95%

Table 3. Frames and number of images used in the experiments

Frames	No. of images
Positive frames	1100
Negative frames	1300
Total frames	2400

4. DISCUSSION

The proposed system uses HAAR-like features. HAAR-like features are rectangular patterns that are used to detect edges, lines, and other visual features in an image [32]. These features are calculated by comparing the pixel values in different regions of an image. A gun has a unique interest point which can be easily detected as a corner i.e., Barrel and Trigger guard therefore, this was the fact which is used in the proposed system. To use HAAR-like

features for gun detection in CCTV images, we have trained the proposed algorithm to recognize the specific patterns associated with guns. This would involve collecting a large dataset of images containing guns and images without guns, and then using the HAAR-like features to train the algorithm to distinguish between the two. Once the proposed algorithm has been trained, it can be used to analyze new CCTV images in real-time to detect the presence of guns. If a gun is detected, the system could trigger an alarm or alert security personnel.

It is worth noting that while HAAR-like features can be effective for object detection, their performance can be affected by factors such as lighting conditions, image quality, and the size and orientation of the object being detected [33]. Therefore, it is important to carefully design and test any system that uses HAAR-like features for gun detection to ensure that it is accurate and reliable.

The proposed system can efficiently and accurately work in an indoor environment where the scene is clearly visible. In the outdoor environment, the system cannot properly detect the gun due to the presence of other objects in the scene. In an outdoor environment, the speed and accuracy of

**Fig 4.** Some samples from training and testing datasets.

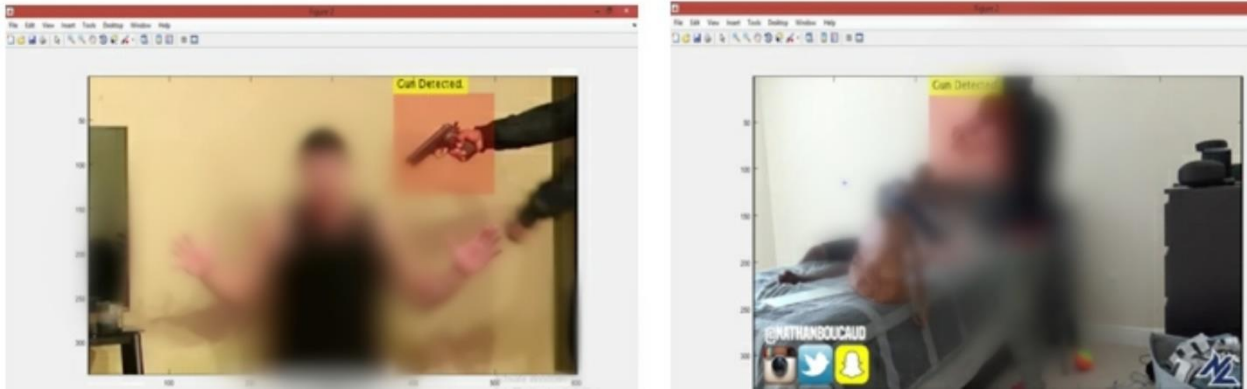


Fig 5. Results of the cascade classifier



Fig 6. (a) Input image (b) output image

the proposed system will compromise efficiency and accuracy while searching for the gun. The performance of the proposed system is also affected when a sudden illumination change occurs in the scene or the scene is not clearly visible.

5. CONCLUSION

A comprehensive approach to indoor security that includes alarms, surveillance, access control, and staff training can help to create a safer and more secure environment for individuals inside the building. In this work, an automated system for gun detection has been presented. Unlike the existing methods, the proposed method detect gun without background subtraction and foreground detection. The proposed method always tries to detect only the gun in the whole scene. HAAR cascade classifier makes it possible to detect the gun in real time. Our proposed method also searches for the gun in an expected size. In the proposed method, only pistol and shotgun is detected in the current video. The

proposed automatic gunshot detection system can provide important benefits for security and safety in indoor environments. By quickly detecting gunshots and immediately alerting authorities or security personnel, response times can be improved and potential harm to individuals in the area can be minimized. However, the proposed method cannot differentiate between the other types of guns. In future work, the focus will be to differentiate between other types of guns and to detect gun of any size. Moreover, future work also includes determining whether the gun is real or not.

6. ACKNOWLEDGMENTS

The authors thank the editor and anonymous reviewers for their helpful comments and valuable suggestions.

7. CONFLICT OF INTEREST

The authors declare no conflict of interest.

8. REFERENCES

1. M.T. Bhatti, M.G. Khan, M. Aslam, and M.J. Fiaz. Weapon detection in real-time cctv videos using deep learning. *IEEE Access* 9: 34366-34382 (2021).
2. D. Qi, W. Tan, Z. Liu, Q. Yao, and J. Liu. A Dataset and System for Real-Time Gun Detection in Surveillance Video Using Deep Learning. *2021 IEEE International Conference on Systems, Man, and Cybernetics (SMC)* 667-672 (2021).
3. S. U. Rahman, S. A. Khan, and F. Alam. An Algorithm for Human Pose Estimation from CCTV Images. *International Journal of Education (IJE)* 3: (2019).
4. T. R. Kumar, and G. K. Verma. A computer vision-based framework for visual gun detection using harris interest point detector. *Procedia Computer Science* 54: 703-712 (2015).
5. G. Arya. Automatic and Accurate Weapons Detection Model Using an Optimal Neural Network Architecture. SSRN 4172293 (2022). <https://ssrn.com/abstract=4172293> (accessed 22 November 2022)
6. K. Akhila, and K. R. Ahmed. Firearm Detection Using Deep Learning. *Intelligent Systems and Applications: Proceedings of the 2022 Intelligent Systems Conference (IntelliSys)* 544: 200-218 (2022).
7. P. K. Yeong, and S.Y. Hwang. An improved Haar-like feature for efficient object detection. *Pattern Recognition Letters* 42: 148-153 (2014).
8. I.T. Darker, A.G. Gale, and A. Blechko. CCTV as an automated sensor for firearms detection: Human-derived performance as a precursor to automatic recognition. *Unmanned/Unattended Sensors and Sensor Networks V* 7112: 12 (2008).
9. Z. Xue, R.S. Blum, Y.X. Li, R. Zhiyun, S. Blum, and Y. Li. Fusion of visual and IR images for concealed weapon detection. *Proceedings of the Fifth International Conference on Information Fusion 2*: 1198-1205 (2002).
10. I. T. Darker, A. Gale, L. Ward, A. Blechko, and K. Purdy. Light camera action and arrest. *Contemporary Ergonomics* 2007: 171-177 (2007).
11. B. Prof, K. Samir, B. Datta, and S. Roy. Identifications of concealed weapon in a Human Body. *arXiv preprint arXiv 1210.5653* (2012).
12. M. Roomi, and R. Rajashankarii. Detection of concealed weapons in x-ray images using fuzzy k-nn. *International Journal of Computer Science, Engineering and Information Technology* 2: 187-196 (2012).
13. B. Khajone, and V.K. Shandilya. Concealed Weapon Detection Using Image Processing. *International Journal of Scientific and Engineering Research* 3: 1-4 (2012).
14. D.M. Sheen, T.E. Hall, D.L. McMakin, A.M. Jones, and J.R. Tedeschi. Three-dimensional radar imaging techniques and systems for near-field applications. *Radar Sensor Technology, International Society for Optics and Photonics* 9829: 98290V (2016).
15. M. Grega, A. Matiolański, P. Guzik, and M. Leszczuk. Automated detection of firearms and knives in a CCTV image. *Sensors* 16: 47 (2016).
16. J. Dever, N. V. Lobo, and M. Shah. Automatic visual recognition of armed robbery. *Pattern Recognition, 2002. Proceedings. 16th International Conference on* 1: 451-455 (2002).
17. G. Andrzej, M. Kmiec, and A. Dziech. Visual detection of knives in security applications using Active Appearance Models. *Multimedia Tools and Applications* 74: 4253-4267 (2015).
18. G. Richard, C. Saritac, and C. C. Hung. Automatic image analysis process for the detection of concealed weapons. *Proceedings of the 5th Annual Workshop on Cyber Security and Information Intelligence Research: Cyber Security and Information Intelligence Challenges and Strategies* 20: 1-4 (2009).
19. D. G. Lowe. Distinctive image features from scale-invariant keypoints. *International journal of computer vision* 60: 91-110 (2004).
20. G.L. Foresti, C. Micheloni, L. Snidaro, P. Remagnino, T. Ellis. Active video-based surveillance system: the low-level image and video processing techniques needed for implementation. *IEEE Signal Processing Magazine* 22: 25-37 (2005).
21. K. Veena, K. Kasemsan, and C. Srisa-an. 2D Gun's type classification using edge detection algorithm and SUSAN low level image processing. *2012 International Conference for Internet Technology and Secured Transactions, London, UK 2012*: 521-523 (2012).
22. G. Michał, S. Łach, and R. Sieradzki. Automated recognition of firearms in surveillance video. *2013 IEEE International Multi-Disciplinary Conference on Cognitive Methods in Situation Awareness and Decision Support (CogSIMA), San Diego, CA, USA 2013*: 45-50 (2013).
23. H.M. Dee, and S.A. Velastin. How close are we to solving the problem of automated visual surveillance? *Machine Vision and Applications* 19:

- 329-343, (2008).
24. M. Spirito, C.S. Regazzoni, and L. Marcenaro. Automatic detection of dangerous events for underground surveillance. *IEEE Conference on Advanced Video and Signal Based Surveillance, 2005.*, Como, Italy 2005: 195-200 (2005).
 25. C.K. Lee, M.F. Ho, W.S. Wen, and C.L. Huang. Abnormal event detection in video using n-cut clustering. *Second International Conference on Intelligent Information Hiding and Multimedia Signal Processing (IIH-MSP 2006)*, Pasadena, California, USA, December 2006: 18-20 (2006).
 26. C. C. Hung, J. W. Hsieh, and K.C. Fan. Suspicious object detection and robbery event analysis. *Computer Communications and Networks 2007. ICCCN 2007. Proceedings of 16th International Conference 2007*: 1189-1192 (2007).
 27. H. Ismail, D. Harwood, and L. S. Davis. W4: Real-time surveillance of people and their activities. *IEEE Transactions on Pattern Analysis & Machine Intelligence* 8: 809-830 (2000).
 28. C. P. Papageorgiou, M. Oren and T. Poggio. A general framework for object detection. *Sixth International Conference on Computer Vision (IEEE Cat. No.98CH36271)*, Bombay, India 1998: 555-562, (1998).
 29. P. Viola, and M. Jones. Rapid object detection using a boosted cascade of simple features. *Proceedings of the 2001 IEEE Computer Society Conference on Computer Vision and Pattern Recognition. CVPR 2001, Kauai, HI, USA 2001*: I-I, (2001).
 30. S.Z. Li, L. Zhu, Z. Zhang, A. Blake, H. Zhang, and H. Shum. Statistical learning of multiview face detection. *Proceedings of the European Conference on Computer Vision London, UK 2353*: 67-81 (2002).
 31. M. Jones, and P. Viola. Fast multi-view face detection. *CTIT technical reports series* (2003).
 32. P. Sri-Kaushik, D. Delgado, and A. F. Frangi. Haar-like features with optimally weighted rectangles for rapid object detection. *Pattern Recognition* 43: 160-172 (2010).
 33. S. Asnani, A. Ahmed, and A. A. Manjotho. Bank Security System based on Weapon Detection using HOG Features. *Asian Journal of Engineering, Sciences & Technology* 4: (2014).



Design and Implementation of Low-Cost Data Acquisition System for Small and Medium Enterprises (SMEs) of Pakistan

Muhammad Imran Majid*, Ejaz Malik, Tahniyat Aslam, Osama Mahfooz,
and Fatima Maqbool

Electrical Engineering Department, Institute of Business Management (IoBM),
Karachi, Pakistan

Abstract: This paper presents the development of low-cost and robust industrial IoT based data acquisition system primarily focused on domestic manufacturing industries striving to achieve goals and benefits of “Industrial 4.0”. This proposes aims to promote DAQ System integration in traditional manufacturing process of the small and mid-sized industries of Pakistan with limited capacity of investment. Proposed method comprises of Arduino and it’s IoT features for Data Collection, along with a self-developed PC based Centralized Software for Collection of Data, Graphical User Display and Storing collected Data in Local SQL Database. PC based Software replaces requirement of multiple software in case of traditional low-cost DAQ systems, like OPC Software for collecting data from industrial hardware, Java or PHP based any GUI and SQL Data storage. The analysis of work is done with the help of the Message Queue Telemetry Transport (MQTT) protocol. This project will be in further stages evaluated to add features of Supervisory Control, along with Data Acquisition hardware with minimum increase in cost and further upgrading PC Software to add more features of Industry 4.0, as compared to costly commercial solutions available in the market. A machine learning algorithm, k-nearest neighbors algorithm has been used to classify sensitive and non-sensitive data for improvising cloud security. K-Nearest Neighbors is also called KNN algorithm which is supervised machine learning classifier.

Keywords: Industry 4.0, Arduino, IoT, UDP/TCP, PC Software, Database, MQTT

1. INTRODUCTION

A recent World Economic Forum status report detailing 21 tipping points that will change the world uptill 2025 which will leave a deepend impact on the way we perceive technology and society. The concept referred to as Industry 4.0 has revolutionized Manufacturing Process with the help of Information and Communication Technologies (ICT) manufacturing Operations systems – forming Cyber Physical Systems (CPS). Due to this industrial revolution, the market is transformed into considering the full value chain and changed the way an organization operates [1]. Many countries have contributed in creating domestic programs to improve the development and acceptance of Industry 4.0 technologies. In deutechland, the

concept of “High-Tech Strategy 2020”, in US “Advanced Manufacturing Partnership”, whereas in Sinoland the “Made in China 2025” alongwith the french “La Nouvelle France Industrielle” has been gaining ground [2].

To communicate between machines and devices requires customizable configurations products, especially for small quantity numbers [3]. Moreover, Cyber phsycial systems are used to process data and information, to enable entitties to have a quicker response to enable resource utilization[4]. Hence, autonomous systems and smart grids using smart grids and power savings helps improve efficiency [5]. There has been a lot of emphasis on practical implications and utilization of technology related to Industry 4.0 [6] [7] [8] [9]. Lutfi et al. [10] have

implemented Accounting Information System to facilitate SMEs. A computerised accounting system (AIS) enables us to achieve accurate data collection, handles large-scale transactions, and creates useful reporting for evaluation. Given the lack of AIS implementation in SMEs, despite its significant benefits, the purpose of this study is to investigate the antecedents of AIS implementation and their implications for long-term business performance in Jordanian SMEs.

As seen in Table 1, there are a number of emerging technologies that are linked to the futuristic fourth industrial revolution [5].

Our research area mainly focuses on Data Acquisition systems, which is an integral part of Supervisory Control and Data Acquisition Systems (SCADA), one of the unique and competitive technologies of the industry 4.0. In this research paper, first known attempt of design and implementation of low-cost Data Acquisition system is made. Instead of using PLCs and Data loggers in conventional SCADA systems. Figure 1 is showing the system design. Overall system consists of two main parts, i.e., Arduino (Ethernet) based Nodes, installed on Ethernet Shield W5100, Self-designed IO Shield and C# based software for acquiring Data, storing Data in Local SQL Database and Displaying Data in Real Time using UDP Protocol, for minimal cost and adequate accuracy and communication speed.

2. METHODOLOGY

The multi channel data acquisition system is

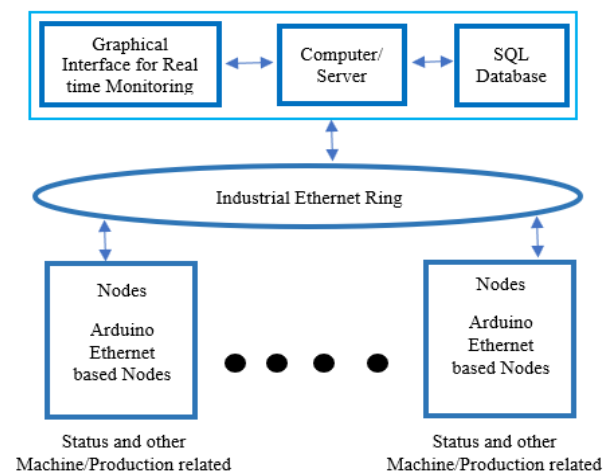


Fig. 1. Block level representation of System Design

revealed in terms of hardware and software description. Work flow demonstration of system design is clearly shown in Figure 1.

Machines to collect Machine's status and other relevant data, their communication to Data Acquisition Server using User Datagram Protocol (UDP) and Data Acquisition Application Software for Data Collection, Displaying Real time Machine Status and other Relevant Data as well as Storing Data in SQL Server as per requirement of User. There are two parts of the system hardware and software. For the software part algorithm is presented. For PCB hardware, pictorial view of front and side is provided. Installed view is also given in the Figure 2, 3 and 4 respectively.



Fig. 2. PCB Hardware design (Front View)

2.1 Hardware Design

Hardware of each Node comprises of Arduino Mega, with its Ethernet Shield W5100 along with Fabricated Digital IOs Shields. Digital IOs Shield is used to convert 24VDC signals from Industrial Sensors and Relays to 5VDC signal which is compatible to Arduino Mega Voltages. Each Digital IOs Shield has 12 channels of 24VDC Input (Sink), total of 3 IOs Shield (36 Channels) are utilized for testing. Ethernet Shield (W5100 Chipset) is used for communicating to Data Acquisition Software. Arduino Mega is selected due to highest number of available Digital IOs over other models of Arduino Family.

Figures 2, 3 and 4 show the PCB hardware design and installation. The following Flow Chart describes the overall working of Arduino Ethernet based Nodes.

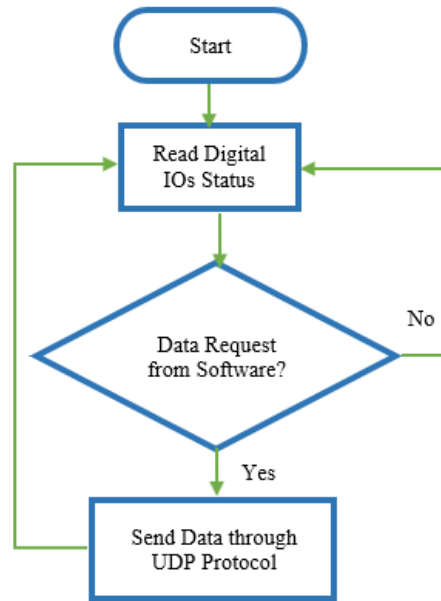


Table 1. Technologies of 4.0

Technologies	Definition
Computer-Aided Design and Manufacturing [CAD/CAM]	Development of projects and work plans for product and manufacturing based on computerized systems (Scheer, 1994).
Integrated engineering systems [ENG_SYS]	Integration of IT support systems for information exchange in product development and manufacturing (Kagermann et al., 2013; Bruun et al., 2015; Abramovici, 2007).
Digital automation with sensors [SENSORING]	Automation systems with embedded sensor technology for monitoring through data gathering (Saldivar et al., 2015).
Flexible manufacturing lines [FLEXIBLE]	Digital automation with sensor technology in manufacturing processes (e.g. radio frequency identification – RFID – in product components and raw material), to promote Reconfigurable Manufacturing Systems (RMS) and to enable the integration and rearrangement of the product with the industrial environment in a cost-efficient way (Brettel et al., 2014; Abele et al., 2007).
Manufacturing Execution Systems (MES) and Supervisory control and data acquisition (SCADA) [MES/SCADA]	Monitoring of shop floor with real time data collection using SCADA and remote control of production, transforming long-term scheduling in short term orders considering restrictions, with MES (Jeschke et al., 2017).
Simulations/analysis of virtual models [VIRTUAL]	Finite Elements, Computational Fluid Dynamics, etc. for engineering projects and commissioning model-based design of systems, where synthesized models simulates properties of the implemented model (Saldivar et al., 2015; Babiceanu and Seker, 2016).
Big data collection and analysis [BIG_DATA]	Correlation of great quantities of data for applications in predictive analytics, data mining, statistical analysis and others (Gilchrist, 2016).
Digital Product-Service Systems [DIGITAL_SERV]	Incorporation of digital services in products based on IoT platforms, embedded sensors, processors, and software enabling new capabilities (Porter and Heppelmann, 2014).
Additive manufacturing, fast prototyping or 3D impression [ADDITIVE]	Versatile manufacturing machines for flexible manufacturing systems (FMS), transforming digital 3D models into physical products (Weller et al., 2015; Garrett, 2014).
Cloud services for products [CLOUD]	Application of cloud computing in products, extending their capabilities and related services (Porter and Heppelmann, 2014).



Fig. 3. PCB Hardware design (Side View)



Fig. 4. Hardware installed at Site

2.2 Software Design

In this section, software of the Data acquisition system is explained. Software is developed using C# language-based Windows Forms. C# is used for 1- Collecting Data from Arduino via UDP Protocol, using Socket Programming as well as 2- Display collected data in real time on Windows Forms and 3- Store and retrieve that collected Data from SQL Database on timer based or on the request of the User/Operator. This self-developed software does not have any limitations of usage as like using any free OPC Software for data collection, also this software is a low-cost variant of any commercial run time Monitoring software or GUI.

2.3 Data Collection Layer

Collection of Data consist of Polling Mechanism. C# based software makes regular data requests to Controller (Arduino) to obtain field system data and store it in system database.

Arduino is equipped with Ethernet Interface via W5100 Ethernet Shield and uses Ethernet/IP Protocol for data communication. Communication Process is as follows: C# Software sends the data request to Arduino via Ethernet/IP Protocols. Ethernet/IP has UDP, TCP two communication protocols to choose from, because C# software (Server) is only responsible for sending “request packets”, Arduino is only responsible for sending “reply packets”, so the communication process does not need to use the connection-based TCP Protocol, but directly uses the UDP Protocol, which does not require high reliability and ensure the rate of data transmission.

2.4 Data Storage and Display

Collected data is analyzed using Main C# Software, according to user requirements. In our test case, Data must be stored if it's changed from its previous value. i.e. If “Status” of any Arduino Digital Inputs (36 Inputs, Channels in our Test) is changed from its previous value, then this “new value” of that “Input” must be stored in the Database with current Timestamp, with its “Input Number”. Values are being stored in Local SQL Database in test case, using Microsoft SQL Server. MS SQL Server is

already being used in the Test company/Industry, makes it our first choice to work with. “Status” of Arduino Input Pins is also displayed on the GUI, which is the part of Main C# Software. “OFF” Pins are showed in Red, and “ON” Pins are displayed as Green.

When Status of “Input” e.g. INPUT0 is ON it means Machine's Line1 is ON and is in “Production”. When Status of “Input” e.g. INPUT0 is OFF it means Machine's Line1 is OFF and is “Idle” i.e. not producing. Change in the “Status” of INPUT0 (ON to OFF) means that machine is stopped after completing a product and is now repeating its cycle to produce new item.

So if we store only “Change of Input Status” in our database, we can count how many times Machine Line1 was “ON” in 24 Hours, thus calculating amount of Production made in that day.

3. DAQ AND COMMUNICATION PROTOCOLS

A data acquisition system (DAS or DAQ) is used for sampling signals that can evaluate physical conditions and convert measured values into digital which could be used by a computer. It converts analog waveforms into digital values for processing such as temperature, pressure, current, and other measurements into digital values for controllers or computers to process. Data Acquisition hardware communicates over several communication protocols. Some of them are discussed below [11].

3.1 Transmission Control Protocol/ Internet Protocol (TCP/IP)

TCP/IP protocol suite delivers the resources to the devices, to interact with one another via an Ethernet Local-Area Network (LAN), or by Wide-Area Network (WAN). TCP/IP allows the application layer messages to transfer between the devices. But it does not assure that the devices will interoperate with each other. Ethernet/IP-based data acquisition modules communicate via Industrial Ethernet protocol via TCP/IP protocol suites and standard IEEE 802.3. These are presented in both digital and analog I/O configurations and could be integrate with the standard cabling of Ethernet [12].

3.2 Modbus

It communicates by using a client-server (master-slave) method. It includes one device either a master or client that can initiate communications known as queries. Other devices such as either servers or slaves react by delivering the requested information to the master, or by initiating a request. A slave is a device such as a network drive, I/O transducer that can process data and transfer the information to the master by using Modbus [13].

3.3 Modbus TCP/IP

It is also known as the Modbus Remote Terminal Unit (RTU) protocol with a TCP interface which operates on Ethernet. The structure of Modbus messaging is the application protocol which specifies the instructions for managing and understanding the information independent of the transmission medium. TCP/IP indicates the transmission medium for Modbus TCP/IP messaging. It allows the transmission of binary data between the processors. It is a global standard that assists as the basis for the WWW. The main feature of TCP is to confirm that all data packets are transferred properly, whereas IP makes sure that messages are routed and addressed correctly. This protocol is used in the industrial field to understand the linkage among the industrial equipments. Initially, the communication protocol was intended to support interaction between Programmable Logic Controllers (PLCs). The protocol also contains built-in checksum protection that can ensure reliable data transmission in IoT networks [13].

3.4 MQTT Protocol

Message Queue Telemetry Transport (MQTT) protocol is depend on Transmission Control Protocol (TCP). It is a protocol for IoT devices to interact with one another by using MQTT messages. The use of network resources can be decreased because the messages are lightweight in MQTT due to their optimized headers. The protocol comprises of MQTT brokers and clients. The MQTT broker can be placed in an IoT gateway, whereas the MQTT client could be an IoT actuators that can control data transmission between control commands and sensors to IoT sensors. This protocol can deliver reliable data transmission. Moreover, IoT actuators

might need to establish a link with the IoT gateway during a period. By employing MQTT brokers, IoT actuators can create a outgoing TCP protocol to allow data communication [14].

3.5 IoT CAN BUS

This protocol is created on the CAN standard. It is a lightweight, centralized, flexible, and open system which can promptly integrate with controllers, sensors, and communication devices on the IoT-CAN bus board. This protocol is applied in many applications such as industrial manufacturing agriculture observing and environmental monitoring, etc. IoT-CAN does not require a master-slave protocol to sustain the system, therefore there is no longer need for registration mechanism of the master-slave protocol, employs static ID, distributes the CAN-ID interval depending on the module type and allow standard frames [14].

Figure 5, shows that the Sensors may be connected to an IoT gateway to form an edge that collects data from sensor nodes. The raw data may be fed into a simulator box for further processing and then transmitted to an on premises server or to a remote location using an IoT platform as shown in figure 5 below. The information may then be analyzed using AI or ML techniques for predicting machine health.

The figure 6 given shows a typical architecture of an MQTT based sensor module. It consists of power supply to power up the microcontroller and the required digital or analog sensors connected to it. The amplifiers converts the intensity of current to to meet the reired power for the sensors. An lcd would display the results received from the sensors after being processed by the microcontroller.

4. MQTT FUNDAMENTALS

Many IoT applications, such as smart cities, buildings, vehicles and industries, etc., are vulnerable to attacks. Therefore, it is necessary to improve the security such as access control, secure booting and device authentication [5]. Several IoT communications are rely on the hypertext transfer protocol (HTTP) protocol, but they require larger resource requirements and latency. On the other hand, the Message Queue Telemetry Transport

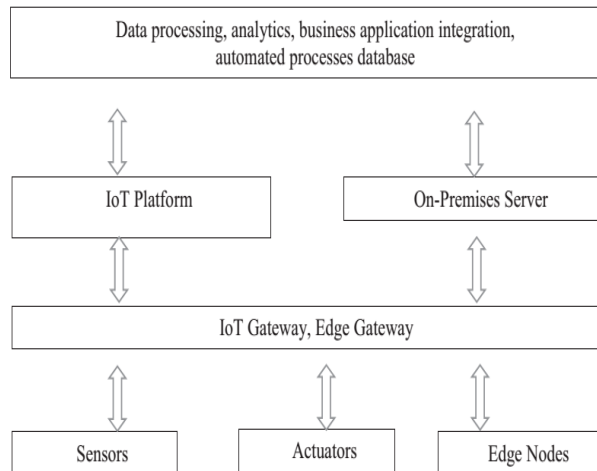


Fig. 5. IoT EDGE Architecture

(MQTT) protocol requires fewer resource requirements and employs less payload overhead packets with various quality of service (QoS), to overcome the problems of HTTP protocol. IBM released an open-source protocol called MQTT for publishing/subscribing messaging over client-server transport. The MQTT protocol are used in communication environments for the IoT and machine to machine (M2M) applications, where a low code footprint and small network bandwidth is required [6].

Figure 7, illustrates the basic setup of the MQTT communication protocol. A fundamental element is known as MQTT broker, that manages the transfer of information between the MQTT clients sending information (publisher) and the MQTT clients receiving the information (subscriber). Hence, no direct connections between the clients. But at a same time, a client can also be a subscriber and a publisher. The MQTT protocol can be deployed with the existing internal networks. Therefore, by employing proper sensor and server (broker) technology, MQTT allows a flexible and comprehensive process for monitoring. The information transmission can be done with three QoS levels by using the MQTT protocols [15].

- QoS 0 is used for only one delivery
- QoS 1 is used for at least one delivery
- QoS 2 is used for exactly-once delivery

5. TECHNOLOGICAL CONCEPT

A microcontroller (ESP32 or alternative ESP8266)

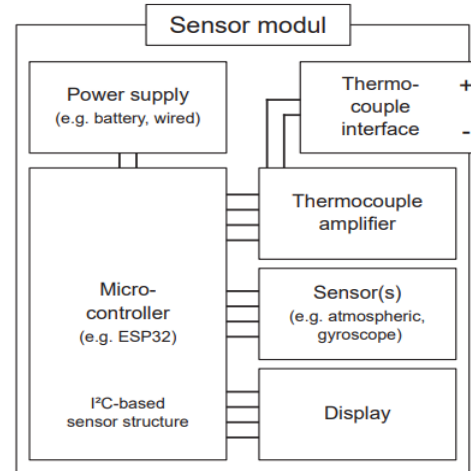


Fig. 6. MQTT Enabled Sensor Module [16]

used as the sensor module (Publisher). The publisher is integrated with the network and transfer the recorded data, collected from different sensors via MQTT protocol to a database. The sensor can be powered by a rechargeable battery (e.g. LiPo or Li-Ion) or operated by a USB connection through a power supply unit. In sensor module, the connection between an optional display and the transmission of the sensor data to the microcontroller can be done by using two different communication protocols: Serial Peripheral Interface (SPI) and Inter-Integrated Circuit (I2C). whereas, a Raspberry Pi (4 or Compute Module 4 with IO Board) equipped with the software can be serve as a MQTT broker. An existing corporate WiFi network is assumed. Figure 8, illustrate the proposed network of the project.

The proposed network lessens the burden of more processing in the cloud layer because we are getting reasonable amount of processing power at the IoT gateway which is being utilized to achieve more processing at the front of DAQ. Eventually this would affect the latency drastically and it would be reduced.

6. RESULTS & DISCUSSION

Data collected from DAQ System (as shown in Table 2) is used to calculate “Total Production” of a Machine in its 24 Hour of Operation. As previously manually count of “Total Production” was made by the Department In charge at the end of 24-Hour operation. Test results showed, that If Machine and Our system is working for 24 Hours, Data collected

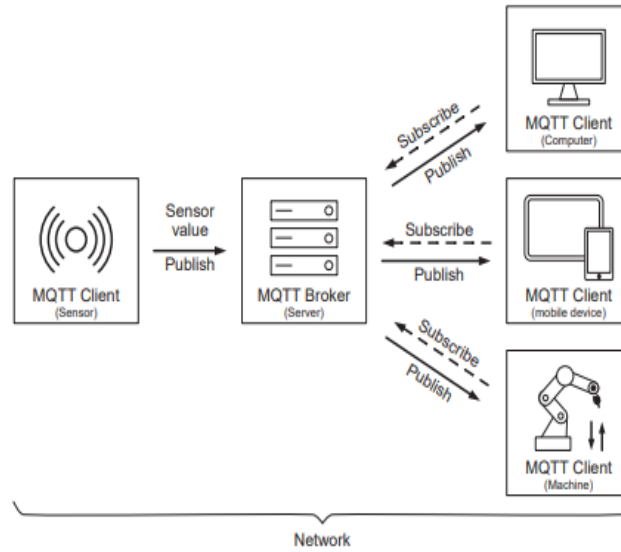


Fig. 7. MQTT communication protocol setup

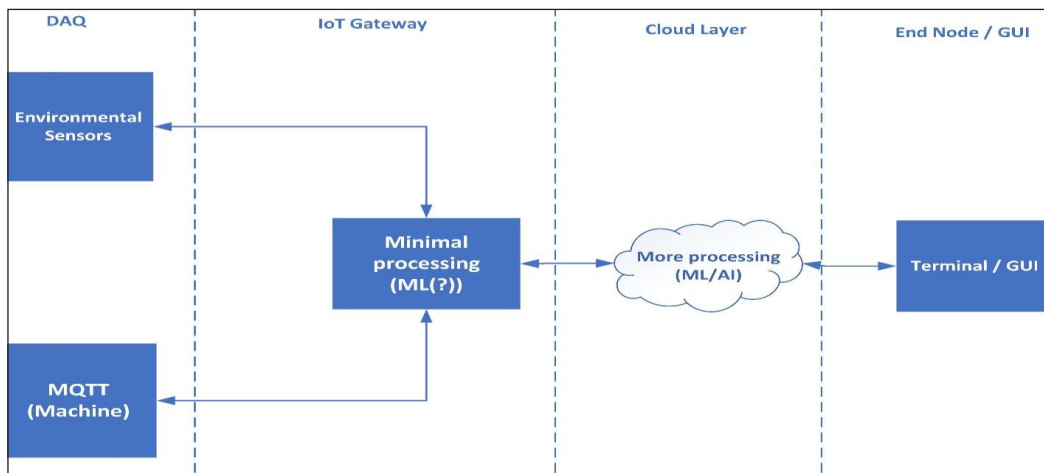


Fig. 8. Proposed Network of project

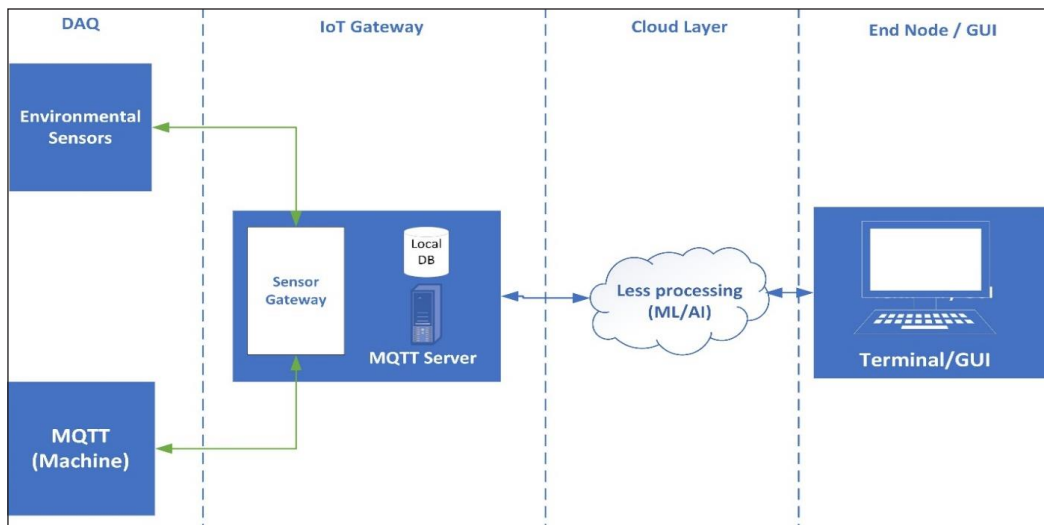


Fig. 9. Proposed Network

Table 2. Data collected from DAQ system

Day	Production count by DAQ System (Database)	Manual Production count from Production Department
Day 1	518	503
Day 2	541	575
Day 3	308	574
Day 4	404	537
Day 5	557	574
Day 6	415	539
Day 7	343	546
Day 8	432	501
Day 9	560	574
Day 10	14	180

is almost as same as Production Data collected from Production Department of our Test Site/Company.

Discussion related part includes description of Machine Learning at the edge, Edge AI, Artificial Intelligence at the cloud layer, Machine Learning at the cloud layer, K-nearest Neighbour KNN, supervised Machine Learning algorithm for cloud security and the algorithm related to the working of KNN.

As per Figure 9, the concept of DAQ based Machine Learning at the Edge and utilizing multiple NodeMCUs connected to IoT gateway can be incorporated. Here we would incorporate advanced features as in Machine Learning at the edge as well as AI/ML at the cloud layer.

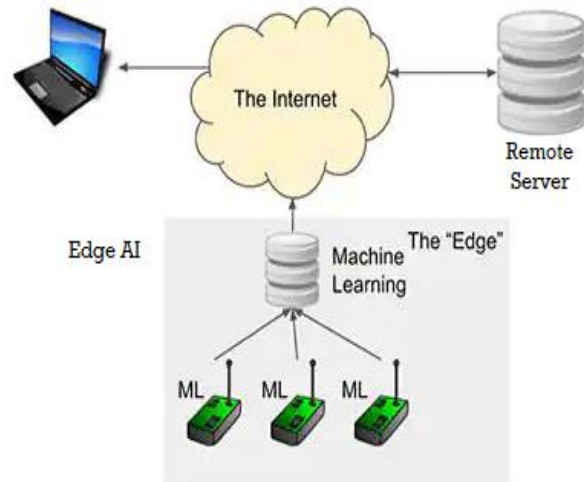
6.1 Machine Learning at the Edge

Machine Learning at the edge (ML@Edge) concept refers to Machine Learning based models' capability to edge devices to collect data from the sources which are on the distance from cloud [17]. ML@Edge can be beneficial for security and safety purpose, predictive maintenance and detection of defects in production lines [18].

6.2 Edge AI

Edge AI is a buzz word in today's world. Edge computing is the combination of various techniques which are employed for data collection, data analysis and processing of data into the network [19]. Whereas, Artificial Intelligence refers to computing technique which made machine intelligent to take decision. Integration of Artificial Intelligence with

Edge Computing is known as Edge AI. Edge AI can fasten the data processing, make network more secure and efficient [20]. Figure 10 is showing role of ML and AI at the Edge [21], [22].

**Fig. 10.** AI and ML at the Edge [21], [22]

6.3 Artificial Intelligence at the Cloud Layer

The combination of Artificial Intelligence and Cloud Computing is emerging as business forward in the various ways beyond Information Technology (IT) [23]. AI based algorithms are applied in cloud computing to provide customer more effective services with the help experience. The two most common examples are Siri and Alexa [24].

6.4 Machine Learning at the Cloud Layer

Machine Learning has enhanced the capability of cloud computing with the help of various algorithms used for binary prediction, value prediction and category prediction. Machine Learning algorithms can help in predicting and forecasting business trends and help organizations in making decisions. Machine Learning as a Service (MLaaS) has become very powerful tool to train the data and make it cost effective [25]. Figure 11, is showing Machine Learning as a Service for cloud Computing [26].

6.5 Machine Learning Algorithm for Cloud Security

Various machine learning algorithms such as Artificial Neural Networks (ANN), K Nearest

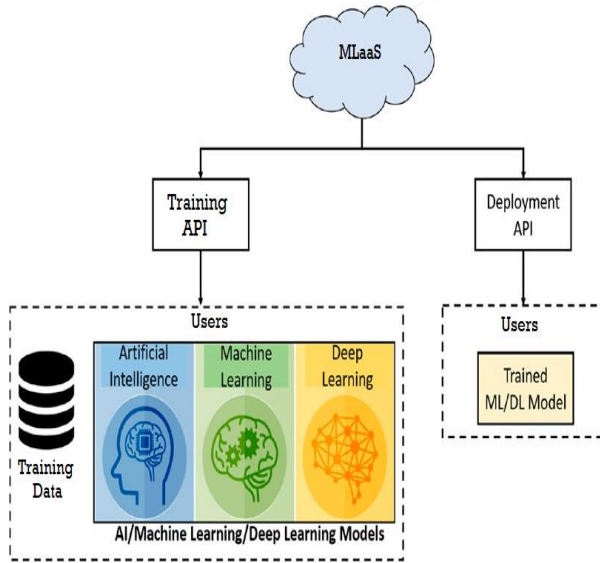


Fig. 11. Machine Learning as a Service (MLaaS) [26]

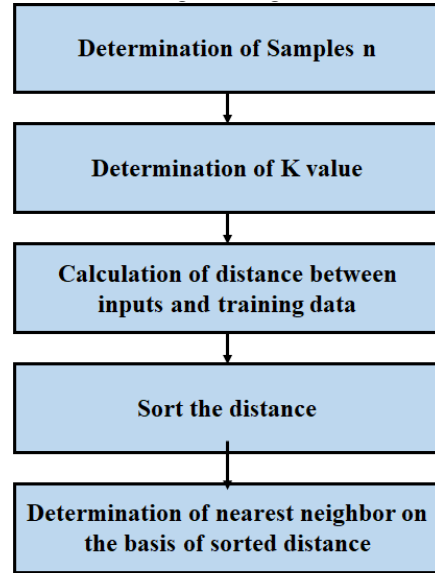


Fig. 12. KNN Classifier Working [27]

Table 3. Classification of Data using KNN [27]

Before Classification		After Classification				
Total Size of File (KB)	Total Record In File	Class-1		Class-2		Time Taken by KNN Classifier in (mS)
		Size	Record	Size	Record	
512	5094	352	3450	160	1644	1075

Neighbor (KNN), Naïve Bayes and Logistic regression can be used to improvise cloud security [27]. In this paper, we have reviewed use of KNN for cloud security management.

6.6 KNN for Improving Cloud Security

The K Nearest Neighbor comes under supervised machine learning algorithm. This algorithm is used for pattern recognition, estimation, classification and prediction. In KNN, there is n number of labelled or defined samples [28].

$$D=\{d1,d2,d3.....dn\}$$

Where D is representing total number of samples and d1,d2...dn is representing different data or samples. Figure 12, is r showing working of KNN Classifier.

KNN algorithm was used to classify sensitive and non-sensitive data. KNN has divided data into two distinct classes Class-1 and Class-2. Class-1

is representing non sensitive data whereas class-2 is representing sensitive data. KNN Classifier has taken 1075ms to classify data, as shown in Table 3.

7. CONCLUSION

The paper is an attempt to propose a novel framework for data acquisition of environment sensors positioned at a machine stationed in industry based in either textile or automotive sectors. Proposed method comprises of Arduino and its IoT features for Data Collection, along with a self-developed PC based Centralized Software for Collection of Data, Graphical User Display and Storing collected Data in Local SQL Database. The production count spread over a 24-hour period is accounted. The experimental analysis of work is done by employing a lightweight MQTT protocol. The basic network is analyzed in terms of edge computing and advanced analytics including Machine learning and Artificial Intelligence. Proposed future extensions are proposed in these domains based on the ideas presented.

8. CONFLICT OF INTEREST

The authors declare no conflict of interest.

9. REFERENCES

1. G.L. Tortorella, and D. Fettermann. Implementation of industry 4.0 and lean production in brazilian manufacturing companies. *International Journal of Production Research* 56: 2975-2987 (2018).
2. L.S. Dalenogare, G.B. Benitez, N.F. Ayala, and A. G. Frank. The expected contribution of Industry 4.0 technologies for industrial performance. *International Journal of Production Economics* 204: 383–394 (2018).
3. S. Wang, J. Wan, D. Li, and C. Zhang. Implementing Smart Factory of Industrie 4.0: An Outlook. *International Journal of Distributed Sensor Networks* 2016: (2016).
4. G. Schuh, R. Anderl, J. Gausemeier, M.T. Hompel, and W. Wahlster. *Industrie 4.0 Maturity Index Managing the Digital Transformation of Companies*. acatech STUDY (2017).
5. S. Jeschke, C. Brecher, T. Meisen, D. Özdemir, and T. Eschert. *Industrial Internet of Things and Cyber Manufacturing Systems*. *Industrial Internet of Things* 3-19 (2017).
6. G.J. Cheng, L.T. Liu, X.J. Qiang, and Y. Liu. Industry 4.0 Development and Application of Intelligent Manufacturing. *International Conference on Information System and Artificial Intelligence (ISAI)* 407-410 (2016).
7. H. Kagermann. Change Through Digitization-Value Creation in the Age of Industry 4.0. *Management of Permanent Change*, H. and P. A. and R. R. Albach Horst and Meffert, Ed. Wiesbaden: Springer Fachmedien Wiesbaden (23–45) 2015.
8. M. Rüßmann, M. Lorenz, P. Gerbert, M. Waldner, J. Justus, P. Engel, and M.J. Harnisch. *Industry 4.0 The Future of Productivity and Growth in Manufacturing Industries*. Economics, History (2016).
9. T. Stock, and G. Seliger. Opportunities of Sustainable Manufacturing in Industry 4.0. *Procedia CIRP* 40: 536-541 (2016).
10. A. Lutfi, A.L. Al-Khasawneh, M.A. Almaiah, A. Alsyouf, and M. Alrawad. Business Sustainability of Small and Medium Enterprises during the COVID-19 Pandemic: The Role of AIS Implementation. *Sustainability MDPI* 14: 5362 (2022).
11. R.A. Atmoko, R. Riantini, and M.K. Hasin. IoT real time data acquisition using MQTT protocol. *Journal of Physics: Conference Series* 853: 012003 (2017).
12. A. Sharma, S. Airan, and D. Shah. Designing C Library for MODBUS-RTU to CANBUS and MODBUS-TCP IOT Converters. *Proceedings of the 2021 Second International Conference on Electronics and Sustainable Communication Systems (ICESC)*, Coimbatore, India (2021).
13. K. Yang. B. Zhang, J. Zhang, and J. Zhu. Design of Remote-Control Inverter Based on MQTT Communication Protocol. *Proceedings of the 2021 IEEE International Conference on Mechatronics and Automation (ICMA)*, Takamatsu, Japan (1374-1378) 2021.
14. H. Gong, J. Li, R. Ni, P. Xiao, and H. Ouyang. The data acquisition and control system based on IoT-can bus. *Intelligent Automation & Soft Computing* 30: 1049–1062 (2021).
15. T. Yokotani, and Y. Sasaki. Comparison with HTTP and MQTT on required network resources for IoT. *Proceedings of the International Conference on Control, Electronics, Renewable Energy and Communications (ICCEREC)* (1–6) 2016.
16. E. Riedel. MQTT protocol for SME foundries: potential as an entry point into industry 4.0, process transparency and sustainability. *Procedia CIRP* 105: 601-606 (2022).
17. M. Verhelst, and B. Murmann. Machine Learning at the Edge. *NANO-CHIPS 2030, The Frontiers Collection book series (FRONTCOLL)* 293-322 (2020).
18. M. Polese, R. Jana, V. Kounev, K. Zhang and S. Deb. Machine Learning at the Edge: A Data-Driven Architecture with Applications to 5G Cellular Networks. *IEEE Transactions on Mobile Computing* 20: 3367-3382 (2021).
19. M. Merenda, C. Porcaro, and D. Iero. Edge Machine Learning for AI-Enabled IoT Devices: A Review. *sensors MDPI* 20: 2533 (2020).
20. E. Bertino, and S. Banerjee. Artificial Intelligence at the Edge. *A Computing Community Consortium (CCC)* (2020).
21. S. Hymel. What is Edge AI? *Machine Learning + IoT*. <https://www.digikey.com/en/maker/projects/what-is-edge-ai-machine-learning-iot/4f655838138941138aaad62c170827af>. [Accessed 26 07 2022].
22. G. Anadiotis. Machine learning at the edge: TinyML is getting big (2021). <https://www.zdnet.com/article/machine-learning-at-the-edge-tinyml-is-getting-big/>. [Accessed 26 07 2022].
23. Z.A. Mohammad, R. Belgaum, S. Musa, M.M. Alam,

- and M.S. Mazliham. Role of artificial intelligence in cloud computing, IoT and SDN: Reliability and scalability issues. *International Journal of Electrical and Computer Engineering (IJECE)*11: (2021).
24. S. Mohammed, W.C. Fang, and C. Ramos. Special issue on “artificial intelligence in cloud computing”. *Computing* 105: 507-511 (2023).
 25. A. Qayyum, A. Ijaz, M. Usama, W. Iqbal, J. Qadir, Y. Elkhatib, and A. Al-Fuqaha. Securing Machine Learning in the Cloud: A Systematic Review of Cloud Machine Learning Security. *Big Data* 3: (2020).
 26. G.B. Dasgupta. AI and its Applications in the Cloud strategy. *ISEC 2021: 14th Innovations in Software Engineering Conference (formerly known as India Software Engineering Conference)* (2021).
 27. U.A. Butt, M. Mehmood, S.B.H. Shah, R. Amin, M.W. Shaukat, D.Y. Suh, and M.J. Piran. A Review of Machine Learning Algorithms for Cloud Computing Security. *Electronics*, MDPI 9: 1379 (2020).
 28. M.A. Zardari, L.T. Jung, and N. Zakaria. K-NN Classifier for Data Confidentiality in Cloud Computing. *2014 International Conference on Computer and Information Sciences (ICCOINS)* (2014).



Modeling and Intelligent Controller Design for Reactor Regulating System of Advanced CANDU Reactor (ACR-700) in LabVIEW

Arshad Habib Malik^{1*}, Feroza Arshad², and Aftab Ahmad Memon³

¹Department of Basic Training, Chashma Centre of Nuclear Training, Pakistan Atomic Energy Commission, Chashma, Pakistan

²Department of Information System, Karachi Nuclear Power Generating Station, Pakistan Atomic Energy Commission, Karachi, Pakistan

³Department of Telecommunication Engineering, Mehran University of Engineering and Technology, Jamshoro, Pakistan

Abstract: In this research work, an Advanced CANDU Reactor of 700 MWe rating (ACR-700) is attempted for Reactor Regulating System (RRS) modeling and intelligent controller design. ACR-700 is a state-of-the-art advanced generation-III reactor. The reactor regulating system is modeled with special emphasis on internal and external reactivity devices. ACR-700 is designed with Liquid Zone Control (LZC) Model, Adjuster Banks Model, Absorber Banks Model and Shutdown Banks Model. The RRS model is a highly sophisticated model developed based on the principle of spatial nuclear reactor dynamics. The RRS model is a multivariable model. The spatial reactor dynamics is modeled based on five internal feedbacks and three feedbacks. The original controller design of RRS is comprised of a PID control algorithm. The control design is reattempted with an advanced intelligent algorithm in which the ANFIS controller is used as a modern control design tool. The new ANFIS controller is basically a multivariable controller. All the modeling of RRS is implemented in Visual Basic (VB) Software while the controller is configured in LabVIEW. A special toolkit is designed for the interfacing of Visual Basic and LabVIEW known as VBLAB. The optimization of intelligent controller parameters is carried out by Genetic Algorithm (GA). The GA-optimized intelligent controller is configured with the VB RRS model. All the variable trends are visualized in the VB environment. The proposed closed-loop ACR-700 RRS control system is tested for small perturbation Analysis and power ramp-down transient and found with excellent behavior well within the design limits. The performance of the suggested ACR-700 RRS controller is compared with the existing conventional controller. The performance of the suggested control scheme is marked with reduced oscillations and faster as compared to the existing control scheme.

Keywords: Spatial Reactor Dynamics, Intelligent Controller, GA Optimization, ACR-700, LabVIEW.

1. INTRODUCTION

A third-generation advanced CANDU reactor of 700 MWe rating is considered for modeling, control design and simulation purposes in the present research. The PWR reactor dynamics based on the first principle is addressed by Johnson *et al.* [1]. Coupled transient neutronics calculations are performed by Lam *et al.* [2] for the molten fast reactor. A PWR design tool is developed by Mollah *et al.* [3] for safety and transient analysis. The reactor kinetics simulator is designed by Hakim *et al.* [4] for

research reactor in LabVIEW. A deep learning based multi-model oriented PWR dynamics is modeled by Malik *et al.* [5] in LabVIEW. A PWR controller is designed by Mousakazemi *et al.* [6] for two-point reactor kinetics model and optimized using PSO. The PWR reactor regulating system is improved by Shim *et al.* [7] optimized by genetic algorithm. The CANDU reactor regulating system is analyzed by Cho *et al.* [8] in detail for safety analysis modeled in CATHENA computer code. A safety simulator for CANDU reactor using first principle point reactor kinetics of ACR-700 is modeled by

Boroni *et al.* [9]. A global power-based reactor regulating system of 540 MWe PHWR is addressed by Subudhi *et al.* [10]. A reactor power regulator is modeled by Volodin *et al.* [11] for CANDU-6 based on parametric settings. A modeling and spatial power controller is performed by Tiwari *et al.* [12] for 540 MWe PHWR. Research is extended by Banerjee *et al.* [13] for 700 MWe PHWR with voiding effect. An attempt is made by Darling *et al.* [14] for intelligent modeling of sodium fast reactor-based nuclear power plant for safety accident management. An Adaptive Neuro-Fuzzy Inference System (ANFIS) based intelligent controller is designed by Malik *et al.* [15] for ACP1000 nuclear power plant in LabVIEW. A detailed safety study is carried out by Shidik *et al.* [16] for ACR-700 using ACR-700 simulator in LabVIEW.

In this research work, a novel spatial reactor dynamics model of reactor regulating system of advanced CANDU reactor of 700 MWe is developed. For RRS model of ACR-700, a new discrete PID controller algorithm is developed and modern ANFIS based intelligent controller is designed and performance is evaluated. The configuration of RRS model and controller synthesis is a novel special hybrid integration of Visual Basic Software and LabVIEW Software resulting in novel development of VBLAB Toolkit. The performance of proposed intelligent controller with new gains is much smooth, oscillation free, faster and robust in reference tracking mode.

2. MATERIALS AND METHODS

2.1 ACR-700 Reactor Regulating System

ACR-700 reactor regulating system is a highly advanced and sophisticated system meant for fine and coarse power control of advanced CANDU nuclear power plant of 700 MWe. It consists of reactivity control devices. The block diagram of liquid zone control system is shown in Figure 1. Liquid zone control system consists of delay tank, liquid zone pump, liquid zone inlet control valve, liquid zone outlet isolation valve, liquid zone and PID controller.

The reactivity control in liquid zone control system is appended by incorporating reactor and rate limiter as shown in Figure 2.

The configuration of liquid zones in ACR-700 is shown in Figure 3. However, the physical visualization of liquid zones is shown in Figure 4. Practically, seven liquid zone compartments are installed in upper face while other seven are installed in lower face. The water in each liquid zone compartment is light water while moderator in Calandria is heavy water. The neutronics characteristics of both light and heavy water are entirely different. The absorption and scattering cross-sections of light water is more as compared to heavy water.

The block of complete reactor regulating system of ACR700 is shown in Figure 5.

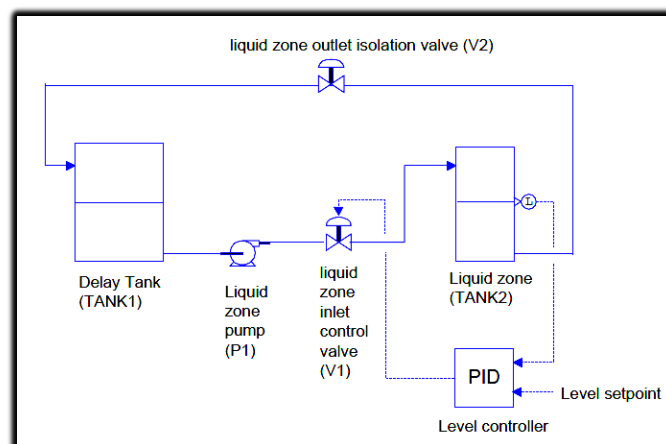


Fig. 1. Block Diagram of Liquid Zone Control System in ACR700

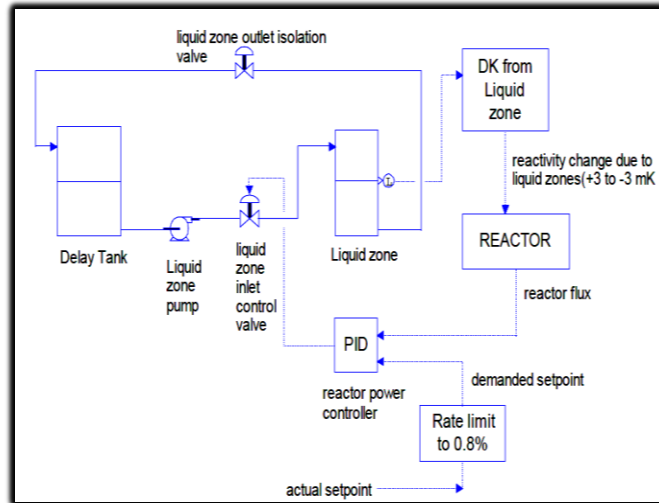


Fig. 2. Block Diagram of Reactivity Control in Liquid Zone Control System in ACR700

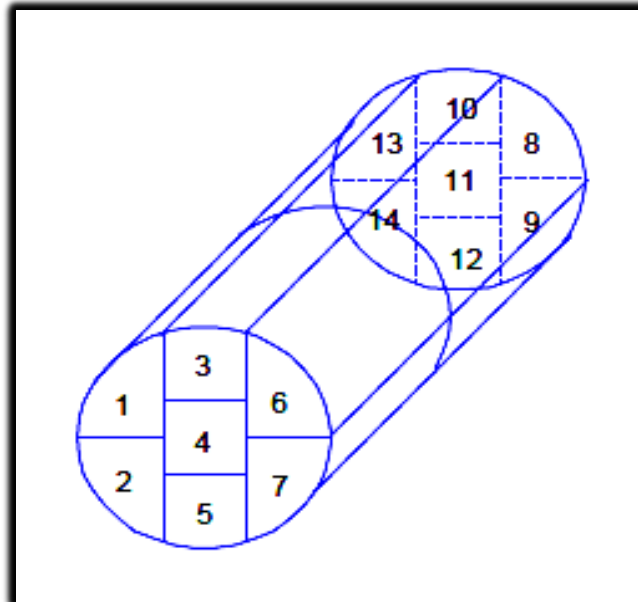


Fig. 3. Configuration of Liquid Zones in ACR700

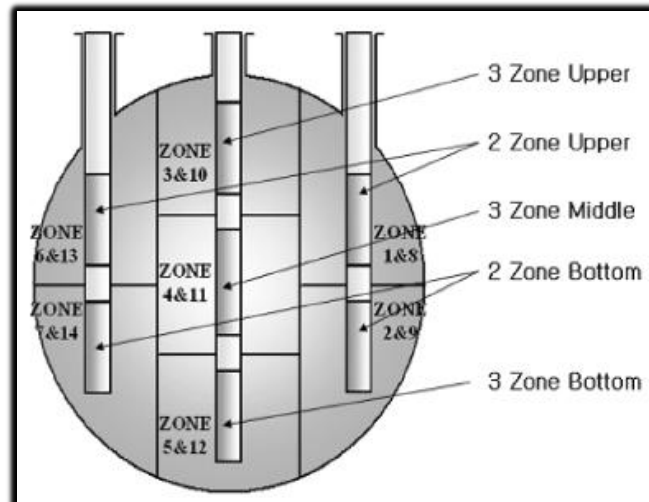


Fig. 4. Physical Visualization of Liquid Zones in ACR700

The reactor regulating system consists of fourteen liquid zones and corresponding fourteen liquid zone controllers. The water level in each zone is controlled by control valve governed by liquid zone controller. In each zone, in addition to liquid zone, there is an effect of adjuster rods, absorber rods, shut down rods and fuel burn-up. The reactor zone flux and water level in the zone is fed to liquid zone controller. Average zone level, average zone flux and power error signals are also fed to each liquid zone controller.

2.2 ACR-700 Reactor Regulating System Modeling

The reactor regulating system is modeled using i -th nodes, six fission fragments groups (j -th precursor groups) and fourteen liquid zones (k -th zones) based on spatial point kinetic model as:

$$l_i \frac{dn_i(t)}{dt} = (1 - \beta) \sum_{k=1}^{14} \alpha_{ik} n_k - n_i(t) + \sum_{k=1}^{14} \alpha_{ik} \sum_{j=1}^6 \lambda_j C_{jk} \quad (1)$$

$$\frac{dC_{jk}(t)}{dt} = \beta_j n_k(t) - \lambda_j C_{jk}(t) \quad (2)$$

Where the symbols having their usual meanings.

On re-grouping the coupling coefficients and using the definition of reactivity, equations (1) is redefined as:

$$\frac{dn_i(t)}{dt} = \frac{(\Delta K_i - \beta)}{\Lambda_i} n_i(t) + \sum_{j=1}^6 \frac{\lambda_j}{l_i} C_{ji}(t) + \frac{(1 - \beta)}{l_i} \sum_{k=1, k \neq i}^{14} \alpha_{ik} n_k(t) + \frac{1}{l_i} \sum_{k=1, k \neq i}^{14} \alpha_{ik} \sum_{j=1}^6 \lambda_j C_{jk}(t) \quad (3)$$

The overall internal reactivity change is given

$$\Delta K_{in}(t) = \Delta K_P(t) + \Delta K_V(t) + \Delta K_{Xe}(t) + \Delta K_{FUEL}(t) \quad (4)$$

The overall external reactivity change is given as:

$$\Delta K_{ex}(t) = \Delta K_{LZC}(t) + \Delta K_{ADC}(t) + \Delta K_{ABC}(t) \quad (5)$$

The overall reactivity change is given as:

$$\Delta K_i(t) = \Delta K_{in}(t) + \Delta K_{ex}(t) + \Delta K_{SDS}(t) + \Delta K_{\alpha_{ik}Z}(t) \quad (6)$$

Various parameters/symbols and variables used in the above section are defined as following:

$n(t)$ = Reactor Power

$C(t)$ = Precursor Concentration

β = Delayed Neutron Fraction

α = Coupling Coefficient

t = Neutron Life Time

ΔK = Change in Reactivity

ΔK_{in} = Change in Internal Reactivity

ΔK_{ex} = Change in External Reactivity

ΔK_P = Change in Reactivity due to Power

ΔK_{FUEL} = Change in Reactivity due to Fuel

ΔK_V = Change in Reactivity due to Voiding

ΔK_P = Change in Reactivity due to Power

ΔK_{Xe} = Change in Reactivity due to Xenon

ΔK_P = Change in Reactivity due to Power

ΔK_{LZC} = Change in Reactivity due to Liquid Zone Control

ΔK_{ADC} = Change in Reactivity due to Adjuster

ΔK_{ABC} = Change in Reactivity due to Absorber

ΔK_{SDS} = Change in Reactivity due to Shut Down System

$H(k)$ = Liquid Zone Level

$H(k-1)$ = Previous Liquid Zone Level

G = Gain

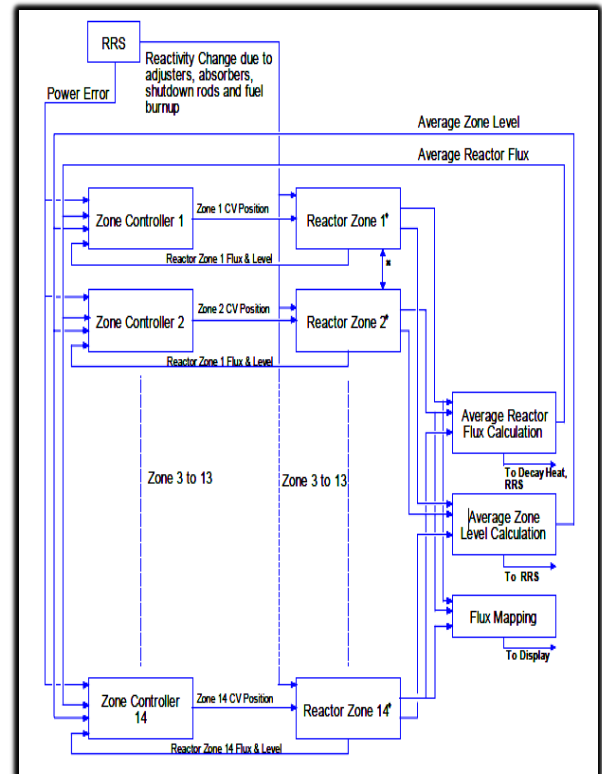


Fig. 5. Block Diagram of Reactor Regulating System (RRS) of ACR700

ep (k) = Power Error
 K = Controller
 μ = Membership Function

2.3 ACR-700 RRS Controller Framework

ACR-700 RRS controller is basically multivariable controller as shown in Figure 6.

Fig. 6 clearly shows that there are multiple set-points, multiple controlled variables and hence multiple manipulated variables.

The overall control framework of ACR-700 is shown in Figure 7. The primary coolant pressure and primary coolant flow are the disturbance signals. Figure 7 is the representation of Fig. 6 with actual details of inputs, outputs and disturbance variables used in ACR-700.

2.4 ACR-700 RRS Controller Modeling

The power error signal is computed as [6]:

$$e_p(k) = K_p \frac{[n_r(k) - n_D(k)]}{n_r(k)} + K_D \left[\frac{[n_r(k) - n_r(k-1)]}{[n_r(k)\Delta t]} - \frac{[n_r(k) - n_D(k)]}{\Delta t} \right] \quad (7)$$

The power tilt in the i-th cell of reactor core is given as:

$$P_{Ti} = K_T [n_r(k) - n_r(k)] \quad (8)$$

The bulk power control is accomplished by 8 representative zones using speed algorithm as:

$$\frac{[LZC - H(k) - LZC - H(k-1)]_k}{\Delta t} = G_1 e_p(k) + G_2 P_T + K_H [H_k(k) - H_{AV8Z}(k)] \quad (9)$$

The spatial power control is accomplished by 10 representative zones using speed algorithm as:

$$\frac{[LZC - H(k) - LZC - H(k-1)]_k}{\Delta t} = G_3 e_p(k) + G_4 [H_{AV8Z}(k) - 0.5] + G_5 [H_{AV10Z}(k) - H_k(k)] \quad (10)$$

Where the parameters/symbols have their usual meanings.

2.5 Optimization of ACR-700 RRS Existing Controller

The optimization of existing ACR-700 RRS controller is accomplished in LabVIEW as shown in Figure 8.

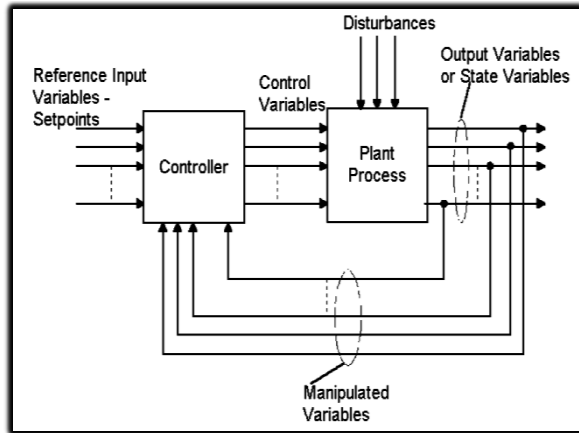


Fig. 6. Structure of Multivariable RRS Closed Loop System of ACR700

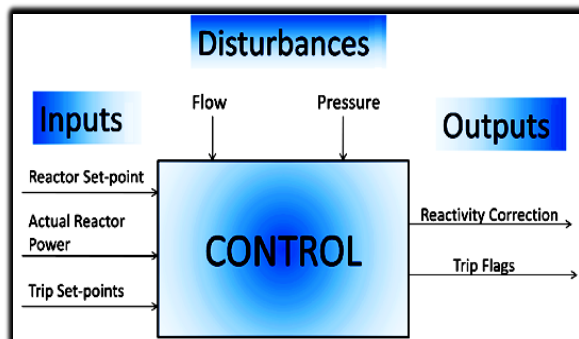


Fig. 7. Overall Control Framework of RRS in ACR700

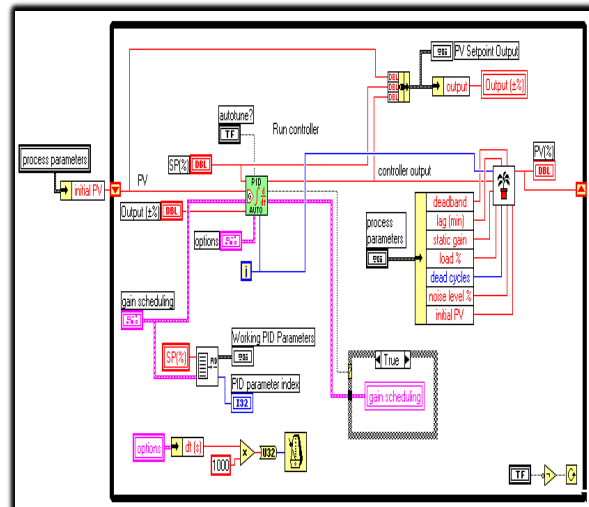


Fig. 8. Block Diagram Design for ACR700 PID Controller Design in LabVIEW

2.6 Configuration of New ACR-700 RRS Control System

The ACR-700 RRS model is configured in VB while ACR-700 RRS controller is configured in LabVIEW. The integration scheme of LabVIEW and Visual Basic is shown in Figure 9.

Fig. 9 shows the logical flow of model and controller variables transfer scheme. This scheme is basically the client and server configuration. The server configuration is in LabVIEW while the client configuration is in Visual Basic.

The configuration of new ACR-700 RRS control system is shown in Figure 10.

2.7 Intelligent ACR-700 RRS Controller Modeling

The intelligent ACR-700 RRS controller output with MISO configuration in discrete domain is given as [15]:

$$K = \frac{\sum_{l=1}^L \left(\frac{(\mu A_l(x) \mu B_l(y))(p_l x + q_l y + r_l)}{\sum_{l=1}^L (\mu A_l(x) \mu B_l(y))} \right)}{\sum_{l=1}^L (\mu A_l(x) \mu B_l(y))} \quad (11)$$

Where the parameters/symbols have their usual meanings.

2.7.1 Intelligent Controller Design for ACR-700 RRS Controller in LabVIEW

The ANFIS controller is configured in LabVIEW. The front panel design is shown in Figure 11. The block diagram of intelligent ACR-700 RRS controller is shown in Figure 12.

2.7.2 Genetic Algorithm for Optimization of Intelligent ACR-700 RRS Controller

A block diagram is designed for the process of GA initialization and optimization as shown in Figure 13. The block diagram design for the fitness function is shown in Figure 14.

3. RESULTS AND DISCUSSION

The modeling work is carried out in VB, control design, optimization and simulations work is carried out in LabVIEW.

3.1 Simulation of Proposed Closed Loop ACR-700 RRS Control System in Hybrid Framework

The detailed analysis of proposed closed loop ACR-700 RRS control system in hybrid framework is performed by taking into account the three distinct scenarios.

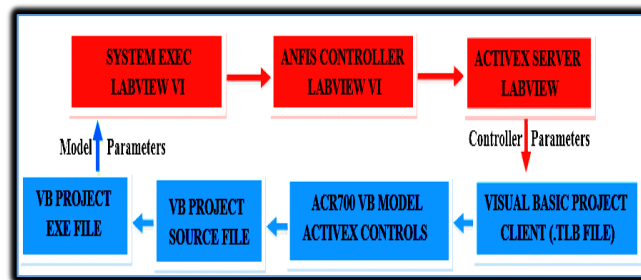


Fig. 9. Integration of LabVIEW and Visual Basic

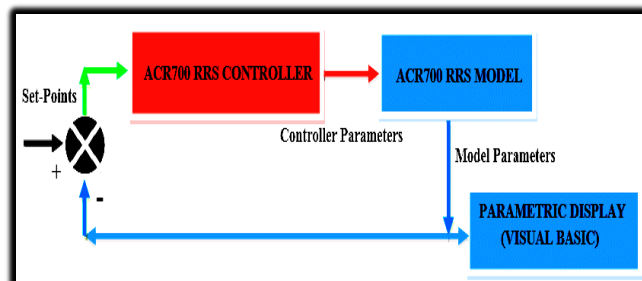


Fig. 10. Configuration of ACR700 RRS Controller and ACR700 RRS Model

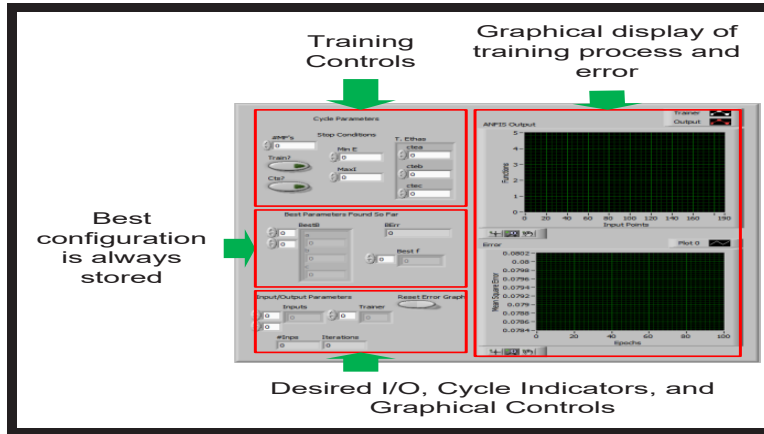


Fig. 11. Front Panel Design of ACR700 ANFIS RRS Controller in LabVIEW

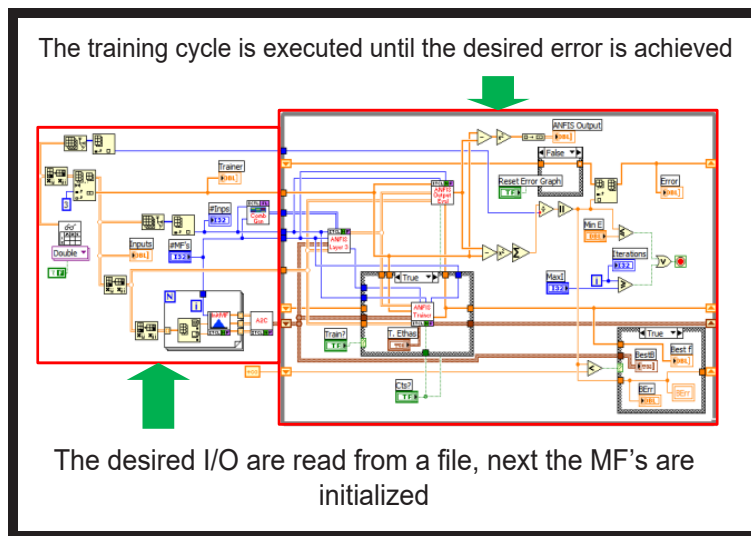


Fig. 12. Block Diagram Design of ACR700 ANFIS RRS Controller in LabVIEW

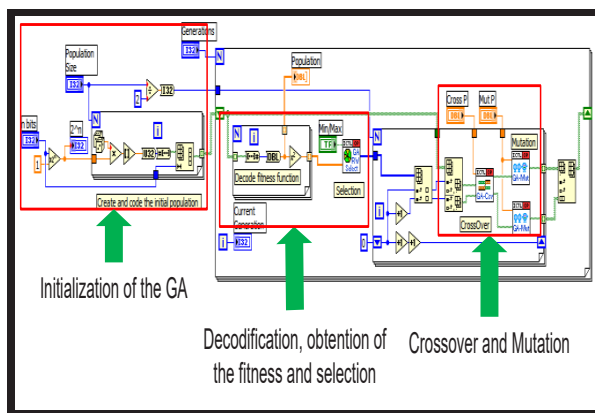


Fig. 13. Block Diagram Design of GA Optimization of ACR700 ANFIS RRS Controller in LabVIEW

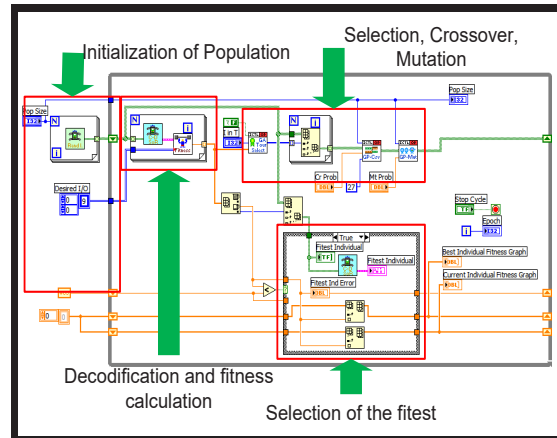


Fig. 14. Block Diagram Design for Fitness Function of GA Optimization for ACR700 ANFIS RRS Controller in LabVIEW

GA parameters are optimized based on RMSE value which is a function of PID controller output and ANFIS controller using premise parameters, consequent parameters and rules defined for the ACR-700 RRS. In this research work many attempts have been made and finally population size is chosen as 190, cross-over rate is chosen as 0.7 and mutation rate is chosen as 0.02.

In one scenario, the demand power is predicted against the set-point change as shown in Figure 15.

The power error is computed and hence the prediction of reactivity model is assessed as shown in Figure 16.

In this transient, set-point is changed in power step down fashion and hence the demanded power try to follow the set-point change based dynamics of liquid zone control system.

In second scenario, small perturbation analysis is performed, in which the reactor power is varied from 100% with $\pm 0.2\%$ i.e. the operating is 100% while deviation is allowed in steady state with maximum value of $\pm 0.2\%$ as shown in Figure 17.

The respond to this power maneuvering, the power error and compensated reactivity is computed as shown in Figure 18.

The total reactivity change of liquid zone control system against this power transient in compensation with all internal and external reactivity changes mentioned in section 2.2 is shown in Figure 19.

Now, the third scenario is selected in which the reactor power is ramp down from 100% to 98% as shown in Figure 20. Based on this power change, power error and reactivity are computed as shown in Figure 21. The power error is decreased and later on stabilized at the end of transient. Similarly, the compensated reactivity is increased as fuel burn-up is reduced and later on stabilized.

The total reactivity change due to liquid zone control is shown in Figure 22. This reactivity of liquid zone control is observed with increasing reactivity trend in compensation with all internal and external reactivity changes mentioned in section 2.2.

3.2 Performance Analysis of Proposed Closed ACR-700 RRS Control System

Now, special trending facility is developed in which performance of suggested closed loop ACR-700 RRS control system is compared with existing closed loop ACR-700 RRS control system.

Now, a low power transient is designed in which reactor power is varied from 25% to 30% through a power ramp-up transient as shown in Figure 23. This transient is designed because in ACR-700 dynamic transient at low power is the most challenging one due to highest system oscillations and fluctuations keeping in view that nuclear power plant control at low power is the most difficult scenario.

The existing control system takes oscillation at steady state while the suggested control system is found with remarkable performance and excellently tracking the set-point change.

Now the effective power error change against this transient is shown in Figure 24.

The average zone control compartment water level change is shown in Figure 25.

The zone control compartment water level error change is shown in Figure 26.

Hence, the performance of proposed closed loop ACR-700 RRS control system is proved fast, oscillation free and robust in performance in steady state, small perturbation, high power ramp-down transient and low power ramp-up transient. Therefore, the proposed control is proved an excellent practical possibility for advanced CANDU reactor such as ACR-700 nuclear power plant and future ACR-1000 nuclear power plant.

4. CONCLUSION

The reactor regulating system modeling and control of ACR-700 has been addressed in this research work. A spatial point reactor kinetics model with xenon dynamics, power dynamics, voiding dynamics, safety shut down systems dynamics, fuel burn-up dynamics, liquid control compartment dynamics, adjuster banks dynamics and absorber banks dynamics is developed in visual basic environment.

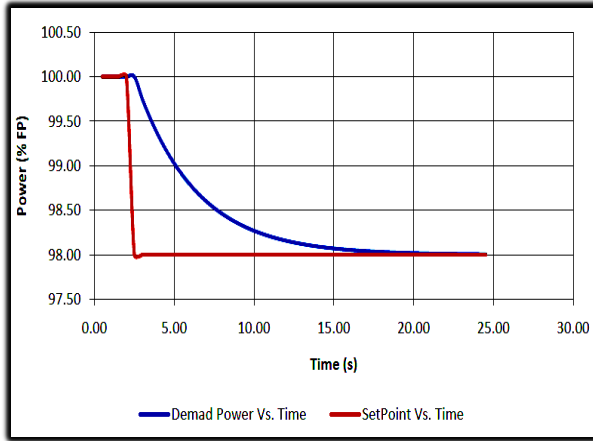


Fig. 15. Prediction of Demanded Power Model of ACR700 RRS

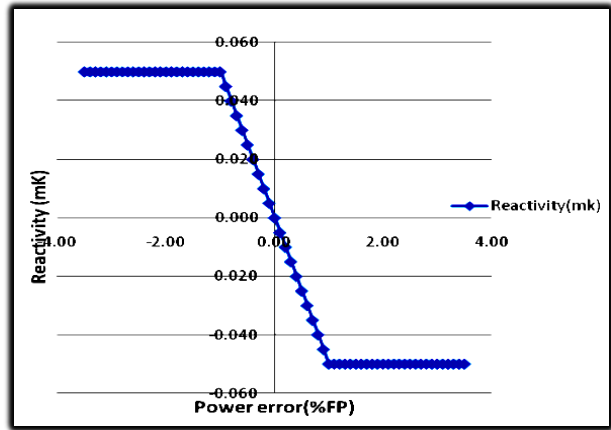


Fig. 16. Prediction of Power Error Dependent Reactivity Model of ACR700 RRS

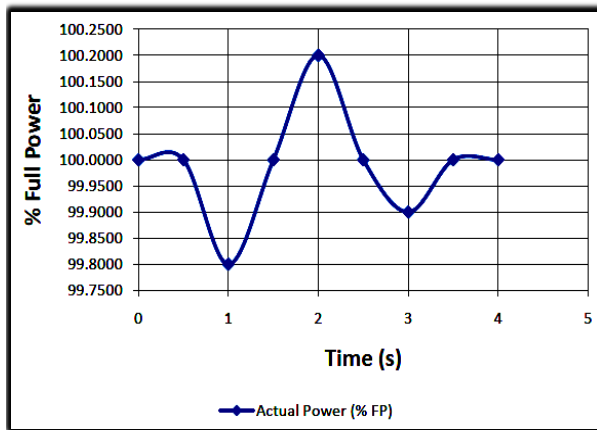


Fig. 17. Small Power Perturbation Maneuvering Transient in RRS of ACR700 RRS

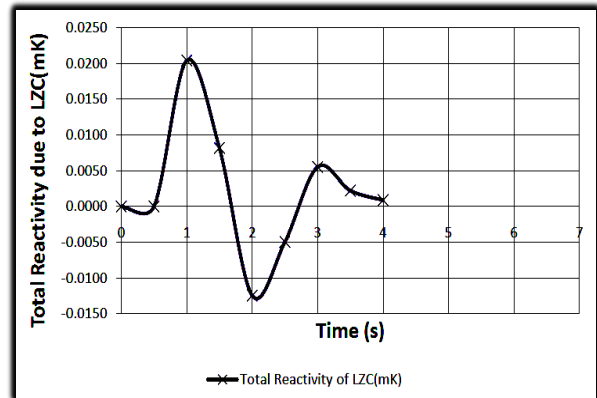


Fig. 18. Prediction of Power Error and Reactivity under Small Power Perturbation Maneuvering Transient of ACR700 RRS

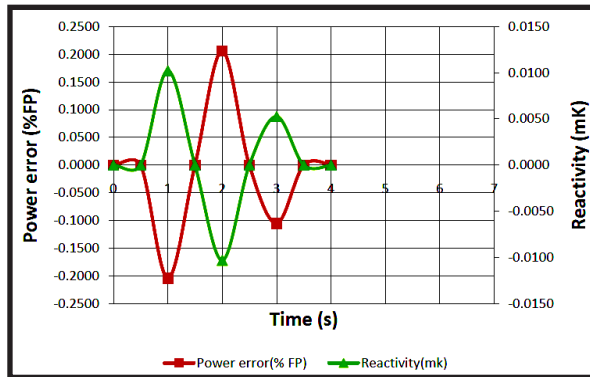


Fig. 19. Prediction of Total Reactivity of Liquid Zone Control System under Small Power Perturbation Maneuvering Transient of ACR700 RRS

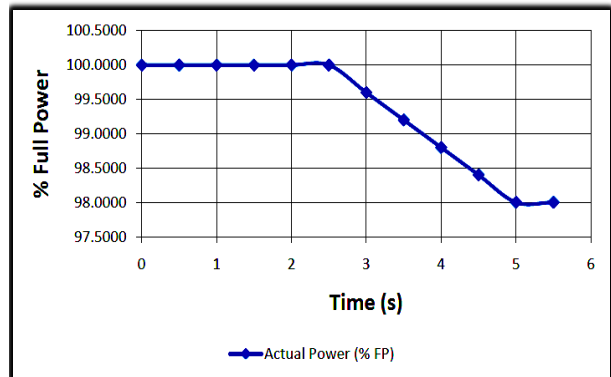


Fig. 20. Reactor Power Ramp-down Transient ACR700 RRS

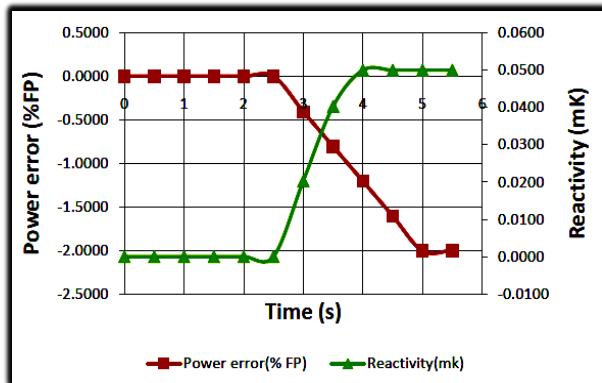


Fig. 21. Prediction of Power Error and Reactivity in Power Ramp-down Transient of ACR700 RRS

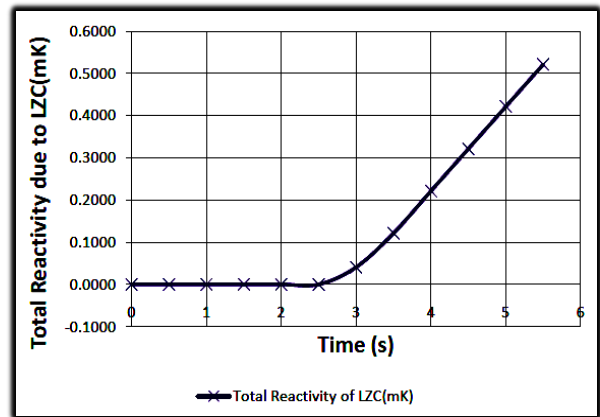


Fig. 22. Prediction of Total Reactivity of Liquid Zone Control System in Power Ramp-down Transient of ACR700 RRS

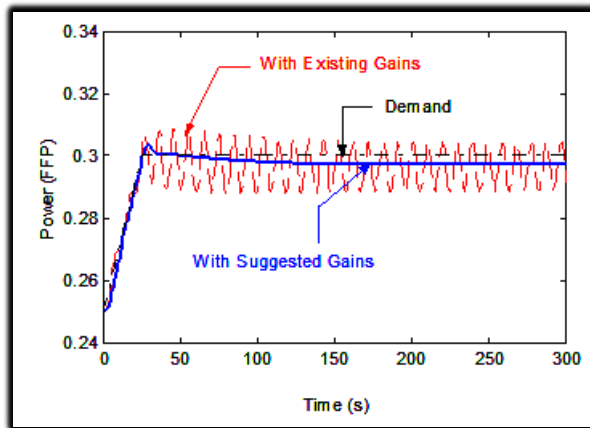


Fig. 23. Performance Comparison of Reactor Power under Low Power Transient for ACR700 RRS

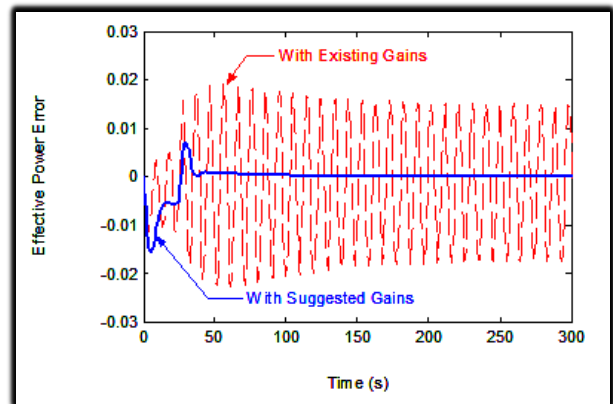


Fig. 24. Performance Comparison of Effective Reactor Power Error under Low Power Transient for ACR700 RRS

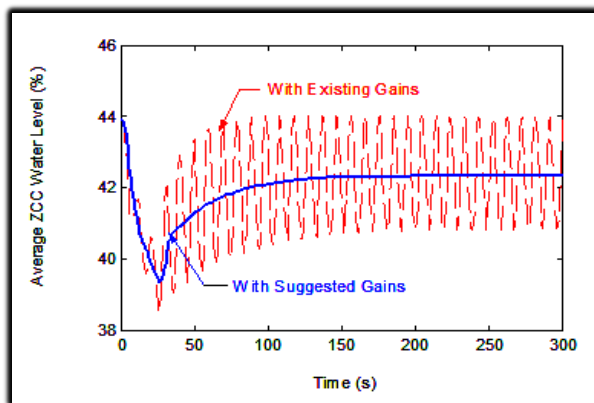


Fig. 25. Performance Comparison of Average Zone Control Compartment Water Level under Low Power Transient for ACR700 RRS

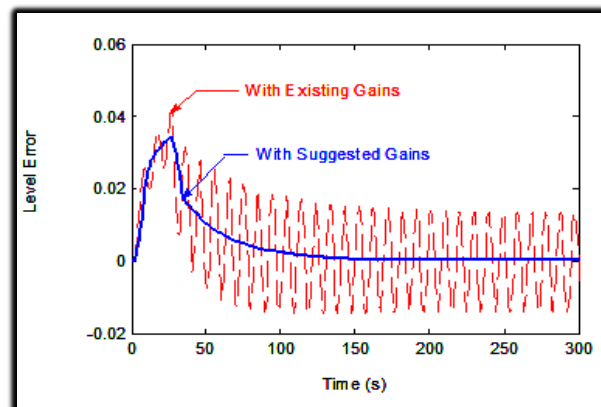


Fig. 26. Performance Comparison of Zone Control Compartment Water Level Error under Low Power Transient for ACR700 RRS

One PID controller as existing controller while other as ANFIS controller are configured with RRS model. Parameters or gains of the controllers are optimized in LabVIEW environment. A hybrid framework is designed and developed integrating VB and LabVIEW. As a result of this research work a sophisticated toolkit is developed called VBLAB. The performance of the suggested new ACR-700 RRS controller is compared existing controller and found faster, robust and within the designed control bands.

5. ACKNOWLEDGEMENT

The support of the Pakistan Atomic Energy Commission, Chashma Centre of Nuclear Training and Information Support Division of KNPGRS is gratefully acknowledged.

6. CONFLICT OF INTEREST

The authors declare no conflict of interest.

7. REFERENCES

1. M. Johnson, S. Lucas, and P. Tsvetkov. Modeling of reactor kinetics and dynamics. *Idaho National Laboratory, Report Idaho Falls, Idaho 83415, U.S. Department of Energy, Canada* (2010).
2. W.K. Lam. Advanced pressurized water reactor simulator. *IAEA Workshop on NPP Simulators for Education, Bucharest, Romania* (2006).
3. A.S. Mollah. Education tool for simulation of safety and transient analysis of a pressurized water reactor. *International Journal of Integrated Sciences & Technology* 03: 01-10 (2018).
4. S.U.E. Hakim, A. Abimanyu, and Sutanto. Simulator design of Kartini reactor based on LabVIEW. *Journal forum Nukir* 12: 29-41 (2018).
5. A.H. Malik, A. A. Memon, and F. Arshad. Advanced multi-modeling of PWR dynamics and deep learning based computational tool in SIMULINK and LabVIEW. *Proceedings of Pakistan Academy of Sciences-A: Physical and Computational Sciences* 59: 71-81 (2022).
6. S.M.H. Mousakazemi. Control of a pressurized light-water nuclear reactor two-point kinetics model with performance index-oriented PSO. *Nuclear Engineering and Technology* 53: 2556-2563 (2021).
7. H.S. Shim, and J.C. Jung. Improved RRS logical architecture using genetic algorithm. *Nuclear Engineering and Technology* 49: 1696-1710 (2017).
8. C.H. Cho, J.H. Choi, J.Y. Hoi, and S.Y. Lee. CANDU NPP reactor regulating system modeling using CATHENA. *Annulus of Nuclear Energy* 23: 909-918 (1996).
9. G. Boroni, and A. Clause. Ladwig: A training simulator of the safety operation of a CANDU. *Science and Technology of Nuclear Installations: 1-8* (2011).
10. C.S. Subudhi, T.U. Bhatt, and A.P. Tiwari. A mathematical model for total power control loop of large PHWRs. *IEEE Transactions on Nuclear Science* 46: 1901-1911 (2016).
11. V.S. Volodin, and A.O. Tolokonskii. Parameters settings of NPP automatic regulators via analytical simulators. *XIII International Youth Scientific and Practical Conference* 317-326 (2017).
12. A.P. Tiwari, T.U. Bhatt, and P.V. Surjagade. Modelling and spatial control of 540 MWe pressurized heavy water reactor. *Transactions on Indian National Academy of Engineering* 06: 731-753 (2021).
13. S. Banerjee, D. Bose, A. Hazra, S. Chattopadhyay, and K. Ghosh. Controller design for operation of a 700 MWe PHWR with limited voiding. *Nuclear Engineering and Design* 357: 1-12 (2020).
14. M.C. Darling, G.F. Luger, T.B. Jonesy, M.R. Denman, and K.M. Groth. Intelligent modeling for nuclear power plant accident management. *International Journal on Artificial Intelligence Tools* 27: 1-25 (2018).
15. A.H. Malik, A.A. Memon, and F. Arshad. Fractional order modelling and robust multi-model intelligent controllers' synthesis for ACP1000 nuclear power plant. *Mehran University Research Journal of Engineering and Technology* 41: 43-53 (2022).
16. M.F. Shidik, and R.S.N. Mahmudah. Safety analysis of advanced CANDU reactor-700 (ACR-700) during transient and emergency condition using ACR simulator. *Journal of Sains Dasar* 10: 30-35 (2021).



Analysis of Stochastic Patterns of Daily Minimum Extreme Temperature of Karachi in Global Climate Change Perspective

Muhammad Atif Idrees^{*1}, Syed Ahmed Hassan², and Muhammad Arif Hussain¹

¹Department of Basic Sciences, DHA SUFFA University, Karachi, Pakistan

²Department of Mathematics, University of Karachi, Karachi, Pakistan

Abstract: Effects of climate change are a critical and globally accepted phenomenon and gradually becoming inevitable and catching the attention of policymakers around the world. Temperature is a principal climatic factor and is defined as the degree or intensity of heat causing huge consequences on human beings' lives. This paper suggests some stochastic approaches to do an analysis of the Karachi region's daily minimum extreme temperature from Jan 1, 2010, to Dec 31, 2014. It is observed that the average daily minimum temperature fits the Markov chain and its limiting probability has reached steady-state conditions after 20 to 87 steps or transitions. The results indicate that after 20 to 87 days the distribution becomes stationary. The smaller steady-state time represents the stationarity of the data series, whereas long-term behavior shows non-stationarity in trend behavior in the respective seasonal time series. Furthermore, the overall annual dormancy of 24 °C to 31 °C daily minimum temperature was analyzed early part of the summer season. This study can be useful for weather variability forecasting.

Keywords: Temperature, Markov Chain, Transition Probability Matrix, Karachi.

1. INTRODUCTION

Climatologists have studied a drastic change in temperature that has been a cause for concern for many years. The consequences of climate change are becoming more and more inevitable and are drawing the attention of policymakers around the world. Several studies have shown links between high temperatures and other extreme weather conditions like urban heat in Iceland, unexpected variations in the urban humidity index, heatstroke, sea level rise, etc., which may cause many casualties and even deaths. Idrees and Hira analyzed that the steady rise in annual temperature is often related to a significant increase in the local heat index (energy). Moreover, being the world's seventh-largest (total area of 3,527 km²) and most crowded city in Pakistan, situated on the shores of the Arabian Sea, Karachi has recently (2015) faced thousands of deaths due to high temperatures/heat stroke. Most of the deaths were in densely populated areas of Karachi, possibly due to the

effects of the urban heat island effect [1]. Usually, Karachi's weather is overall quite pleasant and its climate tends to be moderate due to marine impact. However, instead of four seasonal types, it has typically six seasonal kinds, Winter (Mid Dec. - Feb.), Spring (March - Mid April), First Summer (Mid-April - May), Monsoon (June - Mid Sep.), Second Summer (Mid Sep. - Oct.), Autumn (Nov. - Mid Dec.) (Table 1).

Climate events predictions are a fascinating research topic that meteorologists have been paying attention to for a long time. Tawfeek *et al.* [2], Daren *et al.* [3], Mustafa *et al.* [4] used multiple models to see the expected changes in the future. Squintu *et al.* [5] and Sillmann *et al.* [6] concluded that the climate model is the main resource of climate analysis, it can reconstruct the current environment and the unpredictability of current climate conditions and represent future climate scenarios.

Christidis *et al.* [7] suggested that the people

need to understand the weather conditions in the next few days and other times in the future. Since the weather is such an important part of people's lives, they need to understand whether there is a pattern that determines when these events occur and how serious they may be. Climate change put some burdens on arranging some regular alterations in people's lifestyles and planning at the national level, for example, special preparations for regular outings to work or school and make economic developments of energy resources.

Turner *et al.* [8], You *et al.* [9], Stone *et al.* [10], and Dasari *et al.* [11] suggested that when analyzing climate activities under different conditions of selected Antarctic stations, the researchers proposed various linear trend models of sea surface temperature, showing most of these had warmed patterns and some had cooling patterns. Shumway *et al.* [12], Hassan *et al.* [13], and Khan *et al.* [14] concluded that in a couple of years, a variety of time-series studies have been undertaken to determine the essence of climate change in various regions of the world. The analysis of the time series is to offer future predictions by modeling the past data. The Autoregressive Integrated Moving Average (ARIMA) model is the most widely used time series method in the study of hydro-climatology variability and many real world applications. Ching *et al.* [15], Ching *et al.* [16], and Liu *et al.* [17] suggested that a good and precise time series model and forecasts indicate better efficiency and effectiveness and may be helpful in optimal planning and decision-making process. Chu *et al.* [18] concluded that the prediction of time series using the Markov chain method results in better efficiency and effectiveness. The selection of models under the strong impact of the monsoon and complex climate conditions is a big challenge.

Buzacott *et al.* [19] analyzed that the Markov chains are also a helpful tool in modeling numerous practical frameworks, for example, queuing theory, fabricating, and stock market frameworks. The Markov chain method demonstrating all out-information arrangements can be likewise found. Bartholomew *et al.* [20] introduced the basic principles of Markov Chains. Feller *et al.* [21], Kemeny *et al.* [22] leading mathematicians who incorporated A. Kolmogorov theory and further established the theory. However, it was not until the 1960s that economics, social sciences, and most other applied sciences realized the importance of this theory. Ching *et al.* [23] suggested that Some of the issues with Markov chain implementations can be overcome by distinguishing between two chain shapes, Ergodic and Absorbent.

Markov chain are valuable tools for modeling a range of functional processes, such as queuing structures, production processes and distribution systems. Categorical data sequence modeling applications of Markov chains can also be found. This paper employs the Markov chain method to analyze the seasonal daily minimum temperature of the Karachi region. These results suggest that in spring and fall (each of the 3-month period) seasons the temperature values are almost unstable and the steady-state conditions arrived after 86 and 87 transitions respectively. Furthermore, the annual dominancy of hot to very hot (24 to 31 °C) temperature during March to August followed by Cold to Normal (10 to 18 °C) weather in September to February months.

2. METHODOLOGY

The five years data of daily minimum temperature from Jan 1, 2010, to Dec 31, 2014, of Karachi

Table 1. The weather/climatic of Karachi categories in six different statuses.

Season (Time)	Minimum Temperature	Maximum Temperature	Weather/Climatic Status
Winter (mid Dec. to Feb.)	10	24	Cold
Spring (Mar. to mid Apr.)	22	35	Humid
First Summer (mid Apr. to May)	30	40	Hottest weather
Monsoon (Jun. to mid Sep.)	26	33	Drizzle, Rainy and Humid
Second Summer (mid Sep. to Oct.)	23.65	34.4	Clear cloud, suddenly hot, some heat waves
Autumn (Nov. to mid Dec.)	12.8	31.8	Cool nights and Hottest days

airport was collected from Pakistan Meteorological Department. This data is divided into four seasonal pairings of three months, winter, spring, and summer from December to February, March to May, June to August and September to November respectively. The Markov chain is being applied using MATLAB software for Karachi city air temperature.

$$P = \begin{pmatrix} p_{01} & p_{02} & p_{03} & \dots \\ p_{11} & p_{12} & p_{13} & \dots \\ p_{21} & p_{22} & p_{23} & \dots \\ \vdots & \vdots & \vdots & \dots \end{pmatrix}$$

is called the Markov chain transition matrix, or transition probability matrix $\{X_n, n=0,1,2,\dots\}$.

2.1 Markov Chain

Stochastic processes, denoted by $\{X_n | n \in I\}$ for a finite or countable index set I, or $\{X(t) | t \in T\}$ for an uncountable index set T, refer to sets of random variables. Simply put, a stochastic process is a mathematical model that evolves probabilistically over a certain period of time [24]. The concept of the Markov Chain, which was introduced by Andrey Andreyevich-Markov in 1907, is a new form of a stochastic process. This process explains how the outcome of a particular experiment may impact the outcome of the subsequent experiment [25].

A stochastic process $\{X_n | n=0,1,2,\dots\}$ is said to be a Markov chain with a finite or countlessly infinite state space, if for $i,j,i_0,\dots,i_{n-1} \in S$, and $n=0,1,2,\dots$

$$P(X_{n+1} = j | X_n = i, X_{n-1} = i_{n-1}, \dots, X_0 = i_0) = P(X_{n+1} = j | X_n = i) = P_{ij}$$

Given a collection of states, $S=\{i,j,i_0,\dots,i_{n-1}\}$, $n=0,1,2,\dots$ the process starts from one of the three states and moves successively from one state to another, and each movement is called a phase. If the chain is in state i at the moment, then it moves to another state j with a transitional probability denoted as p_{ij} and that probability is independent of the previous state [21].

The p_{ij} , is also called probabilities of transformation, the process can stay in the state i with probability p_{ii} . An initial probability distribution, defined in S , specifies the starting state and matrix, P ,

where each $0 \leq P_{ij} \leq 1$ and $\sum_{j=0}^{\infty} p_{ij} = 1, \dots i = 0,1,2,\dots$

3. RESULTS AND DISCUSSION

Fig. 1 represents the daily minimum temperature for four seasonal time series plots from 2010-to-2014 from December to February (DJF), March to May (MAM), June to August (JJA), and September to November (SON) of Karachi Airport. The temperature from all three seasons except JJA show overall stationary behavior, however, during 2013 and 2014 they show some rising trend (within 3 months not observed in previous years). This behavior puts some non-stationarity in the data series, which may be due to some local and most probably global impact. The JJA temperature shows the overall stationary behavior. Table 2 shows the transition states temperature ranges of all four selected seasons of the minimum temperature in Karachi city.

The Markov analysis of the seasonal temperature from DJF is analyzed considering three initial transition states defined as, very cold ($5 \leq t < 10$), cold ($10 \leq t < 15$) and normal ($15 \leq t < 21$). The associated DJF estimated Markov transition probability matrix is defined as P_1 :

The probabilities of the above P_1 matrix show that if the minimum temperature is initially in the very cold range, then the probabilities for the next day will be very cold, cold, and normal with 77 %, 23 %, and 0 % respectively. Moreover, if the minimum temperature is initially cold, then the probabilities for the next day will be very cold, cold,

Table 2. Relate the steady-state probability of all four seasons' daily minimum temperature

Winter: DJF (Range 16°C) (P_1^{28})		Spring: MAM (Range 21°C) (P_2^{86})			Summer: JJA (Range 9°C) (P_3^{20})		Fall: SON (Range 21°C) (P_4^{87})				
Very Cold 5-10°C	Cold 10-15°C	Normal 15-21°C	Cold 10-18°C	Normal 18-24°C	Hot 24-31°C	Warm 22-25°C	Hot 25-27°C	Very Hot 27-31°C	Very Hot 24-31°C	Hot 18-24°C	Normal 10-18°C
0.35	0.50	0.15	0.15	0.35	0.50	0.02	0.16	0.82	0.25	0.35	0.40

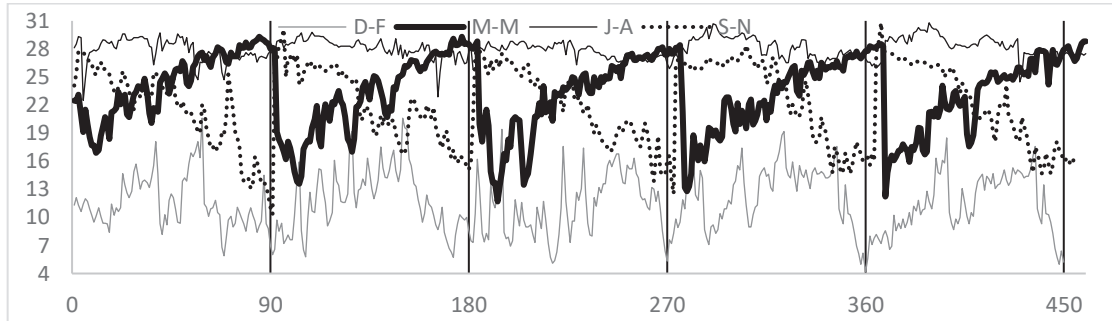


Fig. 1. Daily mean minimum temperature from 2010-to-2014 during December to February (DJF, Lower graph), March to May (MAM), June to August (JJA, Upper graph) and September to November (SON) of Karachi Airport.

		very cold	cold	normal		very cold	cold	normal		very cold	cold	normal					
$P_1 =$	<table border="1"> <tr><td>very cold</td></tr> <tr><td>cold</td></tr> <tr><td>normal</td></tr> </table>	very cold	cold	normal	0.77	0.23	0.00	;	$P_1^2 =$	0.63	0.34	0.03	;	$P_1^{28} =$	0.35	0.50	0.15
		very cold															
		cold															
normal																	
0.15	0.71	0.14	0.23	0.60	0.17	0.35	0.50	0.15									
0.03	0.43	0.54	0.10	0.54	0.35	0.35	0.50	0.15									

and normal with 15 %, 71 %, and 14 % respectively. Finally, if the minimum temperature is initially normal, then the probabilities for the next day will be very cold, cold, and normal with 3 %, 43 %, and 54 % respectively. Fig. 2 represents a transition diagram describing the state transition probabilities with nodes very cold, cold, and normal in the daily minimum temperature of DJF.

After two transitions or multiplying P_1 by itself, P_1 will be P_1^2 matrix as shown above. It is shown that if the temperature is initially very cold, then the probability that temperature for the day after tomorrow will be very cold, cold and normal with 63 %, 34 % and 3 % respectively. Similarly, other state transition probabilities have been interpreted. After 28 transitions periods (28th-time multiplication of P_1), this matrix indicates that the Markov chain has reached its steady state or limit probabilities, as shown in the P_1^{28} matrix defined above. This result has shown that in the future, the

transition probabilities become stationary which means it will be very cold, cold and normal after 28 days of transition and so on are 35 %, 50 % and 15 % respectively. Therefore, there is no impact between current day temperatures with after 28 days temperature. This shows that in the future the chances of temperature change during the month DJF after 87 days/transitions will be very cold, cold and normal are varying from 77 %, 15 % and 0.03 to 35%, very cold; 23 %, 71 % and 43 % to 50 % cold; and 0 %, 14 % and 54 % to 15 % normal respectively.

Similarly, the temperature from MAM is analyzed, with initial states defined as, Cold ($10 \leq t < 18$), Normal ($18 \leq t < 24$), and Hot ($24 \leq t < 31$). The respective MAM estimated transition probability matrix is defined as P_2 :

The probabilities of the above P_2 matrix show that if the minimum temperature is initially

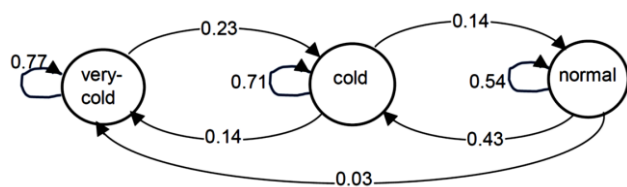


Fig. 2. Transition diagram of December to February (DJF)

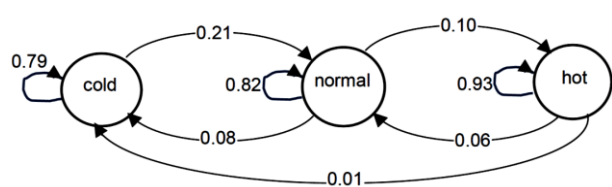


Fig. 3. Transition diagram of March to May (MAM)

$$P_2 = \begin{matrix} & \begin{matrix} \text{cold} & \text{normal} & \text{hot} \end{matrix} \\ \begin{matrix} \text{cold} \\ \text{normal} \\ \text{hot} \end{matrix} & \begin{bmatrix} 0.79 & 0.21 & 0.00 \\ 0.08 & 0.82 & 0.10 \\ 0.01 & 0.06 & 0.93 \end{bmatrix} \end{matrix} ; P_2^2 = \begin{matrix} & \begin{matrix} \text{cold} & \text{normal} & \text{hot} \end{matrix} \\ \begin{matrix} \text{cold} \\ \text{normal} \\ \text{hot} \end{matrix} & \begin{bmatrix} 0.64 & 0.34 & 0.02 \\ 0.13 & 0.70 & 0.17 \\ 0.02 & 0.11 & 0.87 \end{bmatrix} \end{matrix} ; P_2^{86} = \begin{matrix} & \begin{matrix} \text{cold} & \text{normal} & \text{hot} \end{matrix} \\ \begin{matrix} \text{cold} \\ \text{normal} \\ \text{hot} \end{matrix} & \begin{bmatrix} 0.15 & 0.35 & 0.50 \\ 0.15 & 0.35 & 0.50 \\ 0.15 & 0.35 & 0.50 \end{bmatrix} \end{matrix}$$

in the cold range, then the probabilities for the next day will be cold, normal, and hot with 79 %, 21 %, and 0 % respectively. Moreover, if the minimum temperature is initially normal, then the probabilities for the next day will be cold, normal, and hot with 8 %, 82 %, and 10 % respectively. Finally, if the minimum temperature is initially hot, then the probabilities for the next day will be cold, normal, and hot with 0 %, 6 % and 93 % respectively. Fig. 3 represents a transition diagram describing the state transition probabilities with nodes cold, normal, and hot in the daily minimum temperature of MAM. When multiplying P_1 by itself or after two transitions, the probability matrix will now be equal to P_2^2 as defined above. It is shown that if the temperature is initially cold, then the probability that the temperature for the day after tomorrow will be cold, normal, and hot with 64 %, 34 %, and 2 % respectively. Similarly, the other state probabilities have been interpreted. After 86 transitions period, the P_2 matrix attained the steady-state or limiting

probability matrix as shown above as P_2^{86} .

Results have shown that in the future, the transition probabilities become stationary, which implies that it will be cold, normal, and hot after 86 days/transition and so on are 15 %, 35 %, and 50 % respectively. So, there is no impact between the current day temperature with after 86 days' temperature. In the cluster, MAM the probabilities that the minimum temperature after 86 days/transitions will be cold, normal and hot vary from 79 %, 8 % and 1 % to 15 % cold; 21 %, 82 % and 6% to 35 % normal and 0 %, 10 % and 93 % to 50 % hot respectively.

Like the above seasonal behavior, the temperature values from JJA are analyzed, with initial states defined as, warm ($22 \leq t < 25$), hot ($25 \leq t < 27$), and very hot ($27 \leq t < 31$). Their estimated Markov transition probability matrix, is P_3 define as:

$$P_3 = \begin{matrix} & \begin{matrix} \text{warm} & \text{hot} & \text{very hot} \end{matrix} \\ \begin{matrix} \text{warm} \\ \text{hot} \\ \text{very hot} \end{matrix} & \begin{bmatrix} 0.14 & 0.86 & 0.00 \\ 0.04 & 0.55 & 0.41 \\ 0.01 & 0.07 & 0.92 \end{bmatrix} \end{matrix} ; P_3^2 = \begin{matrix} & \begin{matrix} \text{warm} & \text{hot} & \text{very hot} \end{matrix} \\ \begin{matrix} \text{warm} \\ \text{hot} \\ \text{very hot} \end{matrix} & \begin{bmatrix} 0.06 & 0.59 & 0.35 \\ 0.03 & 0.37 & 0.60 \\ 0.01 & 0.11 & 0.88 \end{bmatrix} \end{matrix} ; P_3^{20} = \begin{matrix} & \begin{matrix} \text{warm} & \text{hot} & \text{very hot} \end{matrix} \\ \begin{matrix} \text{warm} \\ \text{hot} \\ \text{very hot} \end{matrix} & \begin{bmatrix} 0.02 & 0.16 & 0.82 \\ 0.02 & 0.16 & 0.82 \\ 0.02 & 0.16 & 0.82 \end{bmatrix} \end{matrix}$$

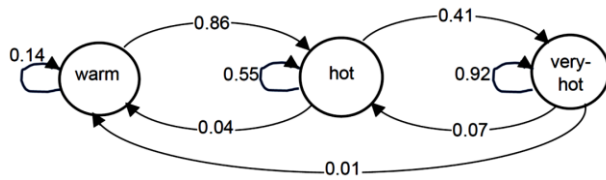


Fig. 4. Transition diagram of June to August (JJA)

It implies that from the above matrix if the minimum temperature is initially in the warm range, then the probabilities for tomorrow will be warm, hot, and very hot with 14%, 86%, and 0% respectively. Moreover, if the temperature is

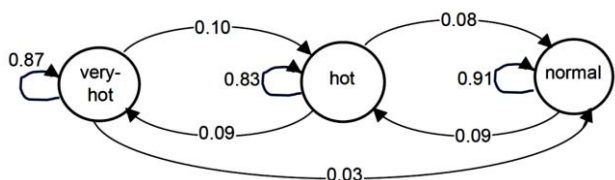


Fig. 5. Transition diagram of Sep. to Nov. (SON)

initially in the hot range, then the probabilities for tomorrow will be warm, hot, and very hot with 4%, 55%, and 41% respectively. Finally, if the temperature is initially in the very hot range, then the probabilities for tomorrow will be warm, hot,

$$P_4 = \begin{array}{c|ccc} & \text{very hot} & \text{hot} & \text{normal} \\ \hline \text{very hot} & 0.87 & 0.10 & 0.03 \\ \text{hot} & 0.09 & 0.83 & 0.08 \\ \text{Normal} & 0.00 & 0.09 & 0.91 \end{array} ; P_4^2 = \begin{array}{c|ccc} & \text{very hot} & \text{hot} & \text{normal} \\ \hline \text{very hot} & 0.77 & 0.17 & 0.06 \\ \text{hot} & 0.15 & 0.71 & 0.14 \\ \text{Normal} & 0.01 & 0.16 & 0.83 \end{array} ; P_4^{87} = \begin{array}{c|ccc} & \text{very hot} & \text{hot} & \text{normal} \\ \hline \text{very hot} & 0.25 & 0.35 & 0.40 \\ \text{hot} & 0.25 & 0.35 & 0.40 \\ \text{Normal} & 0.25 & 0.35 & 0.40 \end{array}$$

and very hot with 1 %, 7 %, and 92 % respectively. Fig. 4 shows the transition diagram indicating the state transition probabilities with nodes warm, hot, and very hot in the daily temperature respectively.

After two transitions or multiplying P_3 itself, the matrix will now be P_3^2 as shown above. The first row of P_3^2 matrix indicates that if the temperature is initially in the warm range, then the probabilities that the temperature for the day after tomorrow of warm, hot, or very hot will be 6 %, 59 % and 35 % respectively. In the same way, for other state probabilities are interpreted. After 20 transitions, the P_3 according to the matrix, the Markov chain has either achieved its steady-state or reached the limit probabilities as illustrated in P_3^{20} matrix define above.

The P_3^{20} transition matrix has shown that in the future, the transition probabilities will become stationary which implies it will be warm, hot and very hot after 20 days or transition and so on are 2 %, 16 % and 82 % respectively. So, there is no impact between current day temperature with after 23 days temperature. For the JJA probabilities that the minimum temperature after 20 days/transitions will be warm, hot and very hot are varied from 14 %, 4 % and 1 % to 2 % warm; 86 %, 55 % and 7 % to 16 % hot and 0 %, 41 % and 92 % to 82 % very hot respectively.

Now, the temperature from SON is analyzed, with initial states defined as, very hot ($24 \leq t < 31$), hot ($18 \leq t < 24$), and normal ($10 \leq t < 18$). The estimated transition matrix, P_4 of the temperature is defined as P_4 :

The transition probabilities of the P_4 matrix (first row) show that, if the temperature is initially in the very hot range, then the next day probabilities for very hot, hot, or normal states are 87 %, 10 %, and 3 % respectively. Moreover, if the state is initially hot, then the next day's temperature probabilities

will be very hot, hot, and normal with 9%, 83% and 8 % chance respectively. Finally, if the state is initially at normal, then the next day probabilities will be of very hot, hot, and normal with 0 %, 9 % and 91 % chance respectively. Fig. 5 shows the transition diagram indicating the state transition probabilities with nodes very hot, hot, and normal in the daily temperature respectively.

After two transitions or multiplying P_4 itself, the probabilities will be represented as P_4^2 matrix define above. This matrix shows that if the temperature is initially at a very hot state, then the probabilities that the temperature for the day after tomorrow will be very hot, hot, and normal states with 77 %, 17 % and 6 % chance respectively. In the same way we can consider probabilities for other states. After 87 transitions, the steady-state or limit probabilities of the Markov chain are indicated in the matrix P_4^{87} , suggesting that the Markov chain has either reached its steady-state or attained the limit probabilities. These results have shown that the transition probabilities become stationary in the future. The transition from any state to very hot and hot ranges after 87 days of transition are 25 %, 35 % and 40 % respectively. So, there is no change in the transition probability after 87 days temperature from one initial state to another. This shows that, for SON the probabilities that the minimum temperature after 87 days/transitions will be very hot, hot and normal are varied from 87 %, 9 % and 0 % to 25 % very hot, 10 %, 83 % and 9 % to 35 % hot and 3 %, 8 % and 91 % to 40 % normal respectively.

The temperature ranges of four seasons, winter (16 °C), spring (21 °C), summer (9 °C), fall (21 °C) have a transitional period to steady the state probabilities, (P_1^{23} , P_2^{86} , P_3^{20} and P_4^{87}) are about 23, 86, 20, and 87 days respectively (Table-2). This relation shows that range of the temperature may be directly related to the steady state period. Moreover, the steady state period of 86 and 87 days/transitions may suggest that in spring (92 days) and

fall season's (91 days) the temperatures are almost unstable, respectively. The steady state matrices (P_1^{23} , P_2^{86} , P_3^{20} and P_4^{87}) and Table 2 depicted that the over annual dominance of temperature 24 to 31 °C (Hot to very hot) from March to August followed by 10 to 18 °C (Cold to Normal) from September to February periods. The formation of P_1 , P_2 , P_3 , and P_4 and related steady state matrices suggested that climate change analyses (for a different span of time) may be utilized Markov transition probability method.

4. CONCLUSION

The time series graph mentioned some climate change indications as an abrupt shift in the mean of the three seasonal data except JJA during the years 2013 and 2014. In order to predict the future temperature, parameters such as atmospheric temperature, humidity, and precipitation are required, moreover, the transition probability matrix will be a good choice for future temperature determination. This paper analyzed the daily minimum temperature data of Karachi Airport to predict their overall future behavior, according to the Markov chain model. The temperature long-term behavior described that after 20 to 87 days/transitions no impact of temperature appears in changing the probabilities from one state to another. The short steady-state interval of 23 of DJF and 20 days of JJA shows that both seasons have stationary data series. The long steady-state interval of 86 MAM and 87 days of SON represents a trend and nonstationary behavior. The steady-state transitional periods may be directly related to the temperature range and their nonstationary and trend behavior of the season. The smaller steady-state time represents the stationary of the data series, whereas, the long time shows nonstationary and trend behavior in respective seasonal time series. The annual dominance of daily minimum temperature is from 24 to 31 °C (Hot to very hot) from March to August and particularly 24 to 31 °C for JJA season. Conclusively, the Markov chain analysis may be a good method to reconstruct the current environment and the unpredictability of the current climate conditions and represent future climate scenarios. This study may prove useful in analyzing weather condition variability. It is recommended that additional data be included to facilitate a more extensive analysis.

5. ACKNOWLEDGMENTS

The authors are thankful to Dr. Zaheer Uddin (Department of Physics, University of Karachi) for guidance and fruitful discussions. The authors are also thankful to Pakistan Metrological Department for providing data for this study.

6. CONFLICT OF INTEREST

The authors declare no conflict of interest.

7. REFERENCES

1. M.A. Idrees, and H.A. Baig. Simulation and Modelling of Maximum and Minimum Temperature of Karachi. *Journal of Natural Sciences Research* 8: 19 (2018).
2. Y.Q. Tawfeek, F.H. Jasim, and M.H. Al-Jiboori. A Study of Canopy Urban Heat Island of Baghdad, Iraq. *Asian Journal of Atmospheric Environment* 14: (2020).
3. R.H. Daren, C.W. Richardson, C.L. Hanson, and G.L. Johnson. Simulating maximum and minimum daily temperature with the normal distribution. *ASAE Annual Meeting, American Society of Agricultural and Biological Engineers* (1998).
4. E.K. Mustafa, Y. Co, G. Liu, M.R. Kaloop, A.A. Beshr, F. Zaraoura, and M. Sadek. Study for Predicting Land Surface Temperature (LST) Using Landsat Data: A Comparison of Four Algorithms. *Advances in Civil Engineering* 2020: 16 (2020).
5. A.A. Squintu, G. Schrier, E. Besselaar, E. Linden, D. Putrasahan, C. Roberts, M. Roberts, E. Scoccimarro, R. Senan, and A.K. Tank. Evaluation of trends in extreme temperatures simulated by HighResMIP models across Europe. *Climate Dynamics* 56: 2389–2412 (2020).
6. J. Sillmann, M.G. Donat, J.C. Fyfe, and F.W. Zwiers. Observed and simulated temperature extremes during the recent warming hiatus. *Environmental Research Letters* 9 (2014).
7. N. Christidis, P.A. Stott, and S.J. Brown. The Role of Human Activity in the Recent Warming of Extremely Warm Daytime Temperatures. *Journal of Climate* 24: 1922-1930 (2011).
8. J. Turner, J.C. King, T.A. Lachlan-Cope, and P.D. Jones. Recent temperature trends in the Antarctic. *Nature* 418: 291-292 (2002).
9. P. You, and A. Jézéquel, Simulation of extreme heat waves with empirical importance sampling.

- Geoscientific Model Development* 13: 763–781 (2020).
10. A.D. Stone, and A.J. Weaver. Daily maximum and minimum temperature trends in a climate model. *Geophysical Research Letters* 29: 70-1 (2002).
 11. H. P. Dasari, S. Rui, J. Perdigao, and V.S. Challa. A regional climate simulation study using WRF-ARW model over Europe and evaluation for extreme temperature weather events. *International Journal of Atmospheric Sciences* 2014: 704079 (2014).
 12. H.R. Shumway, and S.D. Stoffer. ARIMA models. *Time series analysis and its applications* 75-163 (2017).
 13. S.A. Hassan, and M.R.K. Ansari. Nonlinear analysis of seasonality and stochasticity of the Indus River. *Hydrological Sciences Journal–Journal des Sciences Hydrologiques* 55: 250-265 (2010).
 14. H. Khan, and S.A. Hassan. Stochastic River Flow Modelling and Forecasting of Upper Indus Basin. *Journal of Basic and Applied Sciences* 11: 630-636 (2015).
 15. W.K. Ching, S.F. Eric, and K.N. Michael. Higher-order Markov chain models for categorical data sequences. *Naval Research Logistics (NRL)* 51: 557-574 (2004).
 16. W.K. Ching, K.N. Michael, and E.S. Fung Higher-order multivariate Markov chains and their applications. *Linear Algebra and its Applications* 428: 492-507 (2008).
 17. T. Liu. Application of Markov chains to analyze and predict the time series. *Modern Applied Science* 4: 162 (2010).
 18. J. T. Chu, J. Xia, C-Y. Xu, and V. P. Singh Statistical downscaling of daily mean temperature, pan evaporation and precipitation for climate change scenarios in Haihe River, China. *Theoretical and Applied Climatology* 99: 149-161 (2010).
 19. J. A. Buzacott, and J. G. Shanthikumar. Stochastic models of manufacturing systems. Pearson (1993).
 20. D.J. Bartholomew. Recent developments in nonlinear stochastic modelling of social processes. *Canadian Journal of Statistics* 12: 39-52 (1984).
 21. W. Feller 2008. An introduction to probability theory and its applications. *John Wiley & Sons* 2: 704 (1991).
 22. J.G. Kemeny, and J.L. Snell. Mathematical Models in the Social Sciences. *Introduction to Higher Mathematics*. New York, Toronto, London, Blaisdell Publishing Company, A Division of Ginn and Company 145 (1963).
 23. W.K. Ching. Iterative methods for queuing and manufacturing systems. *Springer Science & Business Media* (2001).
 24. A. Berger. Linear Algebra Application~ Markov Chains. *Mathematics* (2007).
 25. W.T. Anderson, and A.G. Leo. Statistical inference about Markov chains. *The Annals of Mathematical Statistics* 89-110 (1957).



Tidal Range Energy Resource Estimation of Khor Kalamat using Geostatistical Modeling

Ambreen Insaf¹, Mirza Salman Baig^{1*}, Saba Javaid², Umair Abbas³, and Zaheer Uddin⁴

¹Department of Applied Physics, University of Karachi, Karachi, Pakistan

²Department of Physics, Federal Urdu University of Arts Science and Technology, Karachi, Pakistan

³Institute of Space Science and Technology, University of Karachi, Karachi, Pakistan

⁴Department of Physics, University of Karachi, Karachi, Pakistan

Abstract: Electrical power generation by tidal energy provides various advantages. The energy is highly predictable, has less impact on ecological pollution and provides an indefinite amount of renewable energy. The countries like Canada, China, Russia, South Korea and France are extensively utilizing tidal sources of energy for the generation of electrical energy. A suitable site (where less construction is required), adequate tidal range and sufficient bathymetry; are the basic requirements for the installation of a tidal power plant however sometimes there is no tidal data available for suitable sites, like Khor Kalamat tidal lagoon in Pakistan. Therefore, this study is conducted to assess the tidal energy resources of the naturally blessed lagoon, Khor Kalamat, which is located in the Baluchistan province of Pakistan, by using geostatistical modeling. A geostatistical model is developed to estimate the tidal energy potential at Khor Kalamat by using observed data of five available locations along with the coastal belt of Pakistan. Models are designed by integrating several layers into ArcGIS. These layers include tidal data, satellite metaphors and other physical and socioeconomic layers. After processing of data, digitized models and layers are generated. Five different models have been compared and the best model is carefully chosen to predict the tidal data of Khor Kalamat after validation of the individual model. During the study, it was observed that low head hydro tidal turbine of Venturi-Enhanced Turbine Technology (VETT) is best suited for harnessing tidal energy due to adequate tidal range. Consequently, by means of a bi-directional VETT device, the output power is assessed to be 269.93 MW.

Keywords: Geostatistical Modeling, Low Head Hydro Turbine, Tidal Lagoon, Tidal Potential Power Density

1. INTRODUCTION

The oceans provide an enormous and dominant source of energy and this energy can possibly be harnessed to overcome the electricity demand globally [1]. The concept of harnessing Tidal Energy (TE) is not a recent manifestation; tidal mills are being utilized since ages. However, the energy extracted was availed for mechanical movement of devices for instance to mill the grain. Ocean water prominence takes place on the earth's side facing the moon, owing to the force of gravitation. On the other side, the centrifugal force proves the same effect in opposite direction. The highest tidal amplitude (High Water HW) can be detected on the

earth side where a new or full moon is observed and the lowest tidal amplitude (Low Water LW) can be detected on halfway. The tidal range describes the difference between the top to bottom level of water and it continues to move on because of the gyrations of the sun and the moon compared to the earth. The tidal range lies between 0.25 m till 10 m [2].

The harnessing techniques of TE are categorized into the following main technologies: Tidal range technology (barrage arrangements) and tidal current technology (marine current turbines). The fundamental tidal barrage model includes the structure of LH (Low Head) hydro turbines with

gated sluices. The operating principle describes that during the HW, the water is accumulated in the region at the back of the barrage. Subsequently, the water flows out with the ebb tide. During the period of outflow, the collected water is used to rotate the tidal turbine for electricity generation.

The Tidal Range (TR) technology is different from conservative hydropower systems for electrical generation of power, in following ways: (i) In TR, water streams in both directions mean entering and leaving the barrage [3] and (ii) electrical power generation from the technology of TR is entirely anticipated. A barrage is sited through an inlet whereas a lagoon arrangement is integrated by ridges, caissons, LH turbines, ship locks and sluices gates. A dam can be built at the entering of the channel or in the centre of land-shore and island or the central of two islands (be contingent on sites) [4]. The tidal turbines can be unidirectional or bidirectional and could be of different types such as rim turbines, tubular turbines, straflo, or bulb turbines [3, 5].

The principle of the tidal lagoon works similarly to a tidal barrage. However, it reserves some part of the water relatively instead of appearing as an entire barrier over a bay. Nonetheless, it could stay within the ocean. A major difference shows that traditional barrage structure uses a regular coastline to minimize the dimension of a barrage. However, this means, obstructing the creek or estuary, irrespective of depth. On the other hand, the lagoon has a reasonably low visual impact, for the reason that it is lower than high tide water and seems identical to a common sea partition at low water tides. Lagoons could be constructed with the help of loose combinations from wrecked arrangements and excavations. Therefore to reduce the costs of construction, any combination of economically feasible materials can be used [6].

1.1 Underdeveloped TPP (Tidal Power Plant) and Tidal Lagoon

For the successful growth of the TE industry, a comprehensive study of the scope and potential of the TE resource is necessary. In comparison with lesser mature oceanic energy technologies like marine current energy, ocean thermal energy and wave energy; tidal range technologies have a long history [7]. The numerous TPPs are under progress and various feasibility studies are considering on the estimation of tidal power resources to recommend forthcoming TPP. A summary of the same is appended in table 1. In the late 1960s, Tidal energy plants have already been commercially well-designed in Canada, China and France, and most recently in South Korea [8]. In Grevelingen lakes (Netherlands), the tidal lagoon scheme will be the first of its kind Ultra Low Head (ULH) barrage, since the tidal range will merely be in lying between 50cm to 1m. Predominantly, some UK enterprises and universities are developing LH tidal systems and also in collaboration with some smaller companies in Canada and France. At Swansea Bay (UK), a 60 MW plant is proposed with a complete resource estimation of about 60,000 MW. The visual impression of Swansea Bay lagoon will also be lower than the environmental impact of the tidal barrage. In China, a 300 MW tidal lagoon plant is also contracted for installation [8].

To encounter economic crises and overcome the upcoming challenges there is an immediate requirement for the renovation of present energy resources and to develop TPPs on the coastal belt of Pakistan. For this purpose, an estimation of uninvestigated TE resources of Khor Kalamat lagoon in Balochistan province is conducted. This study is steered primarily to evaluate the TE resources of Khor Kalamat tidal lagoon for the production of electric power.

Table 1. Studies of under-progressed TPP

S.No	Location	Estimated Output Power (MW)	Impoundment Area (km ²)	Study Conducted by
1	Canada, Minas basin-Cobequid bay	4028	130	[9]
2	UK, Severn Estuary	2000	5700	[10]
3	Australia, Kimberley	3000	-	[11]
4	India, Gulf of Kutch	50	-	[12]
5	Korea, Incheon	1320	157	[13]

2. MATERIALS AND METHODS

Pakistan has around 1000 km long shoreline having naturally sanctified bays, lagoons and creeks, however, Khor Kalmat ($25^{\circ}27'N$, $64^{\circ}05'E$) is considered an Area Of Interest (AOI) which is a lagoon situated near 320 kilometres west of Karachi in the central portion of Baluchistan and adjacent to Pasni. It is bounded by numerous small hills, which are the basis of siltation and sedimentation, for the period of irregular rains (figure 1). Khor Kalmat has a resemblance to the shape of a tree, from the view above ground, having its case signifying the appearance (which is a constricted 7 km long 2 km wide and around 20 m deep channel). It broadens sharply into a 19 km long and 27 km wide surrounded physique of water as an asymmetrical shape. The complete area is 102.25 km^2 . Mud-Flats are generally settled in the nearly perfect lagoon, which is enclosed with superficial seawater at high tides [14]. However, even being sanctified with a natural lagoon, there is no suitable data assortment or balanced intelligence to develop the existing resources of tidal energy at Khor Kalmat.

As aforementioned, since tidal data was not available in the study area, therefore, the geostatistical method is incorporated to examine the tidal range energy resources in study area primarily.

2.1 Estimation Scheme Adopted

An estimation technique has been designed and summarized, as shown in figure 2. It comprises of succeeding steps: data acquirement, data processing, modeling in GIS, endorsement of the geostatistical model, valuation of tidal data at the overlooked site, power density calculations, identification and an assortment of appropriate tidal turbine and total tidal power valuation from the tidal turbine.

Table 2. Geographical location and station IDs of sites

Station ID	Geographical Location
1	$25^{\circ}07' N 62^{\circ}19' E$
2	$25^{\circ}16' N 63^{\circ}28' E$
3	$25^{\circ} 16' 29'' N 64^{\circ} 35' 10'' E$
4	$24^{\circ} 48' N 66^{\circ} 58' E$
5	$24^{\circ}47'54.6'' N 67^{\circ}4'56.27'' E$

Instruments for acquiring tidal data comprise tidal gauges and tidal poles. Data regarding TE exploration comprises sea water levels with an hour resolution for the duration of nine years (Jan 2005-Dec 2013) for five sites. Table 2 represents data acquisition sites which are classified as Gwadar, Pasni and Ormara, along the Makran coast; and Karachi and Ghizri, along the Karachi shoreline, are considered. Time series assessments of an hour of data are organized to perceive the performance

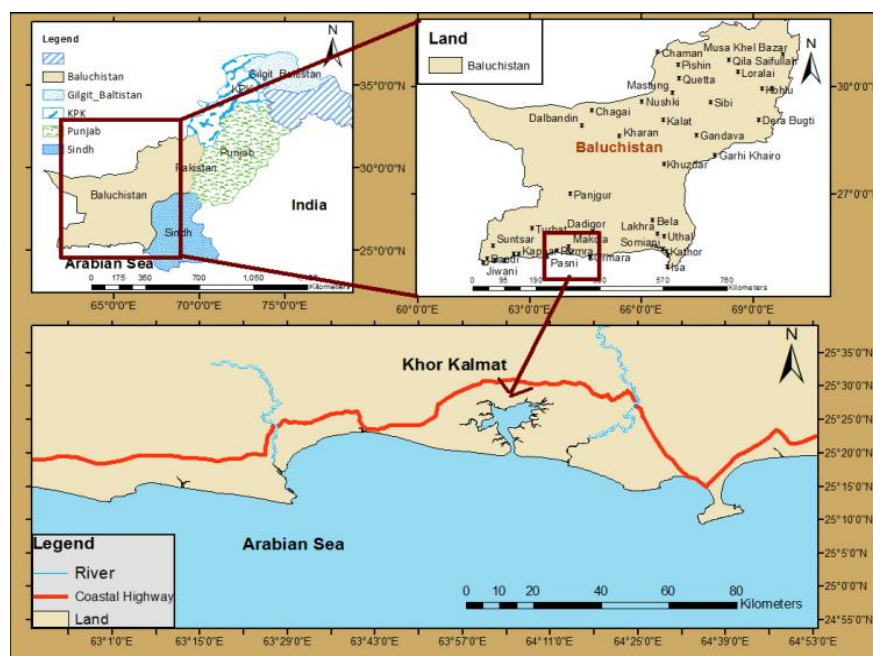


Fig. 1. Study area map

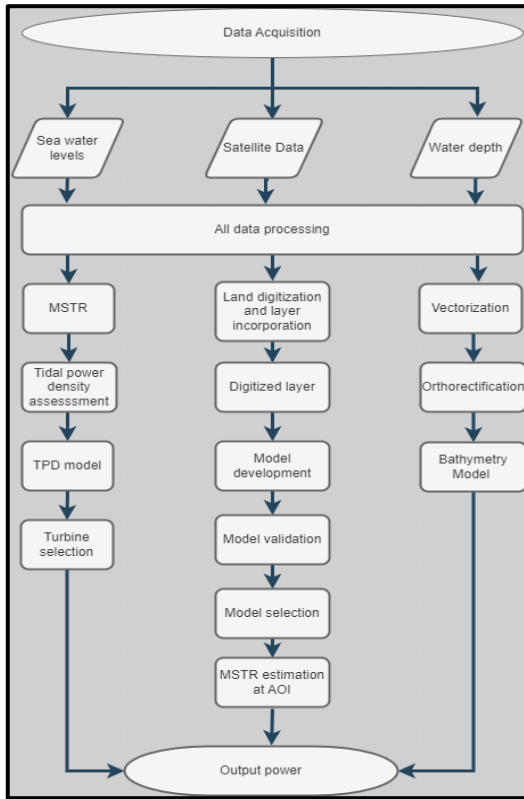


Fig. 2. Estimation methodology

of tides for the estimation of large interval trends. High and Low sea water levels were deduced to compute Mean Spring Tidal Range (MSTR). Environmental Systems Research Institute (ESRI) was retrieved for satellite data [15] and bathymetry data was attained from Hydrography Department, Pakistan [16].

2.2 Validation Method

A cross-validation method was applied to verify the model's accuracy. This method governs the selection of the best model by evaluating statistical error measures. Statistical error measures require the following conditions for the selection of the best model as explained by [17].

1. Root Mean Squared Errors must be small (RMSE)
2. Mean Errors close to zero (ME~0)
3. Mean absolute error (MAE) near to RMSE (MAE ~ RMSE) and both must be small
4. Normalized RMSE must be close to 1 (NRMSE~1)

2.3. Power Density Model

As per [18], potential energy per tide can be assessed as:

$$E = 0.5A\rho gh^2 \text{ (Energy per tide)} \quad (1)$$

Where,

E = Energy per tide

A = area (m²)

ρ = density of seawater (around 1025 kg/m³)

g = Acceleration due to gravity (9.8 m/s²)

h = tidal range (m)

For one tidal period t, mean power (potential) can be computed as:

$$P(\text{mean}) = (A\rho gh^2)/2t \quad (2)$$

For semi-diurnal tides, there are 2 high and low tides. Thus, mean power observed in a day = $(A\rho gh^2/2t) \times 2$

$$P = (A\rho gh^2)/t \quad (3)$$

Hence power density derived from potential energy is evaluated as:

$$P.D._{PE} = (\rho gh^2)/t \quad (4)$$

Power generation using an appropriate tidal turbine can be assessed by using the following relation:

$$P = \rho \times g \times Q \times H \times \eta \quad (5)$$

Where,

P = Power generated by a turbine (MW)

Q = Discharge (m³/s)

H = Water level (m)

η = Efficiency coefficient of turbine

3. RESULTS AND DISCUSSION

3.1. MSTR Model

The MSTR model for AOI was developed by integrating thematic and other layers into the ArcGIS environment. The MSTR model included

MSTRs and physical layers extracted from satellite data, socioeconomic layers (identifying major cities, transportation network, airport, seaport, highways, rivers, fish harbors locations, grid stations and power plants along Makran coast as shown in figure 3).

Geostatistical interpolators; Simple Kriging (SK), Ordinary Kriging (OK) and Universal Kriging (UK) were examined in this study. Results obtained from SK interpolators were found well-fitted and therefore SK interpolators were opted for the development of semi-variogram models. Stable, Spherical, Hole-Effect, Circular and J-Bessel were analyzed (abbreviated as spherical=SPH, circular=CIR, stable=STB, J-Bessel=JB, and hole-effect=HE) and used for the estimation of MSTR at AOI. MSTR models were developed by incorporating STB, SPH, HE, CIR and JB semi-variogram techniques as are shown in figure 4.

Estimated MSTR was compared with observed MSTR for validation purposes and presented in figure 5, demonstrating the results of five models. Developed MSTR models were validated by evaluating statistical error measures of MSTR (shown in figure 6). By considering the conditions of validation as described in section 2.2, it is determined that the CIR model was found best for accomplishing the requirement of the cross-validation method. The implication is that the CIR model is preferred for the assessment of MSTR and is opted to predict MSTR at AOI. The estimated value of MSTR at AOI is assessed as 1.932m.

3.2 Bathymetry Model

The Bathymetry model is necessary for the deployment of tidal turbine and impoundment area calculations. Thus, a comprehensive model for the best visualization of bathymetry for AOI is developed. This model shows adequate water depths in the range of 3.1 to 20.6 m at the proposed lagoon as shown in figure 7.

3.3 Tidal Power Density (TPD) Model

TPD model was established by integrating the MSTR layer, equation 8, physical layer and socioeconomic layer (identifying major cities, transportation networks, airports, seaports, highways, rivers, fish harbors locations, grid stations and power plants along Makran coast as shown in figure 8) into ArcGIS environment. TPD model highlights areas comprising of high and low potential densities ranging between 0.746 W/m^2 to 1.25 W/m^2 . TPD of lagoon lies within the range of $0.818\text{-}0.854 \text{ W/m}^2$.

After analytical analysis of this study, it is observed that AOI is encompassing significant MSTR, ample water depth and natural lagoon structure (requiring less civil construction cost). Therefore, Khor Kalmat is considered as the best region for harnessing tidal energy. Finally, the assessed power output (using equation 5 and $\eta=1$) is evaluated to be 589.6 MW as mentioned in table 3.



Fig. 3. All layers presented as a combined secondary layer for the development of MSTR model

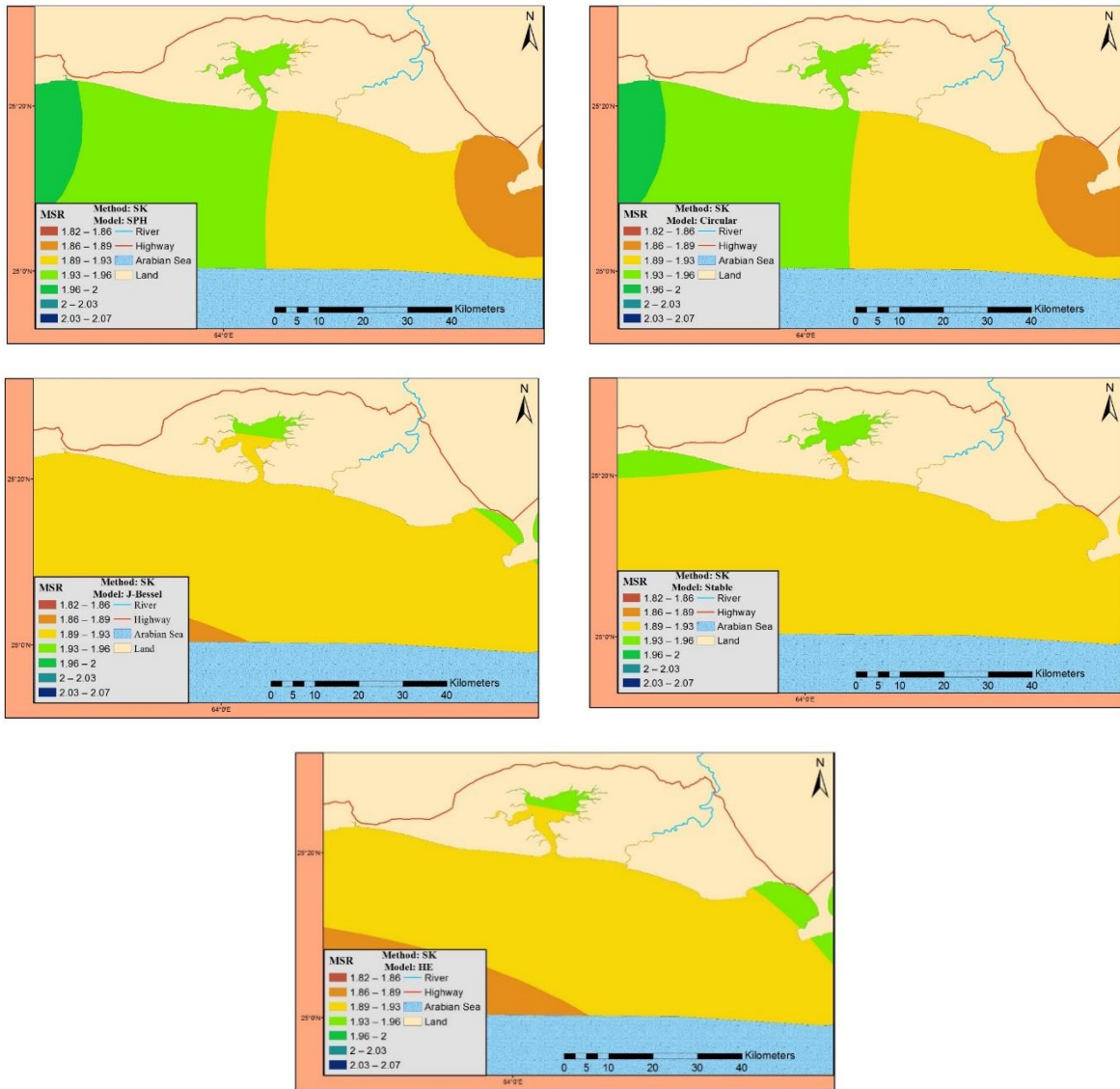


Fig. 4. Geostatistical models for estimating MSTR

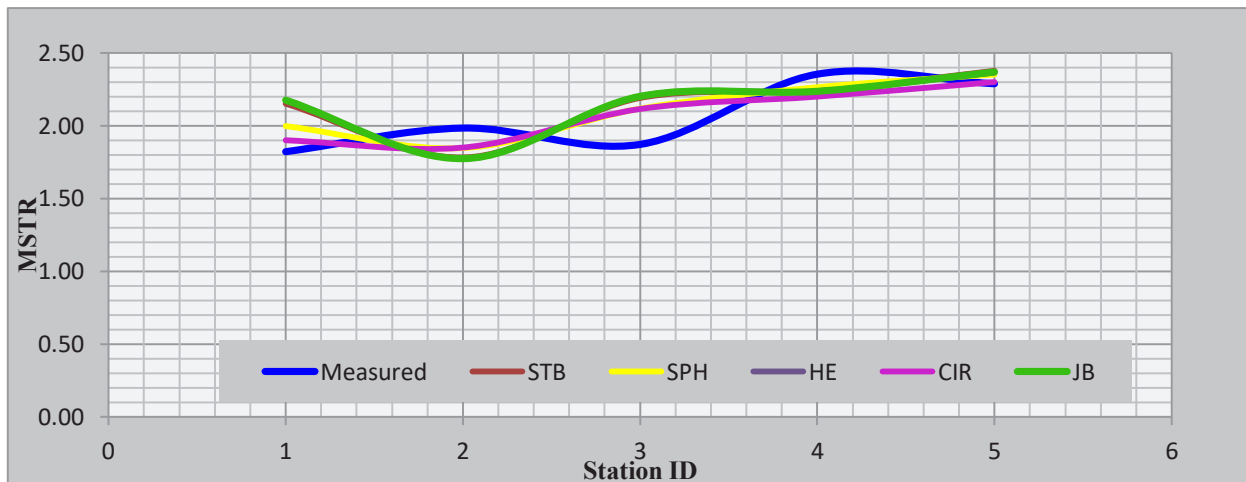


Fig. 5. Measured versus estimated values of MSTR from different models

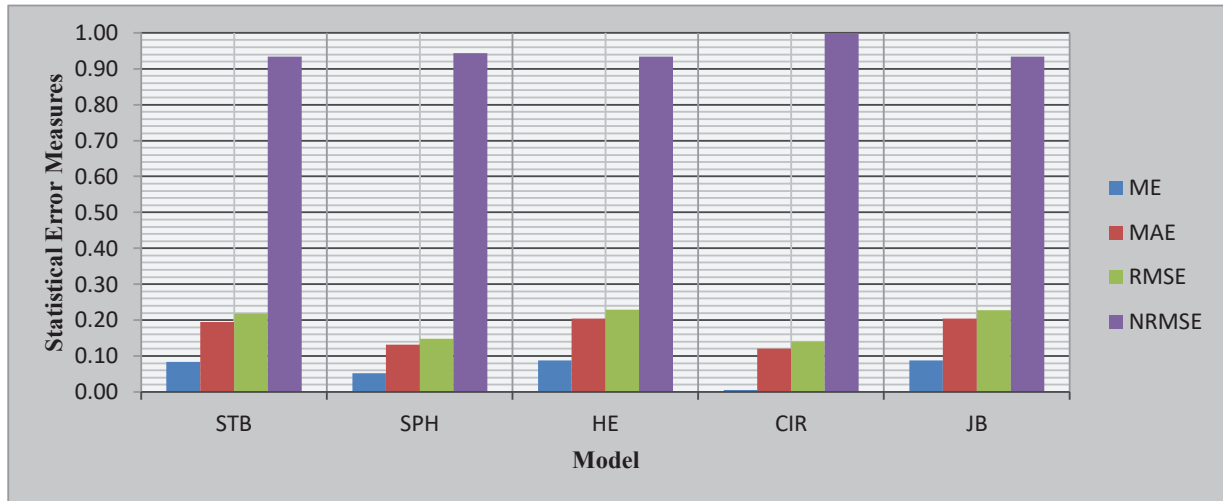


Fig. 6. Statistical error measures

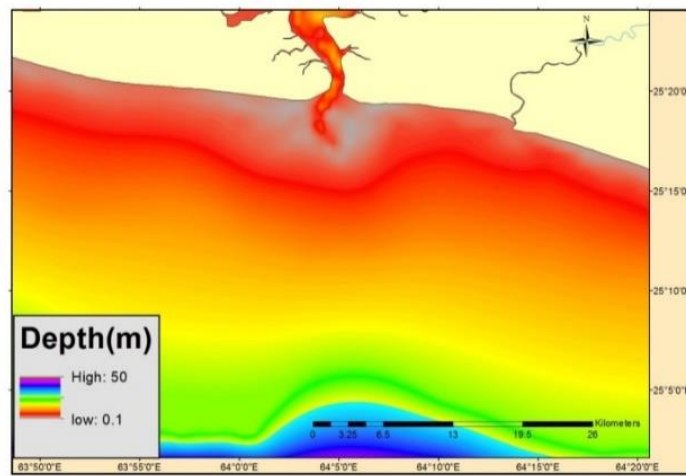


Fig. 7. Bathymetry map study area

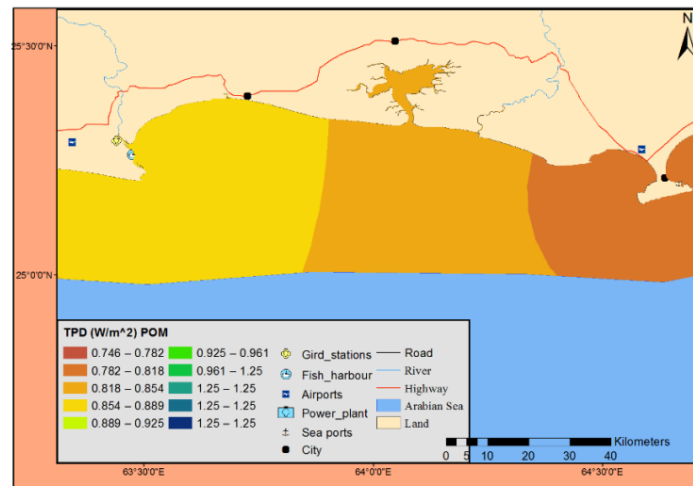


Fig. 8. TPD (W/m^2) of nine years averaged data

Table 3. Assessed tidal power

AOI	Impounded Area (km ²)	Discharge (Q) (m ³ /s)	Power Output (MW)
Khor Kalmat	226.21	30349.84	589.6

3.4 Output Power

Since a moderate tidal range is observed in the study area therefore the study is focused on LH tidal turbines. The main factors of tidal energy generation depend upon size of the tidal pond, tidal range (i.e. head size for turbine) and choice of turbines. The evaluation can be carried out with the help of equation 5.

The selection of a suitable/appropriate turbine would be vital for harnessing tidal energy along with maximum power output. Owing to this, a detailed and conclusive review of latest tidal turbines has been conducted. The technology being used in VLH turbines are found to be the latest one and the movable housing of VLH turbines includes the arrangement of a propeller turbine along with a built-in generator [19].

The proficient method to synchronize VLH sources to conventional turbines is Venturi-Enhanced Turbine Technology ('VETT'). It can also increase the cost-effectiveness of traditional turbines used for the generation of electrical power from VLH sources. VETT uses venture to strengthen head drop through its turbine [20]. Due to this, the VETT turbine was noted to be the most appropriate for the study area. Table 4 depicts the width of the channel region and the area of tidal confinement. The installation configuration of the VETT device can be possible in either unidirectional or bidirectional moreover the study proposed bidirectional installation. The bidirectional

installation is advantageous for the study area because the turbine works with both tides (ebb and flood) with sluicing taking place during times of low water and high water. Therefore, it is expected that four hours per tide generation is possible using the bidirectional installation. The optimal head is required for the generation whereas the startup head for the VETT device is 0.5m. Finally, the total estimated power for the study area is 269.93 watts.

4. CONCLUSION

The rationale of this research is to assess the tidal range energy at tidal lagoon of Khor Kalmat (study area) by incorporating geostatistical modeling. This tidal lagoon of Khor Kalmat was never explored before, for the study of tidal energy. Subsequently, this study provides the preliminary estimation of TE resources. Moreover, the tidal data of Khor Kalmat tidal lagoon was also not available. Therefore, the geostatistical model was developed by utilizing observed data from five available locations for the prediction of MSTR at Khor Kalmat. The moderate tidal ranges as well as a suitable environment were observed for the generation of tidal energy. Satellite imagery was used to complete the above-mentioned tasks with the land imagery digitized into line, point and polygon structures along with further socioeconomic data. The ArcGIS 10.1 software was accessed to digitize the data. The Geostatistical Analysis tool was used to develop MSTR models with the help of incorporated layers. Subsequent to multiple times evaluations and cross-validation of the MSTR model, the prediction of MSTR at Khor Kalmat took place. The identifying areas of sluices, turbine installation and tidal impoundment were carried out through the development of Bathymetry models.

Moreover, depth identification for tidal turbine installation was possible with the help of the Bathymetric model. The potential of tidal lagoon

Table 4. Tidal power plant calculations at AOI

AOI	Impounded Area (km ²)	Sluice width (km)	Q _t (m ³ /s)	Turbine type	No. of turbines	Efficiency	Estimated output power (MW)
Khor Kalmat	226.21	2.26	206	VETT	144	65%	269.93

for tidal power generation has been analyzed by the TPD model. The estimated theoretical output power is 589.6 MW. Keeping above points in view, it is concluded that the installation of bidirectional VETT turbines at the tidal lagoon will be suitable to provide 269.93 MW of tidal output power.

5. CONFLICT OF INTEREST

The authors declare no conflict of interest.

6. REFERENCES

1. R. Pelc, and R.M. Fujita. Renewable energy from the ocean. *Marine Policy* 26: 471-479 (2002).
2. S.A. Abbasi, and N. Abbasi. Renewable energy sources and their environmental impact. *PHI Learning Pvt. Ltd.* (2004).
3. F.O. Rourke, F. Boyle, and A. Reynolds. Tidal energy update 2009. *Applied Energy* 87: 398-409 (2010).
4. A. Etemadi, Y. Emami, O. AsefAfshar, and A. Emdadi. Electricity generation by the tidal barrages. *Energy Procedia* 12: 928-935 (2011).
5. C. Baker. Tidal power. *Energy Policy* 19: 792-797 (1991).
6. F. Harris. Catching the tide: a review of tidal energy systems. *School Science Review* 95: 123 (2014).
7. S.P. Neill, A. Angeloudis, P.E. Robins, I. Walkington, S.L. Ward, I. Masters, M.J. Lewis, M. Piano, A. Avdis, M.D. Piggott, G. Aggidis, P. Evans, T.A.A. Adcock, A. Zidonis, R. Ahmadian, and R. Falconer. Tidal range energy resource and optimization—Past perspectives and future challenges. *Renewable Energy* 127: 763-778 (2018).
8. R. Kempener, and F. Neumann. Ocean Energy Technology Brief 3. *International Renewable Energy Agency IRENA* (2014).
9. J. Chang. Hydrodynamic modeling and feasibility study of harnessing tidal power at the Bay of Fundy. Dissertation Abstracts International, *University of Southern California* 69-06: 3721 (2008).
10. J. Xia, R.A. Falconer, and B. Lin. Hydrodynamic impact of a tidal barrage in the Severn Estuary, UK. *Renewable Energy* 35: 1455-1468 (2010).
11. D. Harries, M. McHenry, P. Jennings, and C. Thomas. Hydro, tidal and wave energy in Australia. *International Journal of Environmental Studies* 63: 803-814 (2006).
12. S. Bhattacharya, and C. Jana. Renewable energy in India: historical developments and prospects. *Energy* 34: 981-991 (2009).
13. P. Chauhan, P. Patel, and S. Sheth. Tidal Stream Turbine-Introduction, current and future Tidal power stations. *National Conference on Innovative and Emerging Technologies SRPEC, Unjha* 413-416 (2015).
14. S. Saifullah, and F. Rasool. Mangroves of Miani Hor lagoon on the north Arabian Sea coast of Pakistan. *Pakistan Journal of Botany* 34: 303-310 (2002).
15. ESRI. Satellite Data Retrieved (2017). <http://www.esri.com/legal/copyright-trademarks> (Accessed October 26, 2017).
16. M.S. Baig, Z. Uddin, and A. Insaf. GIS-linked tidal range energy resource assessment. *Arabian Journal of Geosciences* 14: 1-16 (2021).
17. ESRI. Geostatistical Analyst Using Cross Validation Method. (2017). <http://desktop.arcgis.com/en/arcmap/latest/extensions/geostatistical-analyst/using-cross-validation-to-assess-parameter-values.htm> (Accessed March 2017).
18. J. Twidell, and A.D. Weir. Renewable Energy Resources. *Taylor & Francis, London* (2006).
19. D. Kisliakov, S. Bozhinova, G. Muller, V. Hecht, and S. Schneider. Hydropower converters with head differences below 2.5 m. *Proceedings of ICE: Energy* 166: 107-119 (2013).
20. P. Bird, and P. Roberts. 'VETT' – A New Approach to Very Low Head Tidal Power Generation. *10th European Wave and Tidal Energy Conference*. Aalborg, Denmark (2013).



Evaluation of Air Permeability of Knitted Fabrics at Various Washing Intervals

Mehreen Ijaz*, Namood-e-Sahar, and Zohra Tariq

Department of Home Economics, Lahore College for Women University, Lahore, Pakistan

Abstract: The air permeability of fabrics is one of the most important factors to be considered in making comfortable clothing for consumers. It helps to transport moisture in the form of vapours from the inner skin to the outer environment. This study aims at determining the rate of airflow through the prepared knitted fabrics after various washing intervals. Circular knitted fabrics with 100 % cotton and a blend of cotton and polyester having a ratio of 70 % / 30 % were made by setting different construction parameters. Prepared fabrics were evaluated for their air permeability by following the ASTM D737-1996 test procedure. Then these fabrics were laundered with standard procedure and evaluated after various intervals. It was concluded from the obtained results that construction parameters such as kind of polymer, loop length, hairiness, yarn count, number and size of pores and their distribution play a major role in determining the air permeability of knitted fabrics. Moreover, an increase in washing cycles also reduces the airflow through the fabric.

Keywords: Air Permeability, Knitting, Loop Length, Pore Size, Washing

1. INTRODUCTION

Knitting is one of the most commonly used fabric construction techniques followed by inter looping of yarns running in the direction of either warp or weft. There are a number of rows made with these loops, each loop is pulled through the previous loop and the process goes on. Knitting can be done flat or circular [1]. Knitted garments are comfortable to wear due to their extensibility in their looped structure which fits easily to the body of the wearer. These garments are preferred by consumers due to their easy-to-care properties. These are light in weight and are more porous as compared to other construction techniques [2]. When a fabric is manufactured, a large area covered by a total volume is air space. The pattern of distribution of airspaces has a great influence on certain properties like protection against air, warmth, breeze, wind, dust or rain, thermal conductivity, absorbency, water or moisture absorption etc. [3].

Natural fibers like cotton are hygroscopic in nature and they allow greater absorbency. They can hold moisture in them. On the other hand,

synthetic materials like polyester can hold only a small amount of moisture in them. A combination of both types of fibers can present good results by combining the characteristics of both fibers in a single fabric [4].

Air permeability is one of the functional characteristics of textile materials. It is one of the important parameters to consider while evaluating the comfort of fabrics [5]. Air permeability can be defined as the volume of air measured in mm passed per second from 100 mm² of a textile material at a water head pressure of 10 mm [6]. It is the ability of a fabric to permeate the air through its structure at a given rate under specific conditions for a given time period. Here porosity plays a major role, and it is well understood by various researchers that there exists a strong statistical relationship between air permeability and the porosity of fabrics [7]. The size, amount and shape of pores in a fabric have a great impact on the air permeability of fabrics. The distribution of pores on a substrate either made of knitting or weaving, gives a prediction about how much air can flow through the pores [8].

Table 1. Construction parameters of knitted fabrics

Sample Code	Yarn No. (Ne)	Length of Loop (cm)	Course per cm	Wale per cm	Thickness (cm)	Mass (g/m ²)
AC-1	40	0.27	25	14	0.012	100.21
AC-2	20	0.25	23	12	0.013	101.01
AB-1	40	0.24	21	11	0.012	105.21
AB-2	20	0.22	19	11	0.014	107.52

The evaluation of the air permeability of fabrics is an important aspect to be considered in determining their quality and performance. It helps to identify the intrinsic behaviour of fabrics and must be studied for each manufactured fabric. Different types of construction techniques such as knitting, weaving, felting, napping etc. have a significant effect on the rate of airflow passed through the surface of fabrics. There are multiple factors that can help the manufacturer to alter while making the fabrics in accordance with air permeability; thus providing comfort to the wearer.

Evaluation of the air permeability of knitted fabrics is important to study from commercial and technical points of view. It is the source of physiological comfort to the wearer. As clothing serves as the second skin by protecting the human body from negative external factors. The geometry of textile structure plays an important role in heat transfer between the body and the external environment. Air permeability is the key indicator in this regard. Thus, the thermal properties of raw materials such as fiber and yarn making the textile substrate should be assessed for providing comfort. The main goal of this study was to investigate the rate of airflow through the knitted fabrics after different laundering intervals. A standard test procedure was adopted to measure the rate of airflow through different types of knitted fabrics. Fabrics with different construction parameters were manufactured to note the differences among each tested sample. Results were analyzed statistically through Analysis of Variance (ANOVA).

2. MATERIALS AND METHODS

The circular knitted fabrics were manufactured by the following various construction parameters (Table 1). Two types of fibers such as Cotton 100 % and a blend of Polyester / Cotton 70 % / 30 % were used to prepare simple knit fabrics with medium and tight tightness. Each prepared sample was varied in its yarn number, length of the loop, number of

courses, number of wales per centimetre, thickness and mass.

All the prepared fabrics were then conditioned prior to testing for 24 hours in a standard testing environment with a temperature of $21\text{ }^{\circ}\text{C} \pm 1\text{ }^{\circ}\text{C}$ and relative humidity at $65\% \pm 2\%$ by following the ASTM-D 1776 test method [9]. The air permeability of samples was evaluated by following ASTM standard D737 [10]. A test specimen was cut with the help of a template from each group of samples. The size was approximately 6x6 inches [11]. It was ensured that all specimens were free from wrinkles, creases or folds. These were not taken from or near the edge as properties may vary. Each test specimen was placed on the platform of the air permeability tester. The test was performed at a water pressure of 12.7 mm. The specimen was placed on a circular disk in such a way that it overhung from all sides at least one inch. The fabric was clamped tightly with the ring so that it would not shift from its place. The mounting of specimens was done carefully over the orifice to avoid any air leakage due to the cut edges. In order to protect the cut edges and avoid chances of error, a guard ring around each specimen was fixed. It was raised and held between two parallel plates. On the manometer, the dropped pressure read off directly.

All the knitted samples were washed by following instructions given in the standard M6 Monograph of the American Association of Textile Chemists and Colorists [12]. The front-load machine was used with an agitation speed of 45 rpm. The temperature was set at $60\text{ }^{\circ}\text{C}$ for 12 minutes. The 0.1 gL^{-1} standardized AATCC detergent was added in each cycle. Spinning was done at 1300 rpm for further 12 minutes. The samples were then tumble-dried for one and a half hours at the speed of $68\text{ }^{\circ}\text{C}$. A total of 10 washing cycles were given to the samples. After every 5 cycles, these specimens were labelled and put in a separate packet and assessed for their air permeability at 0 wash, 5 washes and 10 washes.

3. RESULTS AND DISCUSSION





All the obtained data was assessed through Statistical Package for the Social Sciences (SPSS) and presented in the form of mean values and Standard Deviation. The data was observed on repeated observations at intervals of 0-wash, 5 washes and 10 washes, Analysis of Variance (ANOVA) repeated measurement analysis of variance was used to see the difference made with each washing interval. P-value ≤ 0.05 was taken as significant in determining the results. Data was also depicted through multiple lines charts for better understanding.

It was found that the rate of air permeability of fabrics decreased with the increasing number of washing cycles. The washing and drying of fabrics can affect the rate of airflow passing through these materials. It has been observed that the wear and tear conditions can significantly damage the pores of the fabric structure; the lint may adhere to their surface and restricts the airflow [13]. There is a significant difference between the air permeability of studied fabrics. One of the possible reasons is that single-knit fabrics are composed of a porous structure and this porosity increases air permeability [14]. It has

been observed that sample AC-1 and AC-2 has a better rate of air permeability as compared to AB-1 and AB-2. These samples are made with 100% cotton and for this reason, they are associated with hydrophilicity which promotes better air porosity. On the other hand, a fabric made with a combination of cotton and polyester has hydrophobic areas too in its structure that restrict the easy flow of air between the yarns (Table 2). The absorbency of fabrics also affects the air permeability behavior of fabrics. The results are similar to the findings of Guo [11]. It is also observed that the hydrophilicity of cotton fibers makes them swell after absorbing water or any other wet treatment. This swelling brings a change in the dimensional stability and air porosity of fabrics. It also decreases the air passage between component yarns [15].

It was investigated that the size and the total number of pores are the two contributing factors to the air permeability of fabrics. It depicts the phenomenon that the structure of the substrate is very important. As the number of pores increases and the size becomes large, the passage of air will be more to travel through the fabrics [16]. The rate at which air flows through the fabric is largely dependent on its porosity. As porosity increases, the airflow also increases within the fiber and vice

Table 2. Air permeability of samples at various washing intervals

Sample code	Air permeability (cm ³ /sec/cm ²)						p-value	Sample photograph
	0-wash		5-washes		10-washes			
	Mean	SD	Mean	SD	Mean	SD		
AC-1	162.21	1.21	156.32	2.15	148.25	1.25	0.00	
AC-2	155.38	1.15	145.26	1.89	137.56	1.93	0.01	
AB-1	121.45	1.34	111.36	1.69	102.15	1.24	0.00	
AB-2	115.35	2.10	102.53	2.12	93.54	1.55	0.01	

versa [17]. A direct relationship can be observed between air permeability and porosity. It has been observed that fabrics with low porosity result in low air permeability through their structures. One of the main reasons for low air permeability was the lesser number of spaces among yarns, especially in the case of coarse materials. The results are similar to the current study in that as the length of the loop increases, the rate of airflow also increases [18].

The length of the loop also influences the air permeability of fabrics. The effect of structural indicators in the form of loop length was determined and it was found that an increase in the length of the loop in knitted fabrics, makes an increase in the porosity which results in greater permeability to air [3]. This concept is well understood by the fact that as the loop length increases, the spacings between course and wales are also increased, thus the size of the pores enlarges and helps in easy airflow [16]. It is well observed from the findings that the loop length is greater for a sample AC-1 and thus its air permeability is also higher followed by AC-2, AB-1 and AB-2 as shown in Figure 1.

It is also investigated from the results that an increase in laundering cycles, leads to a decrease in air permeability of all specimens. One of the possible reasons of low air permeability is the buildup of lint due to rubbing during laundering cycles. Abrasion caused by washing procedures causes the fibers to accumulate on the surface of fabric and cover the air spaces among yarns. Thus, it restricts the air flow to pass through them [19-20]. P-value less than 0.05 also suggests the same that there is a significant difference in the air permeability of fabrics after each washing interval.

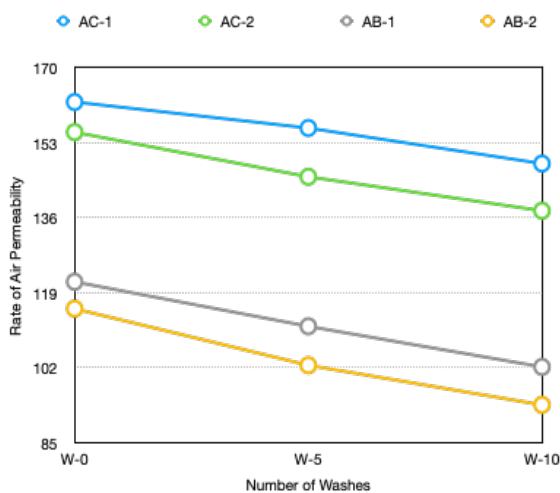


Fig. 1. Air permeability of fabrics

The Fineness of the yarn is another important factor to consider while evaluating the air permeability of fabrics. The finer the fiber, the greater the porosity. It may be due to the reduction in fabric mass because due to increased fineness. On the other hand, coarse yarns reduce the air spaces among yarns and lead towards reduced air porosity and air permeability [21]. Moreover, fine yarns do not prone to yarn hairiness and it has been observed by many researchers that low hairiness also increases the rate of airflow in the fabrics. In fact, hairiness fills up the space among yarns on the substrate and restricts the airflow to pass through them [22]. Thinner fabrics also facilitate the airflow through them. Fine fibers with less hairiness help the air to pass through them with ease [23]. It was also observed by [24] that non-washed samples had the highest rate of air permeability in fabrics. Single-layered fabrics are more permeable to air as compared to double-knit or layered fabrics. It has been observed that double-knit fabrics have more thickness thus restricting the passage of airflow [25]. The air permeability of knitted fabric was affected by certain factors such as its structure, yarn number, thickness, mass and density [26]. It has been investigated that as the yarn becomes smoother and finer, the air permeability increases due to the smaller number of yarns across the structure. It was due to the reason that the pores of the yarns among loops were opened and allowed the air to pass through them [27].

4. CONCLUSION

It was concluded from the findings that construction parameters in knitted fabrics have a significant effect on the air permeability of finished products. The rate of airflow decreased with an increase in washing cycles. It was found that thickness, yarn number and length of the loop were the most important determinants of air permeability through the knitted fabrics. Fabrics permeable to air provide comfort to the wearer. This study was limited to laboratory experiments; other follow-up studies can lead to measuring the comfort level of the wearer through wear trials. Moreover, future studies can be conducted to determine the rate of flow through woven and non-woven fabrics manufactured with different construction parameters. A comprehensive comparison between various construction techniques can be made against air permeability through these materials. The findings can be served as a helpful tool in designing and manufacturing

comfortable clothing products. It can provide a framework for establishing new guidelines for knitted products in relation to their air permeability and porosity.

5. CONFLICT OF INTEREST

The authors declare no conflict of interest.

6. REFERENCES

1. S.C. Ray. Fundamentals and advances in knitting technology. *CRC Press* (2012).
2. T. Dias, and G.B. Delkumburewatte. Changing porosity of knitted structures by changing tightness. *Fibers and Polymers* 9(1): 76-79 (2008).
3. R.T. Ogulata, and S. Mavruz. Investigation of porosity and air permeability values of plain knitted fabrics. *Fibers and Textile in Eastern Europe* 18(5): 71-75 (2010).
4. N. Erdumlu, and B. Ozipek. Investigation of regenerated bamboo fibre and yarn characteristics. *Fibers and Textile in Eastern Europe* 16(4): 69-75 (2008).
5. Z. Zupin, A. Hladnik, and K. Dimitrovski. Prediction of one-layer woven fabrics air permeability using porosity parameters. *Textile Research Journal* 82(2): 117-128 (2012).
6. N.A. Kotb, A.A. Salman, and H.M. Ghazy. Quality of summer knitted fabrics produced from microfiber/cotton yarns. *Journal of Basic and Applied Research Basic* 1(12): 3416-3423 (2011).
7. M. Havlova. Model of vertical porosity occurring in woven fabrics and its effect on air permeability. *Fibers and Textile in Eastern Europe* 22(4): 75-86 (2014).
8. R.B. Turan, A. Okur, and R. Deveci. Predicting the intra-yarn porosity by image analysis method. *Textile Research Journal* 82(16): 1720-1728 (2012).
9. ASTM International. ASTM D1776 Standard practice for conditioning and testing textiles. *West Conshohocken, PA: ASTM International* (2010).
10. ASTM D737 Test method for air permeability of textile fabrics. *West Conshohocken, PA: ASTM International* (1996).
11. J. Guo. The effects of household fabric softeners on the thermal comfort and flammability of cotton and polyester fabrics. *PhD Thesis, Virginia Tech, USA* (2003).
12. AATCC. Monograph M6. *Standardization of home laundry test conditions*. American Association of Textile Chemists and Colorists. (2011). Retrieved from <https://www.scribd.com/document/73811790/Aatcc-Washer#> (accessed 2 December 2022)
13. F.T. Fung, H. Lubos, and B. Vladimir. A study of air permeability influences on pattern cutting. *Fibers and Textiles* 4(1):19-25 (2019).
14. F. Selli, and Y. Turhan. Investigation of air permeability and moisture management properties of the commercial single jersey and rib knitted fabrics. *Textile and Apparel* 27(1): 27-31 (2017).
15. J.A. Wehner, B. Miller, and L. Rebenfeld. Moisture induced changes in fabric structure as evidenced by air permeability measurements. *Textile Research Journal* 57(5): 247-256 (1987).
16. A. Bivainyt, and D. Mikucioniene. Investigation on the air and water vapour permeability of double-layered weft knitted fabrics. *Fibers and Textile in Eastern Europe* 19(3): 69-73 (2011).
17. T.L. Vigo. Textile processing and properties: Preparation, dyeing, finishing and performance. *Elsevier Science* (2013).
18. D. Haroglu. Modeling the air permeability of pile loop knit fabrics using fuzzy logic and artificial neural network. *The Journal of The Textile Institute* 5(1): 1-8 (2022).
19. H.L. Ward. Textile softeners for home laundering. *Journal of home economics* 49(2): 122-123 (1957).
20. F. Kishwar. Investigations related to hydrodynamic characteristics and safety profile of surgical gowns. *PhD Thesis, University of the Punjab, Pakistan* (2013).
21. S.S. Bhattacharya, and J.R. Ajmeri. Air Permeability of Knitted fabrics made from Regenerated Cellulosic fibres. *International Journal of Engineering Research and Development* 10(7):16-22 (2014).
22. M. Havlova, and J. Spankova. Porosity of Knitted Fabrics in the Aspect of Air Permeability-Discussion of Selected Assumptions. *Fibers and Textile in Eastern Europe* 25(3): 86-91 (2017).
23. Q. Chen, F. Jie, M. Bomou, F. Bailu, Z. Rong, and F. Jintu. Development of tricot warp knitted fabrics with moisture management for casual shirt. *Fashion and Textiles* 9(1): 1-16 (2022).
24. G.K. Gunaydin, and E.K. Ceven. Effect of wet laundering on stretching and air permeability properties of polyester warp knitted fabrics with different fabric weights. *Iudağ Üniversitesi Mühendislik Fakültesi Dergisi* 23(3): 61-72 (2018).
25. Z. Degirmenci, and E. Coruh. Comparison of the performance and physical properties of plain, pique, double-pique and fleeced knitted fabrics. *Textile and Apparel* 26(2):159-165 (2016).
26. T. Rajan, and D. Subrata. Evaluation of air permeability behaviour of warp knitted spacer fabrics. *Indian Journal of Fiber and Textile Research* 45(3): 16-22 (2020).
27. R. Mishra, J. Hafsa, H.S.Y. Sheraz, H. Uzair, N. Muhammad, P. Michal, T. Martin, and M. Miroslav. Thermo physiological comfort of single jersey knitted fabric derivatives. *Fashion and Textiles* 8(1): 1-22 (2021).



Mathematical Analysis of Conducting and Dielectric Sphere in Fractional Space

Muhammad Imran Shahzad^{1*}, Muhammad Akbar², Saeed Ahmed³, Sania Shaheen¹,
and Muhammad Ahmad Raza⁴

¹Department of Applied Physics, Federal Urdu University of Arts, Science & Technology,
Islamabad, Pakistan

²Department of Electronics, Quaid-i-Azam University, Islamabad, Pakistan

³Department of Physics, Quaid-i-Azam University, Islamabad, Pakistan

⁴Department of Statistics, Federal Urdu University of Arts, Science & Technology,
Islamabad, Pakistan

Abstract: This paper presents an analytical analysis of a sphere placed in fractional dimensional space. The Laplacian Equation in fractional space describes physics as a complex phenomenon. The general solution of the Laplacian equation in fractional space is obtained by the separable variable technique. We have investigated a close form solution for conducting sphere and dielectric sphere. Further, the electric potential and charge density, induced due to a point charge is calculated in fractional space, and also the energy radiated by the sphere is determined. The results are compared with the classical results by setting the fractional parameter $\alpha = 3$ which normally lies in the limit $2 < \alpha \leq 3$.

1. INTRODUCTION

The idea of fractional dimensional space (FD Space) is very useful in the various branches of physics and it has been discussed by many researchers. Various scientists have applied it accordingly as Wilson [3] has discussed quantum field theory in fractional space. Further, the fractional space can be used as a parameter in the Ising limit of quantum field theory [6]. Stillinger [4] has given a brief introduction to this theme for the formulation of Schrodinger and Gibbsian statistical mechanics in the fractional space. Svozil and Zeilinger [10] have investigated operationalistic meanings of the dimension of space time that provides the possibility of predicted space time dimension. It is already stated that the fractional space time is less than 4. In the new era, Gauss law [11] has been formulated in the FD space. The solutions of electrostatic problems, have also been investigated in the fractional space for.

In this paper, we have focused on the problem of a sphere in an electrostatic field [16] and worked it out for fractional space. Some researchers [17] have also discussed this problem in fraction dimensional space. But we have calculated the electric field and

energy in fractional dimensional space. We have also calculated its energy, charge density, dipole moment and electric field in fractional space for the outside sphere as well as inside the sphere. We have considered here both cases of the sphere “conducting and dielectric” in the electrostatic field. We have solved this problem analytically. First, we consider a conducting sphere, then we solve it for a dielectric sphere and finally, we solve for an electric field and energy radiated by the sphere. For the integer order, the original classical solution can be recovered.

2. MATHEMATICAL MODEL

Let us consider a conducting sphere (as shown in Figure 1) having radius r_1 embedded in the host medium of permittivity ϵ_2 [16]. The point charge q is situated on $z - axis$ at $z = \zeta > r_1$. In FD space, we will find the potential on the sphere as well as the charge distribution. At any point outside the sphere, the entire potential is given as $\phi = \phi_0 + \phi_1$, where ϕ_0 is known as the potential of the outer source q and ϕ_1 indicates the potential of the induced charge distribution on the sphere. This potential is single valued, as in Stratton [16], and can be expressed as:

$$\phi_1 = \sum_{m=0}^{\infty} \sum_{n=0}^{\infty} \left(A_{nm} r^n + \frac{B_{nm}}{r^{n+1}} \right) P_n^m(\cos\theta) \exp \Im \psi \quad (1)$$

where the unknown arbitrary constants are A_{nm} and B_{nm} . But ϕ_1 must be analytic at infinity, as we set $A_{nm} = 0$. Further, the potential ϕ_0 is primary and symmetric about z -axis, here $m = 0$, in this case. Therefore, the potential of the induced charge distribution on the sphere can be expressed as:

$$\phi_1 = \sum_{n=0}^{\infty} \frac{B_n}{r^{n+1}} P_n(\cos\theta) \quad (2)$$

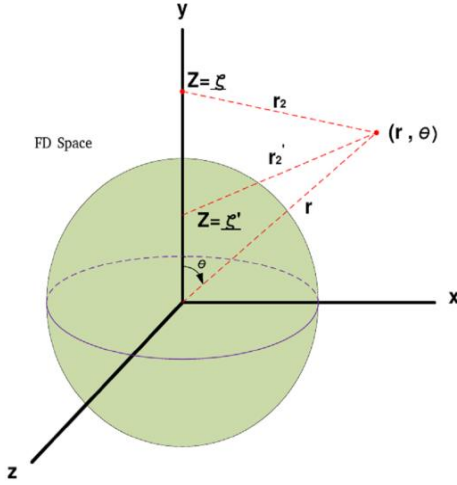


Fig. 1. A sphere placed in fractional dimensional space

In fractional space we can express as:

$$\phi_1 = \sum_{l=0}^{\infty} \frac{B_l}{r^{l+\alpha-2}} C_l^{\alpha/2-1}(\cos\theta), (2 < \alpha \leq 3) \quad (3)$$

When $r < \zeta$, the expansion of the primary potential ϕ_0 can be expressed as:

$$\phi_0 = \frac{1}{4\pi\epsilon_2} \frac{q}{r_2} = \frac{1}{4\pi\epsilon_2} \frac{q}{\zeta} \sum_{l=0}^{\infty} \left(\frac{r}{\zeta} \right)^l C_l^{\alpha/2-1}(\cos\theta), (\alpha \leq 3) \quad (4)$$

The resultant potential at the surface of sphere $r = r_1$ is:

$$\phi(r_1, \theta) = \phi_s = \sum_{l=0}^{\infty} \left[\frac{1}{4\pi\epsilon_2} \frac{q}{\zeta} \left(\frac{r_1}{\zeta} \right)^l + \frac{B_l}{r_1^{l+\alpha-2}} \right] C_l^{\alpha/2-1}(\cos\theta), (2 < \alpha \leq 3) \quad (5)$$

As ϕ_s is constant and since the above equation must be valid for all values of θ , it means that the coefficients of $C_l^{\alpha/2-1}(\cos\theta)$ must go to zero for all values of $l > 0$. Here, the unknown coefficient b_n can be determined from the following set of relations:

$$b_0 = r_1 \phi_s - \frac{q}{4\pi\epsilon_2} \frac{r_1}{\zeta} \quad (6)$$

$$B_l = \frac{-q}{4\pi\epsilon_2} \frac{q r_1^{2l+\alpha-2}}{\zeta^{l+1}}, (l > 0) \quad (7)$$

At any point, the potential outside the sphere is:

$$\phi = \frac{r_1 \phi_s}{r} + \frac{1}{4\pi\epsilon_2} \frac{q}{r_2} - \frac{q}{4\pi\epsilon_2} \sum_{l=0}^{\infty} \frac{r_1^{2l+\alpha-2}}{\zeta^{l+1}} \frac{C_l^{\alpha/2-1}(\cos\theta)}{r^{l+\alpha-2}}, (2 < \alpha \leq 3) \quad (8)$$

To find the charge density [16], we can calculate the normal derivatives on the surface of the sphere as:

$$\left(\frac{\partial \phi}{\partial r} \right)_{r=r_1} = \frac{-\phi_s}{r_1} + \frac{q}{4\pi\epsilon_2} \sum_{l=0}^{\infty} (l + \alpha - 2) \frac{r_1^{l-1}}{\zeta^{l+1}} C_l^{\alpha/2-1}(\cos\theta), (2 < \alpha \leq 3) \quad (9)$$

and the induced charge density can be calculated as:

$$\omega = -\epsilon_2 \left(\frac{\partial \phi}{\partial r} \right)_{r=r_1} = \epsilon_2 \frac{\phi_s}{r_1} - \frac{q}{4\pi} \sum_{l=0}^{\infty} (l + \alpha - 2) \frac{r_1^{l-1}}{\zeta^{l+1}} C_l^{\alpha/2-1}(\cos\theta), (2 < \alpha \leq 3) \quad (10)$$

The entire charge on the sphere is thus given as:

$$q_1 = \int_0^\pi \int_0^{2\pi} \omega r_1^2 \sin\theta d\theta d\psi \quad (11)$$

Now using the orthogonality property of Legendre functions, we find:

$$\int_0^\pi C_l^{\alpha/2-1}(\cos\theta) C_{l'}^{\alpha/2-1}(\cos\theta) \sin\theta d\theta = 0, \quad \text{when } l \neq l' \quad (12)$$

where,

$$C_0^{\alpha/2-1}(\cos\theta) = 1 \text{ and } C_1^{\alpha/2-1}(\cos\theta) = (\alpha - 2)\cos\theta$$

We take $l' = 0$, $C_0^{\alpha/2-1}(\cos\theta) = 1$ and then $C_l^{\alpha/2-1}(\cos\theta)$ vanishes when integrated for the limit 0 to π for all $l > 0$, thus we have:

$$q_1 = 4\pi\epsilon_2 r_1 \phi_s - q(\alpha - 2) \frac{r_1}{\zeta} \quad (13)$$

Therefore, the potential of the sphere is given as:

$$\phi_s = \frac{1}{4\pi\epsilon_2} \frac{q_1}{r_1} + \frac{(\alpha-2)q}{4\pi\epsilon_2} \frac{q}{\zeta} \quad (14)$$

Thus the potential for the integer order $\alpha = 3$ can be found as follows:

$$\phi_s = \frac{1}{4\pi\epsilon_2} \frac{q_1}{r_1} + \frac{1}{4\pi\epsilon_2} \frac{q}{\zeta} \quad (15)$$

where q_1 is showing the excess of the charge so it has been placed on the isolated sphere. Here, for a simple interpretation we choose the point $z = \zeta'$ such that $\zeta\zeta' = r_1^2$ is said to be the inverse of $z = \zeta$. In this way we can write,

$$\frac{1}{r_2'} = \sum_{l=0}^{\infty} \left(\frac{r_1^{2l}}{\zeta^l} \right) \frac{C_l^{\alpha/2-1}(\cos\theta)}{r^{l+\alpha-2}}, \quad (2 < \alpha \leq 3) \quad (16)$$

Thus, the resultant potential is given as follows:

$$4\pi\epsilon_2\phi = \frac{q}{r_2} + \frac{q_1}{r} + \frac{qr_1}{\zeta} \frac{1}{r} - (\alpha - 2) \frac{qr_1}{\zeta} \frac{1}{r_2}, \quad (2 < \alpha \leq 3) \quad (17)$$

Next, we will determine electric potential due to point charge [16] outside and inside the sphere. At any point outside the sphere, the conductivity is zero and the inductive capacity is ϵ_1 , thus the potential is given by:

$$\phi^+ = \phi_0 + \phi_1^+ = \frac{1}{4\pi\epsilon_2} \frac{q}{r_2} + \sum_{l=0}^{\infty} \frac{B_l}{r^{l+\alpha-2}} C_l^{\alpha/2-1}(\cos\theta), \quad (2 < \alpha \leq 3) \quad (18)$$

The symbol ϕ^+ shows the potential or field outside the sphere.

$$\phi^- = \sum_{l=0}^{\infty} A_l r^l C_l^{\alpha/2-1}(\cos\theta), \quad (r < r_1) \quad (19)$$

The Notation ϕ^- represents the potential inside the sphere and the induced polarization.

$$\phi^+ = \sum_{l=0}^{\infty} \left[\frac{1}{4\pi\epsilon_2} \frac{q}{\zeta} \left(\frac{r}{\zeta} \right)^l + \frac{B_l}{r_1^{l+\alpha-2}} \right] C_l^{\alpha/2-1}(\cos\theta), \quad (2 < \alpha \leq 3) \quad (20)$$

Where,

$$\frac{1}{r_2} = \frac{1}{4\pi\epsilon_2} \frac{q}{\zeta} \sum_{l=0}^{\infty} \left(\frac{r}{\zeta} \right)^l C_l^{\alpha/2-1}(\cos\theta)$$

Across the boundary, we find that:

$$\phi^+ = \phi^- \quad (21)$$

$$\epsilon_2 \left[\frac{\partial\phi^+}{\partial r} \right]_{r=r_1} = \epsilon_1 \left[\frac{\partial\phi^-}{\partial r} \right]_{r=r_1} \quad (22)$$

from the first boundary condition, we can calculate:

$$A_l r_1^l = \frac{1}{4\pi\epsilon_2} \frac{q}{\zeta^{l+1}} r_1^l + \frac{B_l}{r_1^{l+\alpha-2}} \quad (23)$$

2nd boundary condition leads us to the following:

$$\epsilon_1 A_l l r_1^{l-1} = \frac{1}{4\pi} \frac{q}{\zeta^{l+1}} l r_1^{l-1} - \epsilon_2 (l + \alpha - 2) \frac{B_l}{r_1^{l+\alpha-1}} \quad (24)$$

By simplification, we obtain the unknowns as follows:

$$B_l = \frac{qr_1^{2l+\alpha-2} (\epsilon_2 - \epsilon_1)}{4\pi\zeta^{l+1} \epsilon_2} \frac{l}{\epsilon_1 l + \epsilon_2 (l + \alpha - 2)} \quad (25)$$

and

$$A_l = \frac{q}{4\pi\zeta^{l+1} \epsilon_1 l + \epsilon_2 (l + \alpha - 2)} \quad (26)$$

At any point, the potential outside the sphere is given as:

$$\phi^+ = \frac{1}{4\pi\epsilon_2} \frac{q}{r_2} + \frac{q}{4\pi} \frac{(\epsilon_2 - \epsilon_1)}{\epsilon_2} \sum_{l=0}^{\infty} \frac{l}{\epsilon_1 l + \epsilon_2 (l + \alpha - 2)} \frac{r_1^{2l+\alpha-2}}{\zeta^{l+1}} \frac{C_l^{\alpha/2-1}(\cos\theta)}{r^{l+\alpha-2}}, \quad (2 < \alpha \leq 3) \quad (27)$$

and also the potential inside the sphere is given as:

$$\phi^- = \frac{q}{4\pi\zeta^{l+1}} \sum_{l=0}^{\infty} \frac{2l + \alpha - 2}{\epsilon_1 l + \epsilon_2 (l + \alpha - 2)} r^l C_l^{\alpha/2-1}(\cos\theta), \quad (r < r_1) \quad (28)$$

For $l = 1$, at any point, the potential outside the sphere can be calculated as:

$$\phi^+ = \frac{1}{4\pi\epsilon_2} \frac{q}{r_2} + \frac{q}{4\pi} \frac{(\epsilon_2 - \epsilon_1)}{\epsilon_2} \frac{1}{\epsilon_1 + \epsilon_2 (\alpha - 1)} \frac{r_1^{\alpha} (\alpha - 2) \cos\theta}{\zeta^2 r^{\alpha-1}}, \quad (2 < \alpha \leq 3) \quad (29)$$

and the potential inside the sphere is given as:

$$\phi^- = \frac{q}{4\pi\zeta^2} \frac{\alpha}{\epsilon_1 + \epsilon_2 (\alpha - 1)} r (\alpha - 2) \cos\theta, \quad (2 < \alpha \leq 3) \quad (30)$$

For $\alpha = 3$, we can find that the potential at any point outside the sphere is given as:

$$\phi^+ = \frac{1}{4\pi\epsilon_2} \frac{q}{r_2} + \frac{qr_1^3}{4\pi\zeta^2} \frac{(\epsilon_2 - \epsilon_1)}{\epsilon_2 (\epsilon_1 + 2\epsilon_2)} \frac{\cos\theta}{r^2} \quad (31)$$

and the potential inside the sphere is calculated as:

$$\phi^- = \frac{q}{4\pi\zeta^2} \frac{3}{\epsilon_1 + 2\epsilon_2} r \cos\theta \quad (32)$$

In this section [16], we find the electric potential and field for a dielectric sphere placed in FD Space. When the point source q deviates from the origin, the field in the vicinity of the sphere becomes parallel and homogeneous. Here, we consider a sphere placed in a host medium of electric constant ϵ_2 under the influence of a uniform parallel, and external field E_0 , which is directed along the positive z - axis. Consequently, the primary potential can be written as follows:

$$\phi_0 = -E_0 z = -E_0 r \cos\theta = -E_0 r P_1(\cos\theta) \quad (33)$$

In FD space, the primary field is given:

$$\begin{aligned}\phi_0 &= -E_0 z = -E_0 r C_1^{\frac{\alpha}{2}-1} (\cos\theta) \\ &= -E_0 r (\alpha - 2) \cos\theta\end{aligned}\quad (34)$$

When ϕ_0 is not continuous at infinity, and for the source, it is itself infinitely remote. The potential at any point outside the sphere is because of either the induced surface charge or the polarization and is given as:

$$\phi_1^+ = \sum_{l=0}^{\infty} \frac{B_l}{r^{l+\alpha-2}} C_l^{\alpha/2-1} (\cos\theta), \quad (2 < \alpha \leq 3) \quad (35)$$

for conducting sphere, then the total potential on the surface of sphere as well as inside the sphere is a constant ϕ_s which is given as:

$$\begin{aligned}\phi_s &= -E_0 r_1 C_1^{\alpha/2-1} (\cos\theta) + \\ \sum_{l=0}^{\infty} \frac{B_l}{r_1^{l+\alpha-2}} C_l^{\alpha/2-1} (\cos\theta), \quad (2 < \alpha \leq 3)\end{aligned}\quad (36)$$

Since ϕ_s is independent of θ , so we can write:

$$B_0 = r_1 \phi_s, \quad B_1 = r_1^\alpha E_0, \quad B_n = 0, \quad \text{for } l > 1 \quad (37)$$

$$\phi^+ = -E_0 r (\alpha - 2) \cos\theta + r_1^\alpha E_0 \frac{(\alpha-2)\cos\theta}{r^{\alpha-1}} + \frac{r_1 \phi_s}{r} \quad (38)$$

Now we will compute the charge density and the total charge density is given as:

$$\omega = -\epsilon_2 \left(\frac{\partial \phi^+}{\partial r} \right)_{r=r_1} \quad (39)$$

Thus we can find the charge density as:

$$\omega = \alpha(\alpha - 2)\epsilon_2 E_0 \cos\theta + \frac{\phi_s r_1}{r}, \quad q_1 = 4\pi\epsilon_2 r_1 \phi_s \quad (40)$$

When $\alpha = 3$,

$$\omega = 3\epsilon_2 E_0 \cos\theta + \frac{\phi_s r_1}{r}, \quad q_1 = 4\pi\epsilon_2 r_1 \phi_s \quad (41)$$

The induced charge surface is due to a dipole moment $p = 4\pi\epsilon_2 r_1^\alpha E_0$.

In case. if the sphere is charged, then q_1 is added to the charge of the sphere. If the sphere is of a dielectric inductive capacity ϵ_1 , then across the boundary conditions we can find the constants A_1 and B_1 . As

$$\phi^+ = \phi^-, \quad r = r_1 \quad (42)$$

$$\epsilon_2 \left(\frac{\partial \phi^+}{\partial r} \right)_{r=r_1} = \epsilon_1 \left(\frac{\partial \phi^-}{\partial r} \right)_{r=r_1} \quad (43)$$

Where $A_0 = 0$, $B_0 = 0$ and $B_n = 0$, $A_n = 0$, when $l > 1$. Then the boundary conditions yield:

$$A_1 = \frac{-\alpha\epsilon_2 E_0}{\epsilon_1 + (\alpha-1)\epsilon_2} \quad \text{and} \quad B_1 = \frac{\epsilon_1 - \epsilon_2}{\epsilon_1 + (\alpha-1)\epsilon_2} E_0 r_1^\alpha$$

The resultant potentials are therefore given as:

$$\phi^+ = -E_0 r (\alpha - 2) \cos\theta + \frac{\epsilon_1 - \epsilon_2}{\epsilon_1 + (\alpha-1)\epsilon_2} E_0 r_1^\alpha \frac{(\alpha-2)\cos\theta}{r^{\alpha-1}} \quad (44)$$

and

$$\phi^- = \frac{-\alpha\epsilon_2}{\epsilon_1 + (\alpha-1)\epsilon_2} E_0 (\alpha - 2) r \cos\theta \quad (45)$$

where $z = r \cos\theta$, inside the sphere, the field $E^- = -\frac{\partial \phi}{\partial z}$ is paprallel and same. Thus,

$$E^- = \frac{\alpha\epsilon_2}{\epsilon_1 + (\alpha-1)\epsilon_2} E_0 (\alpha - 2) \quad (46)$$

The dielectric constant κ_1 of the sphere is either greater or smaller than κ_2 . Thus, the field within the spherical cavity is excited from a homogeneous dielectric constant κ_2 and it is given as:

$$E^- = \frac{\alpha\kappa_2}{1 + (\alpha-1)\kappa_2} E_0 (\alpha - 2) > E_0 \quad (47)$$

Next, we see that the induced field outside the sphere is because of the dipole oriented along the direction of $z - axis$ whose dipole moment is given as:

$$p = 4\pi\epsilon_2 \frac{\epsilon_1 - \epsilon_2}{\epsilon_1 + (\alpha-1)\epsilon_2} E_0 r_1^\alpha \quad (48)$$

Apparently, the characteristics of a spherical cavity look like a dipole. This effect is readily accounted for revealing that the walls of the cavity bear a bound charge of density $\omega' = -n_1 \cdot P_2$, where P_2 is the polarization of the external medium. In the case of a dielectric sphere in the air, we have $\epsilon_2 = \epsilon_0$. The polarization of the sphere is then given as:

$$P_1 = \epsilon_0 (\kappa_1 - 1) E^- = \alpha \frac{\kappa_1 - 1}{\kappa_1 + (\alpha-1)} \epsilon_0 E_0 \quad (49)$$

and its dipole moment is then calculated as:

$$p = \frac{4}{3} \pi r_1^3 \cdot P_1 \quad (50)$$

The energy of the polarized sphere for the external field is thus given as:

$$U_1 = -\frac{1}{2} \int_v P_1 \cdot E_0 dv = -\frac{1}{2} p \cdot E_0 \quad (51)$$

3. CONCLUSION

In this article, the Laplace equation has been solved analytically for the fraction dimensional space. The non-integer dynamics plays a key role in describing the complex phenomenon. We have calculated an electrostatic potential of a conducting sphere as well as a dielectric sphere in fractional space. Moreover, we calculated an electric field and power radiated by the sphere. This is a general and close form solution that can be applied for various materials as host medium as well as core medium. We have checked that by setting alpha parameter equal to 3, the classical results can be recovered.

4. CONFLICT OF INTEREST

The authors declare no conflict of interest.

5. REFERENCES

1. C.G. Bollini, and J.J. Giambiagi. Dimensional renormalization: The number of dimensions as a regularizing parameter. *Il Nuovo Cimento B* 12: 20-26 (1972).
2. J.F. Ashmore. On renormalization and complex space-time dimensions. *Communications in Mathematical Physics* 29: 177-187 (1973).
3. K.G. Wilson. Quantum field-theory models in less than 4 dimension. *Physical Review D* 7: 2911-2926 (1973).
4. F.H. Stillinger. Axiomatic basis for spaces with non integer dimension. *Journal of Mathematical Physics* 18: 1224-1234 (1977).
5. X.F. He. Excitons in anisotropic solids: The model of fractional-dimensional space. *Physical Review B* 43: 2063-2069 (1991).
6. C.M. Bender, and S. Boettcher. Dimensional expansion for the Ising limit of quantum field theory. *Physical Review D* 48: 4919-4923 (1993).

7. C.M. Bender, and K.A. Milton. Scalar Casimir effect for a D-dimension sphere. *Physical Review D* 50: 6547-6555 (1994).
8. V.E. Tarasov. Fractional generalization of Liouville equations. *Chaos* 14: 123-127 (2004).
9. V.E. Tarasov. Electromagnetic fields on fractals. *Modern Physics Letters A* 21: 1587-1600 (2006).
10. A. Zeilinger, and K. Svozil. Measuring the dimension of space-time. *Physical Review Letters* 54: 2553-2555 (1985).
11. S. Muslih, and D. Baleanu. Fractional multipoles in fractional space. *Nonlinear Analysis: Real World Applications* 8: 198-203 (2007).
12. C. Palmer, and P.N. Stavrinou. Equations of motion in a non integer-dimension space. *Journal of Physics A* 37: 6987-7003 (2004).
13. J.D. Jackson. Classical Electrodynamics, 3rd edition. *Wiley, New York* (1999).
14. D.J. Griffiths. Introduction to Electrodynamics, 4th Edition. *Pearson Education* (2012).
15. T. Myint-U, and L. Debnath. Linear Partial Differential Equations for Scientists and Engineers, 4th Edition. *Birkhauser* (2007).
16. V.E. Tarasov. Gravitational field of fractals distribution of particles. *Celestial Mechanics and Dynamical Astronomy* 94: 1-15 (2006).
17. J.A. Stratton. Electromagnetic Theory. *Wiley-IEEE Press* 640 (1941).
18. D. Baleanu, A.K. Golmankhaneh, and A.K. Golmankhaneh. On electromagnetic field in fractional space. *Nonlinear Analysis: Real World Applications* 11: 288-292 (2010).
19. P.M. Morse, and H. Feshbach. Methods of Theoretical Physics. *McGraw-Hill Book Comp., Inc., New York, Toronto, London, Part II* 260: 208-209 (1953).



Investigation of Groundwater Quality for Drinking Usage in Kifri District (Iraq) by using NPI and WQI Indices

Abdulmutalib Raafat Sarhat¹, Muhammad Mohsin^{2*}, and Aram Hassan Mohammed³

¹Department of Chemistry, College of Education, University of Garmian, Kurdistan, Iraq

²Department of Geography, Govt. Sadiq Egerton Graduate College, Bahawalpur, Pakistan

³Department of Social Sciences, College of Basic Education, University of Garmian, Kurdistan, Iraq

Abstract: The present study was mainly proposed to investigate the quality of groundwater for drinking in Kifri District. The main aim of this study was to identify some pollutants of groundwater using two types of indexes which are: Nemerow's pollution index (NPI) and Water quality index (WQI). The groundwater samples were collected from 36 stations (deep wells) and analyzed for seven physico-chemical parameters including EC, TDS, pH, TH, TA, Ca^{+2} and SO_4^{-2} ; as well as, the results were compared to WHO standards. The results presented undesirable values for almost all physico-chemical parameters, according to WHO standard limits for drinking. Based on WQI, the results show that 33 stations out of 36 were classified under the 'Poor Quality' category. Also, most of the NPI values of EC, TDS, Ca^{+2} , TH, TA, and SO_4^{-2} concentrations were (>1) and exceeded the WHO standard. Thus, all the stations reported high values of WQI and NPI and all the groundwater samples belonged to polluted water.

Keywords: Groundwater Quality, Water Quality Index (WQI), Nemerow's Pollution Index (NPI), Kifri District, Iraq.

1. INTRODUCTION

Generally, drinking water plays a big role in human life, and humans have the right to access safe and affordable water in order to sustain good health because access to safe drinking water has benefits for human health [1]. However, poor quality of drinking water affects human health, especially children and infants who are highly exposed to contaminants [2]. Groundwater is considered a common resource of water for human consumption including drinking, industrial, irrigation and construction. Generally, groundwater is preferable to surface water due to a number of reasons. For instance, groundwater mostly has better quality; it is also well protected from contaminants sources and is less subjected to seasonal changes [3]. However, sometimes the groundwater is of poor quality because of the aquifers, which contain undesirable elements in large quantities, as is the case in the study area. The chemistry of groundwater highly depends on some factors including general geology, types of rock weathering as well as the quality of recharged water [4]. The sustainable supply

of potable water is highly ambiguous in most developing countries therefore the assessment of groundwater quality is significant to ensure that the water is suitable and safe to be used [5,6]. Usually, the hydro-chemical assessment of groundwater is based on large amounts of information in terms of groundwater chemistry [7]. The excessive elements of groundwater are a global public health concern, as some elements and compounds are responsible to cause deleterious effects on human health. Kifri District is one of the cities of Iraq where groundwater has been the only water supply for all sectors for a long time. All the people in this district are utilizing groundwater for household usage. Based on a previous study, the quality of groundwater in Kifri District has high concentrations of some pollutants such as Ca^{+2} , Mg^{+2} , Fe^{+2} , and SO_4^{-2} which significantly exceeded the WHO and FAO drinking water quality standards [8]. The present paper aimed to investigate the possibility of using groundwater for drinking purposes by collecting samples from different stations in the city. For this purpose, Nemerow's Pollution Index (NPI)

and Water quality index (WQI) have been utilized considering the World Health Organization (WHO) standards [9]. The findings of this study are expected to pave the way to increase public consciousness on using groundwater for various usages, especially for drinking; then, this will promote the authorities to take some actions for finding new sources of safe water.

2. METHODOLOGY

2.1 Study Area

The study area of the present study was the Kifri District, about 100 Km southeast Kirkuk city, Iraq (Figure 1). It is geographically situated between $34^{\circ} 27' 24'' - 35^{\circ} 10' 17''$ N latitudes and $44^{\circ} 31' 4'' - 45^{\circ} 16' 52''$ E longitudes.

2.2 Data Collection and Mapping

A (GPS) device was used to record the locations of the sampling stations. The collected data were properly arranged and manipulated according to the

study's needs. Also, cartography was conducted by utilizing cross-sectional maps prepared in ArcGIS 10.7 and ERDAS Imagine 14 software. The method of quantitative analysis was used to download the maps. The study area map was drawn on a scale of 1: 250000 for the year 2021.

2.3 Sampling Analysis

The samples were taken and collected in (1 L) polypropylene bottles, and all the samples were labelled. Then, 0.4 % HNO_3 was added in each collected sample and stored in a refrigerator.

Some of the parameters such as pH, TDS and EC were immediately measured after sampling in the site by using digital pH and conductivity TDS meters. The samples were analyzed to determine Ca^{+2} and total hardness (TH) by Titration with EDTA (Ethylenediaminetetraacetic Acid). Also, SO_4^{-2} were determined by an ion-selective electrode with specific parameters comprising a sulphate

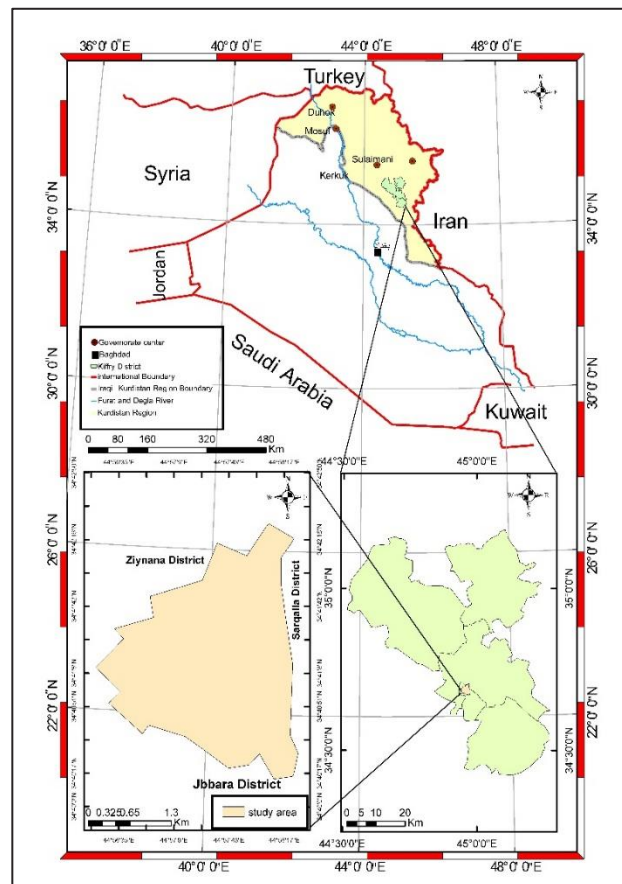


Fig. 1. Location of the studied area

Source: Directorate of Survey, Ministry of Water Resources, Iraq

electrode [10]. Total alkalinity (TA) has been determined by titrating the groundwater samples with sulfuric acid.

2.4 Water Quality Index (WQI)

Water Quality Index (WQI) is one of the most effective methods to investigate water quality. WQI was calculated by using the values of seven parameters, and it was determined based on the WHO [9]. The samples for WQI were collected from deep wells of 36 stations in the Kifri district and each of the seven parameters of these samples was given a special weight (w_i) based on their influence on the water quality, ranging from 1 to 3 as shown in Table 1. A minimum weight which is a value of 1 was given to pH and TA which have less significant roles in human health [11]. However, the maximum weight of 3 was given to the both SO_4^{-2} and TH parameters for their significance in the assessment of the water quality. To find the relative weight, the following equation was utilized [12]:

$$W_i = w_i / \sum_{i=1}^n W_i$$

Where:

W_i represents the relative weight of each parameter and n , is the number of tested or studied parameters. Then, the following equation was used to calculate the quality rating (Q_i):

$$Q_i = \left(\frac{C_i}{S_i} \right) * 100$$

Where:

C_i is each parameter's value

S_i is each parameter's standard value.

Finally, the following equation was used to compute WQI [11]:

$$WQI = \sum_{i=1}^n (W_i * q_i)$$

Where:

WQI is the water quality index, and it is classified into five categories as shown in Table 2; q_i is the rating value of each parameter which is given from

Table 1. Relative and assigned weight value to calculate WQI based on WHO standards

Parameters	WHO standard	Assigned weight	Relative weight
pH	8.5	1	0.0714
EC	1,000	2	0.1429
Ca ²⁺	100	2	0.1429
SO ₄ ⁻²	250	3	0.2143
TDS	500	2	0.1429
TH	500	3	0.2143
TA	250	1	0.0714

Table 2. Classification of WQI categories

Ranges statue	WQI categories
<50	Excellent
50-100	Good
100-200	Poor
200-300	Very poor
>300	Unsuitable

1 to 3 based on the parameter's concentration and importance.

W_i is the relative weight of each parameter i^{th} .

2.5 Nemerow's Pollution Index (NPI)

In order to understand the contamination levels in the water, Nemerow's Pollution Index (NPI) has been utilized. It is represented by the following equation [13]:

$$NPI = \sqrt{[(\max P_i)^2 + (P_i)^2] / 2}$$

Where:

NPI= refers to Nemerow's pollution index

$\max P_i$ is the maximum value of each pollutant or parameter \bar{P}_i , which is the standard value of the specific pollutant.

Therefore, each value of (NPI) with less than one ($PN < 1$) indicates the suitability of water; however, the value of NPI with more than one ($PN > 1$) indicates the unsuitability of water to be used in terms of a specific parameter [14].

3. RESULTS AND DISCUSSION

The obtained results of the studied parameters are illustrated in Table 3 below:

Table 3. Results of the studied physio-chemical parameters in the study area

S. No.	Locations		pH	EC µS/cm	Ca ⁺²	SO ₄ ⁻²	TDS mg/l	TH	TA
	E	N							
1	44.96181	34.68425	7	1,470	211	369	971	718	228
2	44.96854	34.69875	7.1	1,256	200	472	789.1	690	201
3	44.96987	34.68071	7.3	1,000	121	278	601	461	212
4	44.97005	34.69084	6.95	1,950	35	382	799.4	538	261
5	44.96973	34.68842	7.2	1,002	151	340	645	518	198
6	44.96205	34.68703	7.3	1,110	156	313	720.3	528	248
7	44.96326	34.6823	6.99	1,338	167	333	791	617	251
8	44.95958	34.68342	6.75	1,350	178	309	855.8	673	282
9	44.94542	34.69012	6.85	1,121	51	281	718.4	542	253
10	44.95513	34.6883	6.7	1,594	167	432	1,028	818	310
11	44.94377	34.68702	7.2	1,595	198	310	1,016.3	722	319
12	44.96282	34.69113	7	1,455	115	432	925.2	695	257
13	44.96142	34.69272	6.7	359	123	448	198.3	754	296
14	44.95837	34.69439	6.9	1,267	146	309	781.2	598	281
15	44.94942	34.68392	6.88	301	149	369	175.3	618	261
16	44.95173	34.68058	6.9	1,246	110	287	753.5	576	282
17	44.96644	34.6848	8.5	1,003	44	267	651.7	374	303
18	44.96784	34.68211	7.87	1,401	149	317	920	483	173
19	44.95754	34.68019	6.45	304	98	349	195	431	283
20	44.95472	34.69469	6.57	264	129	451	159	592	232
21	44.97005	34.69084	6.6	269	130	338	174	567	271
22	44.96278	34.68988	7.1	1,111	97	362	670.5	428	205
23	44.96205	34.68782	7.18	1,498	200	440	900.6	493	319
24	44.9625	34.69903	7.95	1,012	198	318	640.3	487	245
25	44.95296	34.68775	7.99	1,404	231	301	912.7	691	307
26	44.9575	34.68576	7.95	1,278	193	293	813.8	570	291
27	44.95795	34.68741	8.25	1,167	189	425	729.1	576	301
28	44.96573	34.6889	8.01	1,321	173	298	835.6	429	248
29	44.95124	34.68914	7.95	1,169	152	291	720	625	257
30	44.96658	34.69384	7.98	814	91	300	471	575	303
31	44.96194	34.67824	7.22	1,621	200	348	983	701	298
32	44.95425	34.678	7.31	1,198	121	287	698	489	284
33	44.94679	34.68043	7.21	1,188	145	411	770	517	254
34	44.96641	34.67627	7.05	1,200	157	513	702	654	318
35	44.96002	34.68669	7.96	878	178.5	201	502	502	159
36	44.96239	34.69772	7.71	298	62	119	164	195	171
Min.			6.45	264	35	119	159	195	159
Max.			8.5	1,950	231	513	1,028	818	319
Ave.			7.29	1,105.9	144.88	341.5	677.25	567.9	260
WHO			6.5-8.5	600	150	75	500	500	250

3.1 pH

Generally, the value of pH shows the concentration of hydrogen ions in the solution [15]. It is considered an important parameter of water quality due to its effect on the process of disinfection. According to the obtained data, the pH of the samples was ranging between 6.45 and 8.5 with an average of 7.29. Out of 36 stations, only one location has a pH value equal to the maximum permissible limit for drinking purposes viz. 6.5-8.5 [9]. The water pH has no direct influence on human health; while it has an indirect influence on health as it affects

other parameters. Figure 2 illustrates the pH spatial distribution in the Kifri District.

3.2 Total Dissolved Solids (TDS)

The value of Total Dissolved Solids (TDS) in groundwater is a significant parameter to investigate the suitability of water for different purposes [16]. The concentration of TDS of the groundwater samples in the studied area were ranging between 159 and 1,028 mg/l with a mean of 677.25 mg/l. Approximately 80.55 % of the groundwater samples had TDS values of more than 500 mg/l; while only

7 samples 19.45 % had TDS values of less than the permissible value [17]. Figure 3 illustrates the spatial distribution of TDS in the studied area.

3.3 Electric Conductivity (EC)

Electric Conductivity (EC) is representing the measurement of salinity in water indirectly [18]. The EC values of the Kifri groundwater samples were ranging between 264 to 1,950 $\mu\text{S}/\text{cm}$ with an average of 1,105.9 $\mu\text{S}/\text{cm}$. About 83.33 % of the groundwater samples in the study area had EC values above the critical limit value for drinking. Only 6 samples have values of EC less than 600 $\mu\text{S}/\text{cm}$. Figure 4 below shows the EC spatial distribution in the present area.

3.4 Calcium (Ca^{+2})

The concentrations of calcium in all groundwater samples were ranging between 35 to 231 mg/l with an average of 144.9 mg/l. The standard limit of calcium is 150 mg/l. The obtained results showed that most of the samples had Ca^{+2} concentrations more than the permissible limit. Figure 5 below illustrates the Ca^{+2} spatial distributions within Kifri City.

3.5 Total Alkalinity (TA)

The presence of both carbonate and bicarbonate ions is the main cause of alkalinity levels in water [19]. The results show that the total alkalinity (TA) values ranged between 159 and 319 mg/l, with a mean of 260 mg/l. Therefore, the total alkalinity values in most of the samples were above the desirable limit [9]. While 12 samples (33.34 %) have (TA) values less than the permissible limit. Figure 6 shows the representation of total alkalinity in groundwater samples within the study area.

3.6 Sulfate (SO_4^{-2})

The concentrations of sulfate in the samples were ranging between 119 to 513 mg/l, with a mean value of 341.5 mg/l. Only 2 samples (5.56 %) had values of sulfate less than the permissible limit of 250 mg/l. Figure 7 demonstrates the sulphate spatial distribution within the study area. Recently, health issues that are linked to sulfate in water have increased [20]. Presence of high concentrations of sulfate in water cause an undesirable taste. It contributes to the corrosion of the water distribution pipe system [9].

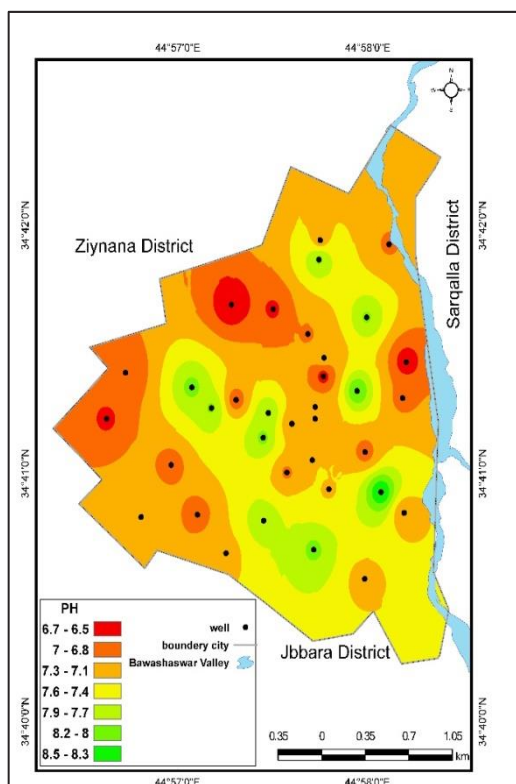


Fig. 2. Distribution of pH values in the study area

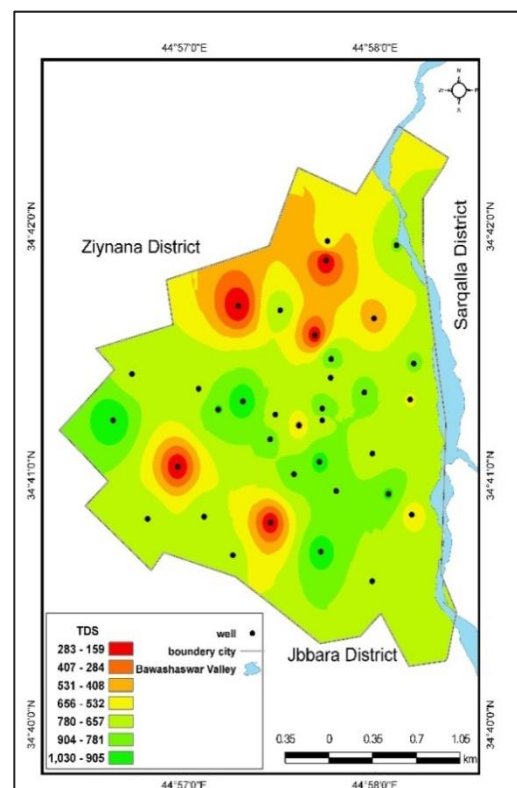


Fig. 3. Distribution of TDS values in the study area

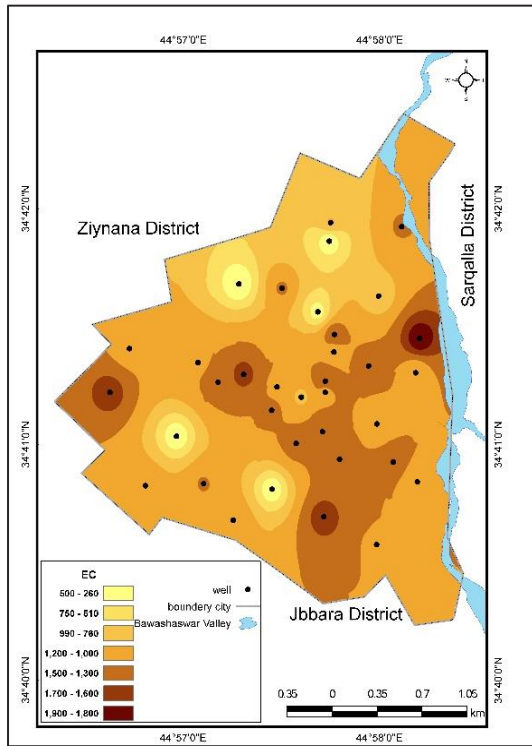


Fig. 4. Distribution of EC values in the study area

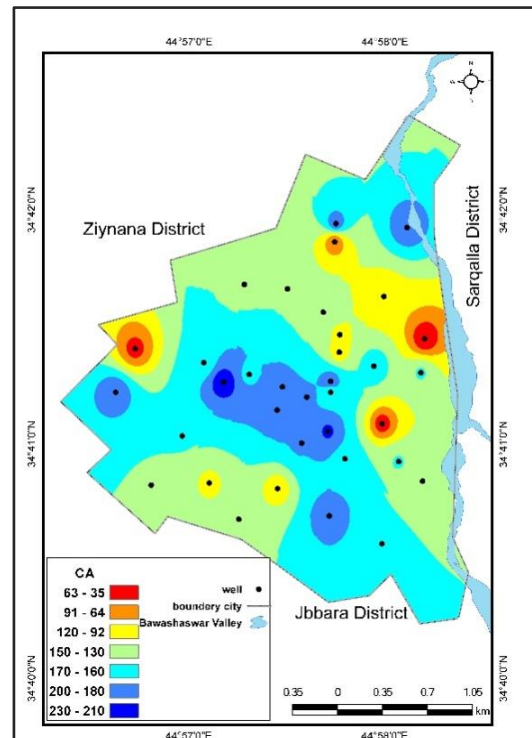


Fig. 5. Distribution of Ca⁺² values in the study area

3.7 Total Hardness (TH)

Water hardness relies on some anions and cations including sulfate, bicarbonate, calcium, chloride and magnesium [21]. High values of total hardness of more than 300 mg/l can cause problems for daily human uses [22]. The concentrations of total hardness of the groundwater samples were ranging

between 195 to 818 mg/l with a mean value of 567.9 mg/l. The permissible value of TH is 500 mg/l according to WHO [9]. In the study area, 36 samples (72.23 %) had TH values greater than 500 mg/l; while only 10 samples (27.78 %) had values less than the permissible value. Generally, water containing CaCO₃ concentration less than 75

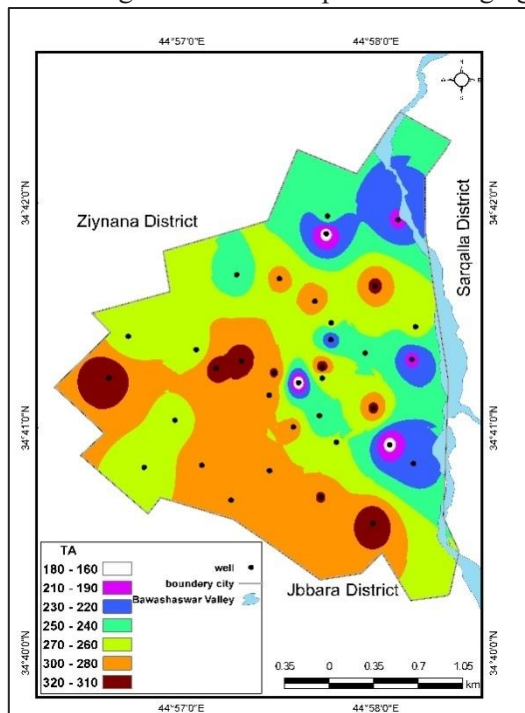


Fig. 6. Distribution of TA values in study area

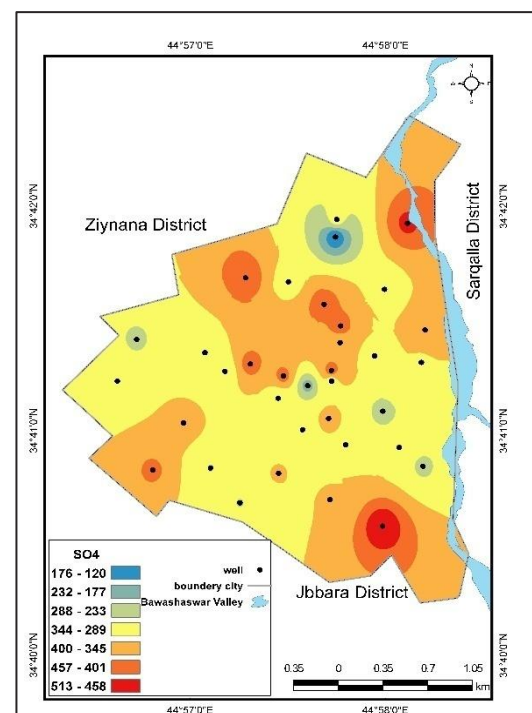


Fig. 7. Distribution of SO₄⁻² values in the study area

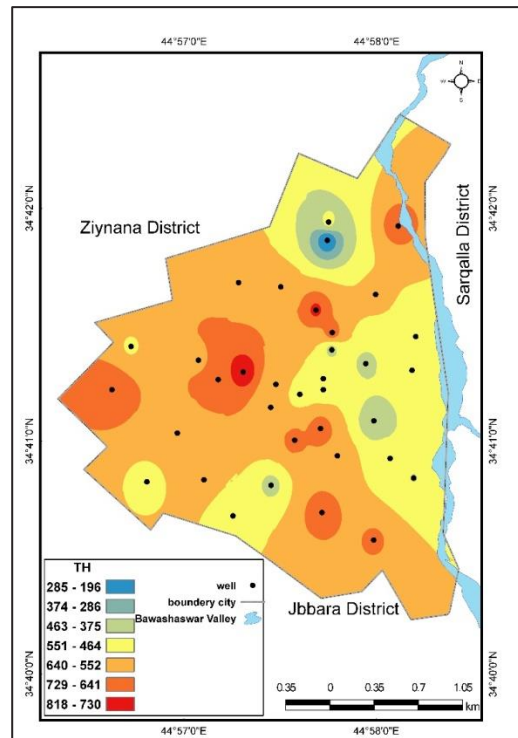


Fig. 8. Distribution of Total Hardness values in the study area

mg/l is soft; 75-150 mg/l of CaCO_3 concentration is moderately hard; while 150-300 mg/l of CaCO_3 concentration is regarded as hard; however, greater than 300 mg/l of CaCO_3 concentration is regarded as very hard [23]. A study conducted in Shorkot City (Jhang) concluded that certain parameters exceeded WHO standards like TDS (62 %), Calcium (62 %), Hardness (44 %) and Chloride (28 %) respectively, whereas Electrical Conductivity exceeded 100 % than the prescribed limit of WHO. These exceeding concentrations of these parameters created various fatal waterborne diseases in the study area i.e. Gastroenteritis, Cholera, Dysentery, Diarrhea, Hepatitis, Kidney stone, Cancer, Asthma and Heart diseases [24].

3.8 Correlation Matrices

The correlation matrices for the parameters including pH, EC, Ca^{+2} , SO_4^{-2} , TDS, TH and TA

has been prepared and explained as shown in Table 4. The results illustrate that EC has a high positive correlation with Ca^{+2} , TDS and TH. In addition, a high positive correlation of Ca^{+2} with each of TDS and TH has been demonstrated. Furthermore, the same is true for SO_4^{-2} with TH and TA.

3.9 Water Quality Index (WQI)

The categories of WQI are included excellent, good, poor, very poor, and unsuitable for drinking [25]. The results of the WQI of the study area showed that 33 stations out of 36 were classified under the 'Poor Quality' category. However, only 3 stations were classified as 'Good Quality' category. Table 5 indicates that the groundwater in Kifri is not suitable for drinking.

A study conducted in Karnataka (India) found that various samples of groundwater samples were

Table 4. Correlation matrix of the studied parameters

Parameters	pH	EC	Ca^{+2}	SO_4^{-2}	TDS	TH	TA
pH	1						
EC	0.152	1					
Ca^{+2}	0.131	0.305	1				
SO_4^{-2}	-0.439	0.143	0.237	1			
TDS	0.192	0.960	0.432	0.128	1		
TH	-0.373	0.341	0.497	0.570	0.378	1	
TA	-0.089	0.219	0.127	0.344	0.218	0.445	1

Table 5. Classification of WQI in the study area

Station	Statue	WQI Type
1	171.85	Poor
2	166.8	Poor
3	115.1	Poor
4	138.95	Poor
5	129	Poor
6	134.7	Poor
7	148.4	Poor
8	152.7	Poor
9	110.75	Poor
10	178.65	Poor
11	172.3	Poor
12	157.1	Poor
13	115.4	Poor
14	139.96	Poor
15	105.55	Poor
16	129	Poor
17	105.6	Poor
18	144.98	Poor
19	85.33	Good
20	104	Poor
21	95.2	Good
22	119.8	Poor
23	168.3	Poor
24	139.8	Poor
25	172.4	Poor
26	152.8	Poor
27	160.3	Poor
28	144.1	Poor
29	140.95	Poor
30	113.85	Poor
31	174.2	Poor
32	126.66	Poor
33	143.55	Poor
34	159.86	Poor
35	117.1	Poor
36	50.4	Good

had 'Very Poor Water Quality', showing that, the area is prevailed by remnants of weathered rock and dissolution of salts from the bedrock into the water resources, creating a serious threat to the natural environment [26].

3.10 Nemerow's Pollution Index (NPI)

The parameters of pollution as NPI at all the stations have been determined and demonstrated in Table 6. The NPI results of pH were in the permissible range for drinking purposes based on WHO standards. Also, the NPI values for EC varied from 0.44 to 3.25 with an average of 1.84 at all monitoring stations. Thus, the NPI values of EC illustrated that 83.34 % of the samples were not fit for drinking purposes based on WHO standards. Roughly the same scenario has been found in terms of TDS values as per WHO standards. Approximately 94.45 % and 80.56 % of the samples in the monitoring stations had NPI values for SO_4^{-2} and Ca^{+2} concentrations respectively, exceeding one, this indicates the high level of pollution for these parameters. It was noticed also that 72.23 % and 66.67 % of groundwater samples had NPI values of more than one in terms of TH and TA concentrations respectively. This indicates that most of the samples in Kifri City were unsuitable for drinking.

4. CONCLUSION

The quality of the groundwater samples that were collected from 36 various stations in the Kifri district were all analyzed and studied to meet the main objectives of the present research. Based on the results, the pH of 97.23 % of the samples was within the permissible limits. However, the EC, TDS, TH, TA, Ca^{+2} and SO_4^{-2} values of most of the samples were above the standard limits set by the WHO. Also, total alkalinity (TA) values for all the samples were higher than the permissible limit. Based on WQI, the results show that 33 stations out of 36 were classified under the 'Poor Quality' category; while only 3 stations were classified as the 'Good Quality' category. Nemerow's pollution index (NPI) method was applied to evaluate the groundwater quality for drinking. In terms of pH, most of the NPI values were acceptable and were within the permissible limits for drinking usage. However, most of the NPI values of EC, TDS, TH, TA, Ca^{+2} and SO_4^{-2} concentration were (>1) and exceeded the WHO standard. Ultimately, those parameters generated many problems for human health. Thus, suitable treatment is required for the consumption of groundwater for drinking. Also, there is a need of finding another source of drinking water in Kifri City for securing the health of the inhabitants from various waterborne diseases.

Table 6. NPI values of studied parameters

Site	pH	EC	Ca ⁺²	SO ₄ ⁻²	TDS	TH	TA
1	0.82	2.45	2.11	1.48	1.94	1.44	0.91
2	0.84	2.09	2.00	1.89	1.58	1.38	0.80
3	0.86	1.67	1.21	1.11	1.20	0.92	0.85
4	0.82	3.25	0.35	1.53	1.60	1.08	1.04
5	0.85	1.67	1.51	1.36	1.29	1.04	0.79
6	0.86	1.85	1.56	1.25	1.44	1.06	0.99
7	0.82	2.23	1.67	1.33	1.58	1.23	1.00
8	0.79	2.25	1.78	1.24	1.71	1.35	1.13
9	0.81	1.87	0.51	1.12	1.44	1.08	1.01
10	0.79	2.66	1.67	1.73	2.06	1.64	1.24
11	0.85	2.66	1.98	1.24	2.03	1.44	1.28
12	0.82	2.43	1.15	1.73	1.85	1.39	1.03
13	0.79	0.60	1.23	1.79	0.40	1.51	1.18
14	0.81	2.11	1.46	1.24	1.56	1.20	1.12
15	0.81	0.50	1.49	1.48	0.35	1.24	1.04
16	0.81	2.08	1.10	1.15	1.51	1.15	1.13
17	1.00	1.67	0.44	1.07	1.30	0.75	1.21
18	0.93	2.34	1.49	1.27	1.84	0.97	0.69
19	0.76	0.51	0.98	1.40	0.39	0.86	1.13
20	0.77	0.44	1.29	1.80	0.32	1.18	0.93
21	0.78	0.45	1.30	1.35	0.35	1.13	1.08
22	0.84	1.85	0.97	1.45	1.34	0.86	0.82
23	0.84	2.50	2.00	1.76	1.80	0.99	1.28
24	0.94	1.69	1.98	1.27	1.28	0.97	0.98
25	0.94	2.34	2.31	1.20	1.83	1.38	1.23
26	0.94	2.13	1.93	1.17	1.63	1.14	1.16
27	0.97	1.95	1.89	1.70	1.46	1.15	1.20
28	0.94	2.20	1.73	1.19	1.67	0.86	0.99
29	0.94	1.95	1.52	1.16	1.44	1.25	1.03
30	0.94	1.36	0.91	1.20	0.94	1.15	1.21
31	0.85	2.70	2.00	1.39	1.97	1.40	1.19
32	0.86	2.00	1.21	1.15	1.40	0.98	1.14
33	0.85	1.98	1.45	1.64	1.54	1.03	1.02
34	0.83	2.00	1.57	2.05	1.40	1.31	1.27
35	0.94	1.46	1.79	0.80	1.00	1.00	0.64
36	0.91	0.50	0.62	0.48	0.33	0.39	0.68
Min.	0.76	0.44	0.35	0.48	0.32	0.39	0.64
Max.	1.00	3.25	2.31	2.05	2.06	1.64	1.28
Ave.	0.86	1.84	1.45	1.37	1.35	1.14	1.04

5. CONFLICT OF INTEREST

The authors declare no conflict of interest.

6. REFERENCES

1. A. Davison, G. Howard, M. Stevens, P. Callan, and L. Fewtrell. Water safety plans: managing drinking-water quality from catchment to consumer (No. WHO/SDE/WSH/05.06). *World Health Organization* (2005).
2. M. Mohsin, S. Safdar, F. Asghar, and F. Jamal. Assessment of Drinking Water Quality and its Impact on Residents Health in Bahawalpur City. *International Journal of Humanities and Social Science* 3(15): 114–128 (2013).
3. A.S. Abbas, A.H. Dawood, and Z.M. Hasan. Evaluation of groundwater quality for drinking purpose in Basrah governorate by using application of water quality index. *Kufa Journal of Engineering* 8(1): 65–78 (2017).
4. M. Redwan, A.A. Abdel Moneim, and M.A. Amra. Effect of water–rock interaction processes on the hydrogeochemistry of groundwater west of Sohag area, Egypt. *Arabian Journal of Geosciences* 9(2): 1–14 (2016).
5. S. Safdar, M. Mohsin, and A.A. Khan. Sustainable Management of Water Supply in Bahawalpur City, Pakistan. *European Academic Research* 1(12): 5824–5850 (2014).
6. M. Mohsin, S. Safdar, M. Nasar-u-Minallah, and A. Rehman. Monitoring of physiochemical quality of drinking water in selected areas of Bahawalpur City, Pakistan. *Journal of Biodiversity and Environmental Sciences* 14(6): 186–196 (2019).
7. N. Aghazadeh, and A.A. Mogadam. Evaluation effect of geological formation on groundwater quality in the Harzandat plain aquifer. *Symposium of Geosciences of Iran* 22: 392–395 (2004).
8. A.R. Sarhat. Assessment of groundwater quality and its suitability for agricultural uses in Kifri. *Journal of Garmian University* 4: 290–300 (2017).
9. WHO. Guidelines for drinking-water quality. *World Health Organization (WHO), WHO chronicle* (2011).
10. APHA and AWWA. Standard methods for the examination of water and wastewater. Standard methods for the examination of water and wastewater. *American Public Health Association and American Water Works Association* 1000–1000 (1995).
11. R.J. Channo. Studying the Probability of Using Groundwater in Baghdad City for Human, Animal, and Irrigation Use. *Al-Khwarizmi Engineering Journal* 8(3): 63–74 (2012).
12. M. Ketata, M. Gueddari, and R. Bouhlila. Use of geographical information system and water quality index to assess groundwater quality in El Khairat deep aquifer (Enfidha, Central East Tunisia). *Arabian Journal of Geosciences* 5(5): 1379–1390 (2012).
13. Q. Yang, J. Zhang, Z. Hou, X. Lei, W. Tai, W. Chen, and T. Chen. Shallow groundwater quality assessment: use of the improved Nemerow pollution index, wavelet transform and neural networks. *Journal of Hydroinformatics* 19(5): 784–794 (2017).
14. Z. Zhaoyong, J. Abuduwaili, and J. Fengqing. Heavy metal contamination, sources, and pollution assessment of surface water in the Tianshan Mountains of China. *Environmental Monitoring and Assessment* 187(2): 1–13 (2015).
15. E.J. Kim, J.E. Herrera, D. Huggins, J. Braam, and S. Koshowski. Effect of pH on the concentrations of lead and trace contaminants in drinking water: a combined batch, pipe loop and sentinel home study. *Water Research* 45(9): 2763–2774 (2011).
16. S.M. Deshpande and K.R. Aher. Evaluation of groundwater quality and its suitability for drinking and agriculture use in parts of Vaijapur, District Aurangabad, MS, India. *Research Journal of Chemical Sciences* 2: 25–31 (2012).
17. WHO. Guidelines for drinking-water quality. *World Health Organization (WHO)* (2004).
18. D. Florescu, R.E. Ionete, C. Sandru, A. Iordache, and M. Culea. The influence of pollution monitoring parameters in characterizing the surface water quality from Romania southern area. *Romanian Journal of Physics* 56(7–8): 1001–1010 (2011).
19. T.B. Singh, I. Bala, and D. Singh. Assessment of groundwater quality of Paonta Sahib (HP). *Pollution Research* 18(1): 111–114 (1999).
20. S. Al-Harashsheh, O. Al-Ayed, M. Amer, and M. Moutq. Analysis of retorted water produced from partial combustion of Sultani oil shale. *Journal of Environmental Protection* 8(9): 1018–1025 (2017).
21. S.B. Applebaum. Demineralization by ion exchange: in water treatment and chemical processing of other liquids. *Elsevier* (2013).
22. M.R. Islam, M.K.I. Sarkar, T. Afrin, S.S. Rahman, R.I. Talukder, B.K. Howlader, and A. Khaleque. A study on total dissolved solids and hardness level of drinking mineral water in Bangladesh. *American Journal of Applied Chemistry* 4(5): 164–169 (2016).
23. A. Nagaraju, A. Thejaswi, and Z. Sharifi. Assessment of groundwater quality and its suitability for agricultural usage in and around Rangampeta area,

- Andhra Pradesh, south India. *Journal of Water Chemistry and Technology* 38(6): 358–365 (2016).
24. M. Azhar, M. Mobeen, M. Mohsin, T. Aziz, A. Rehman, and M. Sajid. Assessment Of Ground Water Quality and its Impact on Human Health (A Case Study of Shorkot City), (Jhang) Punjab, Pakistan. *Pakistan Journal of Science* 73(1): 199–212 (2021).
25. H. Boyacioglu. Utilization of the water quality index method as a classification tool. *Environmental Monitoring and Assessment* 167(1): 115–124 (2010).
26. P. Govindaraju, A.B.S. Manian, D. Nagaraju, and V. Krishnamurthy. Water Quality Index (Wqi) to Evaluate Groundwater Quality in Chickmagaluru District, South Karnataka, India. *Current World Environment* 17(1): 197–212 (2022).

Instructions for Authors

Manuscript Format

The manuscript may contain Abstract, Keywords, INTRODUCTION, MATERIALS AND METHODS, RESULTS, DISCUSSION (or RESULTS AND DISCUSSION), CONCLUSIONS, ACKNOWLEDGEMENTS, CONFLICT OF INTEREST and REFERENCES, and any other information that the author(s) may consider necessary.

Abstract (font size 10; max 250 words): Must be self-explanatory, stating the rationale, objective(s), methodology, main results, and conclusions of the study. Abbreviations, if used, must be defined on the first mention in the Abstract as well as in the main text. Abstract of review articles may have a variable format.

Keywords (font size 10): Three to eight keywords, depicting the article.

INTRODUCTION: Provide a clear and concise statement of the problem, citing relevant recent literature, and objectives of the investigation.

MATERIALS AND METHODS: Provide an adequate account of the procedures or experimental details, including statistical tests (if any), concisely but sufficient enough to replicate the study.

RESULTS: Be clear and concise with the help of appropriate Tables, Figures, and other illustrations. Data should not be repeated in Tables and Figures, but must be supported with statistics.

DISCUSSION: Provide interpretation of the RESULTS in the light of previous relevant studies, citing published references.

ACKNOWLEDGEMENTS: (font size 10): In a brief statement, acknowledge the financial support and other assistance.

CONFLICT OF INTEREST: State if there is any conflict of interest.

REFERENCES (font size 10): Cite references in the text **by number only in square brackets**, e.g. “Brown et al [2] reported ...” or “... as previously described [3, 6–8]”, and list them in the REFERENCES section, in the order of citation in the text, Tables and Figures (not alphabetically). Only published (and accepted for publication) journal articles, books, and book chapters qualify for REFERENCES.

Declaration: Provide a declaration that: (i) the results are original; (ii) the same material is neither published nor under consideration elsewhere; (iii) approval of all authors have been obtained; and (iv) in case the article is accepted for publication, its copyright will be assigned to *Pakistan Academy of Sciences*. Authors must obtain permission to reproduce, where needed, copyrighted material from other sources and ensure that no copyrights are infringed upon.

Manuscript Formatting

Manuscripts must be submitted in Microsoft Word (2007 Version .doc or .docx format); **pdf** files not acceptable. Figures can be submitted in Word format, TIFF, GIF, JPEG, EPS, PPT. Manuscripts, in *Times New Roman*, 1.15spaced (but use single-space for Tables, long headings, and long captions of tables & figures). The text must be typed in a double-column across the paper width. The Manuscript sections must be numbered, i.e., **1. INTRODUCTION, 2. MATERIALS AND METHODS**, and so on... (a) **Title** of the article (Capitalize initial letter of each main word; font-size 16; **bold**), max 160 characters (no abbreviations or acronyms), depicting article’s contents; (b) Author’ first name, middle initial, and last name (font size 12, **bold**), and professional affiliation (i.e., each author’s Department, Institution, Mailing address and Email; but no position titles) (font size 12); (c) Indicate the corresponding author with *; (d) **Short running title**, max 50 characters (font size 10).

Headings and Subheadings (font size 11): All flush left

LEVEL-1: ALL CAPITAL LETTERS; Bold

Level-2: Capitalize Each Main Word (Except prepositions); **Bold**

Level-3: Capitalize each main word (Except prepositions); **Bold, Italic**

Level-4: Run-in head; Italics, in the normal paragraph position. Capitalize the initial word only and end in a colon (i.e., :)

List of REFERENCES must be prepared as under:

a. Journal Articles (*Name of journals must be stated in full*)

1. I. Golding, J. Paulsson, S.M. Zawilski, and E.C. Cox. Real time kinetics of gene activity in individual bacteria. *Cell* 123: 1025–1036 (2005).
2. W. Bialek, and S. Setayeshgar. Cooperative sensitivity and noise in biochemical signaling. *Physical Review Letters* 100: 258–263 (2008).
3. R.K. Robert, and C.R.L.Thompson. Forming patterns in development without morphogen gradients: differentiation and sorting. *Cold Spring Harbor Perspectives in Biology* 1(6) (2009).
4. D. Fravel. Commercialization and implementation of biocontrol. *Annual Reviews of Phytopathology* 43: 337359 (2005).

b. Books

5. W.R. Luellen. Fine-Tuning Your Writing. *Wise Owl Publishing Company, Madison, WI, USA* (2001).
6. U. Alon, and D.N. Wegner (Ed.). An Introduction to Systems Biology: Design Principles of Biological Circuits. *Chapman & Hall/CRC, Boca Raton, FL, USA* (2006).

c. Book Chapters

7. M.S. Sarnthein, and J.D. Stanford. Basal sauropodomorpha: historical and recent phylogenetic developments. In: *The Northern North Atlantic: A Changing Environment*. P.R. Schafer, & W. Schluter (Ed.), *Springer, Berlin, Germany*, pp. 365–410 (2000).
8. J.E. Smolen, and L.A. Boxer. Functions of Europhiles. In: *Hematology*, 4th ed. W.J. Williams., E. Butler and M.A. Litchman (Ed.), *McGraw Hill, New York, USA*, pp. 103–101 (1991).

d. Reports

9. M.D. Sobsey, and F.K. Pfaender. Evaluation of the H2S method for Detection of Fecal Contamination of Drinking Water, Report WHO/SDE/WSH/02.08, *Water Sanitation and Health Programme, WHO, Geneva, Switzerland* (2002).

e. Online references

These should specify the full URL for reference and give the date on which it was consulted. Please check again to confirm that the work you are citing is still accessible:

10. L. Branston. SENSPOL: Sensors for Monitoring Water Pollution from Contaminated Land, Landfills and Sediment (2000). <http://www.cranfield.ac.uk/biotech/senspol/> (accessed 22 July 2005)

Tables and Figures

Insert all tables as editable text, not as images. Number tables consecutively following their appearance in the text, Figures should appear in numerical order, be described in the body of the text, and be positioned close to where they are first cited. Each figure should have a caption that describes the illustration, and that can be understood independently of the main text (Caption Table 1. and Fig 1. font size 10; Bold; Captions should be in sentence case; left-aligned). All Figures should have sufficiently high resolution (minimum 1000 pixels width/height, or a resolution of 300 dpi or higher) to enhance the readability. Figures may be printed in two sizes: column width of 8.0 cm or page width of 16.5 cm; number them as **Fig. 1**, **Fig. 2**, ... in the order of citation in the text. Parts in a figure can be identified by A, B, C, D, ... and cited as Figure 2A, Figure 2B, Figure 2C. Captions to Figures must be concise but self-explanatory. Laser printed line drawings are acceptable. Do not use lettering smaller than 9 points or unnecessarily large. Photographs must be of high quality. A scale bar should be provided on all photomicrographs.

Tables: with concise but self-explanatory headings must be numbered according to the order of citation (like **Table 1.**, **Table 2.**). Do not abbreviate the word "Table" to "Tab.". Round off data to the nearest three significant digits. Provide essential explanatory footnotes, with superscript letters or symbols keyed to the data. Do not use vertical or horizontal lines, except for separating column heads from the data and at end of the Table.

Figures: Figures may be printed in two sizes: column width of 8.0 cm or page width of 16.5 cm; number them as **Fig. 1, Fig. 2, ...** in the order of citation in the text. Captions to Figures must be concise but self-explanatory. Laser printed line drawings are acceptable. Do not use lettering smaller than 9 points or unnecessarily large. Photographs must be of high quality. A scale bar should be provided on all photomicrographs.

Note: The template of the manuscript is available at <http://www.paspk.org/proceedings/>; <http://ppaspk.org/>

Reviewers: Authors may suggest four relevant reviewers, two National and two International (with their **institutional E-mail** addresses).

SUBMISSION CHECKLIST

The following list will be useful during the final checking of an article before sending it to the journal for review.

Ensure that the following items are present:

One author has been designated as the corresponding author with contact details:

- E-mail address (Correct and valid)
- Full address of Institute/organization
- Keywords
- All figure captions
- All tables (including title, description, footnotes)

Further considerations

- Manuscript has been 'spell-checked' and 'grammar checked'
- References are in the correct format for this journal
- All references mentioned in the Reference list are cited in the text, and vice versa
- Permission has been obtained for the use of copyrighted material from other sources (including the Internet)

In case of any difficulty while submitting your manuscript, please get in touch with:

Editor

Pakistan Academy of Sciences
3-Constitution Avenue, Sector G-5/2
Islamabad, Pakistan
Email: editor@paspk.org
Tel: +92-51-920 7140
Websites: <http://www.paspk.org/proceedings/>; <http://ppaspk.org/>



PROCEEDINGS OF THE PAKISTAN ACADEMY OF SCIENCES: PART A Physical and Computational Sciences

CONTENTS

Volume 59, No. 4, December 2022

Page

Research Articles

- Gun Detection in CCTV Images using HAAR-Like Features 1
—*Sami Ur Rahman, Fakhre Alam, and Wajid Ali*
- Design and Implementation of Low-Cost Data Acquisition System for Small and Medium Enterprises (SMEs) of Pakistan 13
—*Muhammad Imran Majid, Ejaz Malik, Tahniyat Aslam, Osama Mahfooz, and Fatima Maqbool*
- Modeling and Intelligent Controller Design for Reactor Regulating System of Advanced CANDU Reactor (ACR-700) in LabVIEW 25
—*Arshad Habib Malik, Feroza Arshad, and Aftab Ahmad Memon*
- Analysis of Stochastic Patterns of Daily Minimum Extreme Temperature of Karachi in Global Climate Change Perspective 37
—*Muhammad Atif Idrees, Syed Ahmed Hassan, and Muhammad Arif Hussain*
- Tidal Range Energy Resource Estimation of Khor Kalamat using Geostatistical Modeling 45
—*Ambreen Insaq, Mirza Salman Baig, Saba Javaid, Umair Abbas, and Zaheer Uddin*
- Evaluation of Air Permeability of Knitted Fabrics at Various Washing Intervals 55
—*Mehreen Ijaz, Namood-e-Sahar, and Zohra Tariq*
- Mathematical Analysis of Conducting and Dielectric Sphere in Fractional Space 61
—*M. Imran Shahzad, M. Akbar, Saeed Ahmed, Sania Shaheen, and M. Ahmad Raza*
- Investigation of Groundwater Quality for Drinking Usage in Kifri District (Iraq) by using NPI and WQI Indices 67
—*Abdulmutalib Raafat Sarhat, Muhammad Mohsin, and Aram Hassan Mohammed*

Instructions for Authors

PAKISTAN ACADEMY OF SCIENCES, ISLAMABAD, PAKISTAN

HEC Recognized, Category Y; Scopus Indexed

Website: <http://www.paspk.org/proceedings/>; <http://ppaspk.org>